Magnetic Resonance Imaging for Percutaneous Interventions

Magnetresonanzbildgebung für perkutane Interventionen

Der Technischen Fakultät der
Friedrich-Alexander-Universität Erlangen–Nürnberg

zur Erlangung des Grades

DOKTOR–INGENIEUR

vorgelegt von

Eva Maria Barbara Rothgang

aus Erlangen

Als Dissertation genehmigt von der
Technischen Fakultät der
Friedrich-Alexander-Universität Erlangen-Nürnberg

Tag der mündlichen Prüfung:	5. Mai 2014
Vorsitzende des Promotionsorgans:	Prof. Dr.-Ing. habil. Marion Merklein
Gutachter:	Prof. Dr.-Ing. Joachim Hornegger
	Prof. Dr.Univ. Gabor Fichtinger

Abstract

The fundamental motivation for all percutaneous interventions is to improve patient care by reducing the invasiveness of the procedure. An increasing number of percutaneous interventions from biopsies, targeted drug delivery to thermal ablations are performed under magnetic resonance (MR) guidance. Its excellent soft-tissue contrast and multiplanar imaging capabilities make MRI an attractive alternative to computed tomography or ultrasound for real-time image-guided needle placement, in particular for targets requiring a highly angulated approach and non-axial scan planes. MRI further provides the unique ability to monitor spatial temperature changes in real-time.

The research efforts of this dissertation were focused on improving and simplifying the workflow of MR-guided percutaneous procedures by introducing novel image-based methods without the need for any additional equipment. For safe and efficient MR-guided percutaneous needle placement, a set of methods was developed that allows the user to: 1) plan an entire procedure, 2) directly apply this plan to skin entry site localization without further imaging, and 3) place a needle under real-time MR guidance with automatic image plane alignment along a planned trajectory with preference to the principal patient axes. Methods for enhanced MR thermometry visualization and treatment monitoring were also developed to support an effective thermal treatment facilitating the ablation of tumor tissue without damaging adjacent healthy structures.

To allow for an extensive *in-vitro* and *in-vivo* validation, the proposed methods for both needle guidance and MR thermometry were implemented in an integrated prototype. The clinical applicability was demonstrated for a wide range of MR-guided percutaneous interventions emphasizing the relevance and impact of the conducted research.

Kurzfassung

Die grundlegende Motivation für alle perkutanen Interventionen ist die Patientenversorgung durch die Verringerung der Invasivität zu verbessern. Eine steigende Anzahl an perkutanen Interventionen, von Biopsien, zielgerichteter Verabreichung von Medikamenten bis hin zu thermalen Ablationen, wird unter Bildgebung mit Magnetresonanz (MR) durchgeführt. Der exzellente Weichteilkontrast und die multiplanaren Bildgebungsmöglichkeiten machen MR zu einer attraktiven Alternative für die bildgesteuerte Nadelplatzierung gegenüber Computertomographie oder Ultraschall. Dies gilt insbesondere für Ziele, die einen stark gewinkelten Ansatz oder nicht axiale Scanschichten benötigen. MR erlaubt zudem, räumliche Temperaturveränderungen in Echtzeit zu überwachen.

Der Forschungsschwerpunkt dieser Dissertation lag auf der Verbesserung und Vereinfachung des Arbeitsablaufes für MR-geführte perkutane Interventionen. Hierzu wurden neuartige, bildbasierte Methoden entwickelt, welche keine zusätzliche Ausrüstung erfordern. Für eine sichere und effiziente MR-geführte Nadelplatzierung wurden eine Reihe von Methoden entwickelt, welche dem Anwender erlauben, 1) die gesamte Prozedur zu planen 2) diesen Plan direkt auf die Lokalisierung der Einstichstelle auf der Haut des Patienten zu übertragen 3) die Nadel unter Echtzeitbildgebung zu platzieren, wobei die Bildgebungsschichten automatisch entlang des geplanten Pfades unter Bevorzugung der Patientenhauptachsen ausgerichtet werden. Zudem wurden Methoden entwickelt, welche die Visualisierung von MR Thermometrie und die Behandlungsüberwachung verbessern. Ziel hierbei war, eine effektive thermale Behandlung zu unterstützen, welche das Tumorgewebe zerstört und gleichzeitig umgebendes gesundes Gewebe erhält.

Um eine umfassende *in-vitro* und *in-vivo* Validierung zu ermöglichen, wurden die entwickelten Methoden sowohl für die Nadelplatzierung als auch für die MR Thermometrie in einem integrierten Prototypen implementiert. Die klinische Anwendbarkeit konnte für eine große Bandbreite von MR-geführten perkutanen Interventionen gezeigt werden. Dies unterstreicht die Relevanz und die Bedeutung der durchgeführten Forschungsarbeit.

Acknowledgment

Magnetic resonance imaging is one of the most exciting fields I could have imagined doing my PhD in and I am very grateful for the chance to have worked with so many outstanding people over the last years.

Christine H. Lorenz played a key role in me becoming so passionate about MRI. I am deeply grateful for her strong support, advice, and help, also in building up a network. Christine continuously gave me the possibility to grow and develop my strengths. I am thankful for her friendship and many stimulating conversations over the last years.

Wesley D. Gilson played a key role in shaping this PhD project. I would like to thank him for his guidance, expertise, motivation, and most importantly his friendship. We spent endless hours together at the MR scanner and he greatly supported me by revising numerous abstracts and papers. My sincere thanks also go to my co-workers at the Center for Applied Medical Imaging in Baltimore. It has been a fabulous team to work in and I greatly appreciate their friendship, humor, and support. I would also like to thank Berthold Kiefer and Jörg Roland for hosting me at the MR onco team and providing their expertise.

Joachim Hornegger set up an amazing and very stimulating lab at the University of Erlangen. I very much appreciate his support, advice, and inspiration over the last years. I am grateful to have had the chance to do my PhD under his supervision in a lab which provides an excellent environment for developing a strong academic record, establishing a network and building many friendships. In particular, I would like to thank Eva Eibenberger who made sure I had a smooth and pleasant start in the lab. I would also like to thank Robert Grimm for his proof-reading and valuable input.

Gabor Fichtinger for being my second adviser and providing a lot of valuable input through his outstanding research in the field of MR-guided interventions. It is a great honor to have him on my thesis committee.

This dissertation would not have been possible without my family. My parents, Barbara and Georg, who have been supporting me unconditionally all my life. I am deeply grateful for their love, support, generosity, encouragement, and faith in me. Susanne who diligently reviewed this thesis. Her input from a different engineering perspective was very valuable and highly appreciated. I am very thankful for her friendship and happy to have such a great little sister. Tobias who has been a perfect anchor, best friend and loving husband. It has been so wonderful discovering the world together, supporting each other, and having so much joy and fun. I very much look forward to the years to come and I deeply thank him for all his love, trust, support, patience, and encouragement.

Eva Rothgang

Contents

Introduction 1

An increasing number of percutaneous interventional procedures are being performed under magnetic resonance (MR) guidance including aspiration, biopsy, sclerotherapy, targeted drug delivery, and thermal ablation. However, over twenty years after the introduction of interventional MRI (iMRI) [Muel 86], these procedures are still performed primarily at academic hospitals. The complexity of the current iMRI workflow is one of the primary barriers to more widespread adoption. The goal of this thesis is to improve the efficacy and efficiency of percutaneous MR-guided interventions by image processing methods without introducing additional hardware. Figure 1.1 illustrates the two main components of this work: real-time needle guidance and online temperature monitoring.

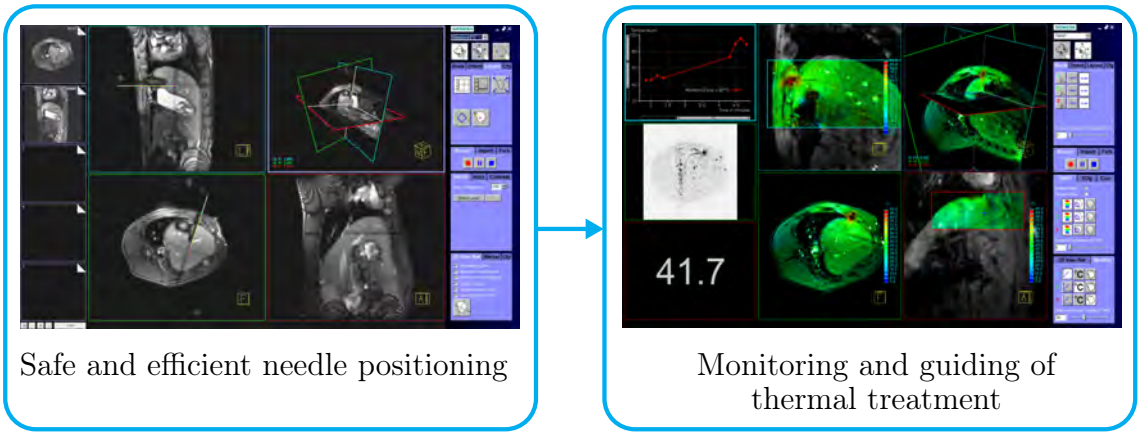

Figure 1.1: *Illustration of thesis goals on the example of a laser ablation procedure performed with the developed clinical prototype.*

1.1 Motivation

The fundamental motivation for all image-guided percutaneous interventions is to improve patient care by reducing the invasiveness of the procedure (Sec. 1.1.1). Most interventions in radiology practice are currently performed under X-ray fluoroscopy, ultrasound (US), and computed tomography (CT) guidance. The potential of MR for guiding percutaneous procedures has been recognized soon after MRI was introduced into diagnostic imaging in the early 1980s [Muel 86, Lufk 88] and has seen growing acceptance over the past decade [Kahn 08]. Research on using MR for guidance of minimally invasive procedures has been driven by several advantages inherent to this

imaging modality (Sec. 1.1.2) but at the same time faces several challenges (Sec. 1.1.3) which need to be considered in algorithm development.

1.1.1 Percutaneous Minimally Invasive Procedures

Percutaneous minimally invasive procedures have in common that a needle is inserted into the target under visual control through a small incision in the skin. They provide alternative treatment strategies to conventional surgical approaches and hold great promise for improved patient care due to lower complication rates, reduced postoperative pain, and shorter hospital stays. In the following paragraphs, a brief introduction into percutaneous minimally invasive procedures performed under MR guidance is given. They all benefit from the methods developed in this work with details given in Chapters 3 and 4. Chapter 5 gives an overview of interventions performed with the developed clinical prototype.

Needle Biopsy

Percutaneous needle biopsy plays a key role in the diagnosis of cancer [Gupt 07] and has virtually replaced excisional biopsy for most lesions throughout the body. Biopsy sampling techniques can be grouped into fine-needle aspiration (FNA) in which a small tissue or fluid sample is aspirated from a lesion using a thin (20 to 25 gauge) needle and core biopsy in which larger (14 to 19 gauge) cutting needles are used. FNA samples are cytologically evaluated, whereas core biopsies allow histologic examination [Bock 91]. MR provides added value when the lesion is not sufficiently visualized using US or CT, or the lesion is located in complex anatomic locations [Schm 99, Weis 08].

Targeted Drug Delivery

The local injection of a therapeutic agent into a target lesion allows for a high therapeutic efficacy with minimal systemic effects [Arep 08]. Spinal infiltration and sclerotherapy are two examples for local administration of a therapeutic agent. In spinal infiltrations, a fluid with anesthetic, anti-inflammatory, or anti-edemic properties is injected directly into the spine [Frit 09, Stre 10]. Percutaneous sclerotherapy is currently the treatment of choice for low-flow vascular malformations. Under image guidance, an irritating solution is injected into abnormally formed or dilated veins. MR plays an important role in the diagnosis of the extent of the venous malformation as areas behind airways or bony structures are invisible to US. Due to the high-soft tissue contrast and multiplanar capabilities of MRI (Sec. 1.1.2), there is also growing interest of using MR for sclerotherapeutic needle guidance in particular for deep seated lesions [Boll 04]. Infiltration and sclerotherapy cases performed with the developed clinical prototype are presented in Section 5.2.3.

Thermal Ablation

Thermal ablations are increasingly used as a regional treatment option to supplement systemic treatment strategies such as chemotherapy [Bela 07]. They provide a minimally invasive alternative to surgery, in particular for patients with comorbidi-

ties or unresectable disease. The goal of all thermal ablation procedures is to cause cell death of diseased tissue while sparing surrounding healthy tissue. Thermal ablations may be performed with a variety of energy sources [Skin 98] including radiofrequency (RF)[Terr 10], high-intensity focused ultrasound (FUS) [Temp 03], microwaves [Kuru 07], laser [Wack 98, Mack 05, Ahra 11], and cryo [Morr 08, Erin 10]. With the exception of FUS, they all require the placement of a thermal applicator into the target structure. MR provides two key advantages over other imaging modalities for guiding thermal ablations. First, its soft tissue contrast and multi-planar imaging capabilities allow to clearly visualize many solid tumors and further support accurate placement of the thermal applicator even into difficult locations. Second, MR can measure in real-time the spatial distribution of temperature changes in tissue. Further information on thermal ablation procedures can be found in Chapter 4.

1.1.2 Rationale for MR Guidance

MR guidance compared to CT or US is more expensive, patient access is more difficult and specially designed devices must be used. However, the advantages of using MR imaging to guide percutaneous interventions are manifold.

Visualization

Lesion visibility with X-ray, CT or US can be limited, in particular for breast, liver, prostate, and musculoskeletal tumors [Tatl 07, Lewi 00]. In contrast, MRI not only allows for unparalleled visualization of target lesion but also of surrounding structures due to its excellent soft-tissue contrast and high vascular conspicuity. MRI further has the unique ability to accentuate different tissue characteristics by providing multiple contrast mechanisms like T1, T2, or proton-density weighting (Sec. 2.1.2). This all aids in accurate needle positioning and in preventing damage to adjacent structures which would not be seen under other imaging modalities. The ability of MR to provide functional information such as flow, perfusion, and diffusion, is further beneficial for accurate identification of target location and determination of intervention endpoint [Weis 08].

Multiplanar Imaging Capabilities

The multiplanar capabilities of MRI, i.e. the ability to image in three dimensions and in any orientation, allows for visualization of the target lesion and for tracking of the needle or thermal applicator in any plane. In contrast to CT [Silv 99, Keat 01, Gupt 07], one can directly image along the axis of the device even if the lesion is targeted along a double oblique trajectory like in subcostal liver biopsies [Schm 99]. US provides multiplanar imaging, however device guidance can be problematic if either bony structures or air space lies between puncture point and tumor [Tatl 07]. The multiplanar imaging capabilities of MRI play a fundamental role in the algorithm design for real-time needle guidance in this work.

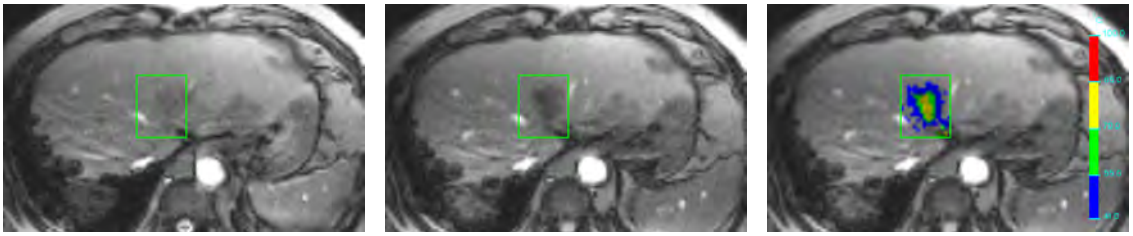

(a) Before ablation (b) Tissue change (c) Fused temperature information

Figure 1.2*: Laser-induced thermal ablation in liver under real-time MRI. The ablation zone can be detected as a signal drop in the magnitude image (a) and relative temperature changes can be calculated from phase images (b). The green box marks the area of the lesion.*

Intra-procedural Monitoring

For an effective and safe treatment, intra-procedural monitoring is essential [Solo 10]. Of particular importance for this work is the capability of MRI to provide immediate assessment of the extent of thermally-induced tissue alterations (Fig. 1.2). With MR thermometry, spatial temperature changes can be monitored in real-time (Chap. 4). This is enhanced by the fact that the MR signal changes in coagulated tissue due to ^1H loss. On the contrary, ablated tissue can be only visualized with CT after thermal treatment by contrast enhancement [Teic 06]. MRI further provides abilities to detect intra-procedural hemorrhage during a biopsy or to monitor targeted drug delivery, e.g. in sclerotherapy [Weis 08].

No Ionizing Radiation

Unlike X-ray and CT, MR does not expose the patient and physician to any ionizing radiation. This is of particular importance to younger patients, women of childbearing age and interventional staff who perform these interventions on a daily basis [Mill 03b, Mill 03a]. X-ray or CT fluoroscopy are particularly prone to yielding high radiation dose for both patient and personnel [Nawf 00].

1.1.3 Challenges in Interventional MRI

Current MR systems are designed primarily for diagnostic imaging. Large parts of the workflow need to be customized in order to make intra-procedural guidance and monitoring of thermal therapies feasible in a clinical setting. The following paragraphs give an overview of the challenges in interventional MRI and introduce recent technological advances.

For diagnostic imaging, image acquisition can take several minutes depending on the scanner hardware, imaging sequence and spatial resolution. In contrast, for guiding percutaneous interventions, image feedback in near real-time is needed with sufficient image quality to visualize the needle, targeted lesion and surrounding structures. Section 2.3 gives an overview of image acquisition strategies used in this work. Achieving high-temporal resolution with continuous visualization of tumor and cri-

tical structures also plays an important role in the algorithm design for real-time needle guidance (Chap. 3).

Patient accessibility is as important as real-time image feedback. Conventional high-field ($\geq$ 1 T) MR scanners have a narrow ($\leq$ 60 cm) and long ($\geq$ 150 cm) bore to achieve a homogeneous main magnetic field crucial for image quality (Sec. 2.4.2). Recent development of wide-bore (70 cm) scanners has greatly improved patient access [Solo 10], however there is still not much room for additional equipment, in particular, when working in a sterile field (Fig. 1.3a). The accessibility to the patient for positioning instruments is further limited by the fact that MR imaging requires coils to be placed as closely as possible to the region to be imaged. The geometries of currently available coils are not designed for interventional procedures but focus on optimizing signal-to-noise ratio (SNR) for diagnostic MRI. One issue, for example, are the small coil openings (Fig. 1.3b) which limit the field for device placement and complicate sterile draping.

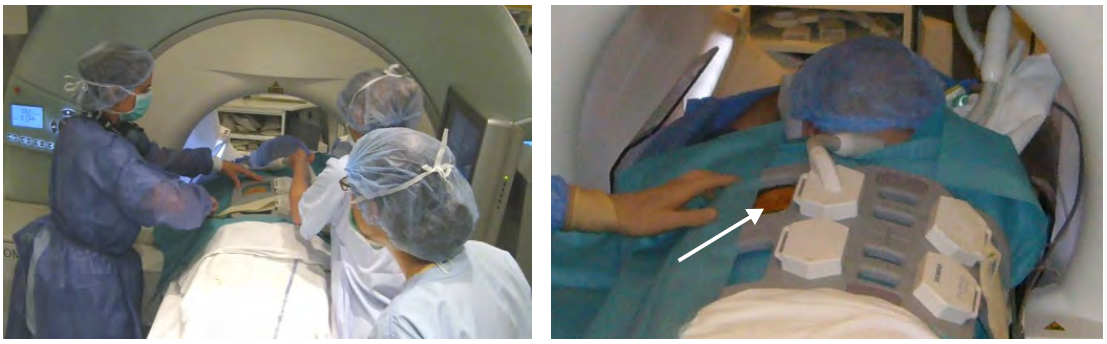

(a) Patient preparation (b) Coil placement

Figure 1.3*: Patient and equipment preparation for a laser ablation of a tumor located in the spine/rib junction. The trocar for laser fiber positioning is placed through the coil opening (see arrow). Before needle placement the coil is covered by sterile pads.*

Another hurdle to MR-guided interventions is the noise generated during scanning [Moel 02] which makes communication between medical personnel difficult. Expensive optical headphones with adaptive noise reduction exist, however most sites rely on hand signals (Fig. 1.4). Thus, methods requiring less communication would be beneficial.

All devices used in an iMRI suite must also be MR-compatible, most of the equipment from CT- or US-guided procedures cannot be used (Fig. 1.5a). Needles should be made of material with similar magnetic susceptibility to water [Koli 04] and imaging parameters should be carefully chosen to minimize magnetic susceptibility-induced needle artifacts (Sec. 2.4.2). The strong magnetic field can attract a ferromagnetic object, pulling it rapidly into the center of the bore by considerable force (Fig. 1.5b). This missile effect will not only damage equipment but can also lead to fatal injuries [Chal 01].

(a) Move slice towards head (b) Move slice towards feet

Figure 1.4: *Communication during a spinal infiltration between physician and technician running the scanner from the control room. Hand signals indicate in which direction to move the real-time scan planes. The noise of the MR scanner does not allow use of the patient communication system during real-time scanning.*

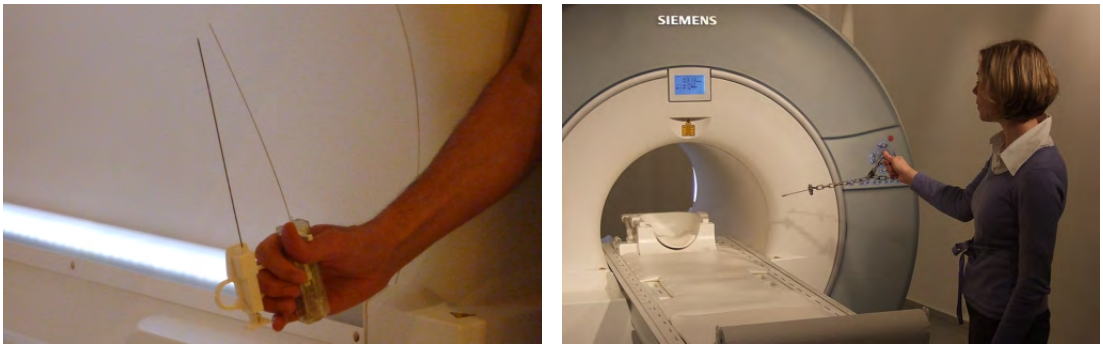

(a) MR-compatible and non MR-compatible needle, courtesy of Prof. Afshin Gangi (b) Demonstration of the 'missile effect'

Figure 1.5: *Objects containing ferromagnetic material are strongly attracted by the magnetic field when brought into the proximity of an MR scanner. The more mass an object has, the stronger the active force becomes. Objects such as wheelchairs or oxygen tanks can be drawn in as quickly as small objects like the screw driver in (b).*

1.2 Contributions to the State of the Art

This dissertation investigates methods for the improvement of MR-guided percutaneous interventions and their evaluation in a clinical setting. Focus was put on developing methods which simplify the workflow of such procedures without introducing any additional equipment. In the following paragraphs, an overview of the major contributions of this dissertation is presented along with corresponding scientific publications. The full list of publications can be found at the end of this work.

Needle Guidance

The goal was to develop methods to improve and streamline the workflow of MR-guided percutaneous procedures with a focus on target locations that cannot be easily

reached using CT or US guidance. The major contributions of this dissertation for freehand MR-guided percutaneous needle placement are as follows.

- Algorithm for precise and reproducible entry point localization on the patient's skin using only the MR landmark laser and a planning dataset [Roth 12b]. The algorithm is based on a two-step approach, divided into superior-inferior and lateral localization. The latter is based on calculating the offset along the patient's body contour derived from planning image segmentation. The proposed approach removes several time-consuming steps associated with state-of-the art entry point localization and allows for localization of all entry sites in one shot.

- Algorithm for automatic slice alignment along a planned trajectory with preference to the principal patient axes [Roth 13]. Two MR slices are aligned along the trajectory and one orthogonal to them at the target location. The resulting saturation bands correspond to the planned path. Thus, the user can simply follow them during needle advancement, knowing that the target is reached once a cross-sectional needle artifact appears in the orthogonal target slice.

  (Slice alignment is considered one of the major challenges of freehand MR-guided needle placement, in particular for complex trajectories.)

- Algorithms to further enhance automatic slice alignment by updating the planned trajectory to the actual device entry point and providing feedback to the user about the current needle position. The planned trajectory is updated based on detecting the device entry point while it is inserted into the subcutaneous tissue under continuous imaging [Roth 11a, Stre 09]. The algorithm for online needle detection is based on a passive approach, i.e. it exploits signal voids induced in the MR image by the needle.

Integrated Workflow for Thermal Ablations

To make full use of the advantages of MRI for guiding thermal ablations (Sec. 1.1.2), an integrated solution for a thermal therapy workflow with enhanced thermal mapping capabilities was developed. The major scientific contributions are summarized below.

- Algorithm for global correction of $\boldsymbol{B_0}$ drift during online MR thermometry with no need for user interaction [Roth 11c]. The proposed algorithm works by automatically determining the mean phase drift from all voxels which show a standard deviation in the phase below a certain threshold.

- Algorithms for enhanced MR thermometry visualization and treatment monitoring during thermal treatment [Roth 10a]. (Reading MR thermometry images can be challenging due to the sensitivity of MR thermometry to various artifacts.)

- Development of an integrated system that supports the entire MR-guided thermal ablation workflow from planning to applicator placement to real-time monitoring independent of the heating source and makes use of the methods developed within this thesis [Roth 12c].

Clinical Validation and Applications

The broad use of the developed prototype for clinical studies emphasizes the relevance and potential impact of the conducted research.

- The proposed image-based workflow improvements have been validated in patient studies for a wide range of MR-guided percutaneous interventions [Bret 12, Roth 12a].
- The developed platform serves as a tool for researcher to explore the use of MR thermometry in new clinical applications [Roth 11b, Kobu 12, Bome].

A complete list of publications can be found in the attached vita.

1.3 Outline

This dissertation focuses on improving methods for performing MR-guided minimally invasive percutaneous procedures. It is composed of two main parts, real-time MR-guided needle placement and MR thermometry (Fig. 1.6). As these two are highly interconnected, the evaluation of the developed methods is presented in one joint chapter. A brief background in interventional MRI is given in Chapter 2. The following overview summarizes the key topics of each chapter.

Chapter 2 - Basics of Magnetic Resonance Imaging

A brief introduction to basic principles of magnetic resonance imaging is presented with a focus on interventional imaging. MR signal generation and image reconstruction are discussed, and key imaging parameters are introduced. The second part of the chapter focuses on interventional MRI. Pulse sequences used frequently during iMRI studies are described and common artifacts are reviewed with an emphasis on those that most impact needle guidance and MR thermometry.

Chapter 3 - Real-time MR-guided Needle Placement

A brief overview of current guidance concepts in the area of MR-guided percutaneous interventions is presented with an in-depth examination of the freehand method. Image-based methods to improve and streamline the freehand workflow are presented including a novel method for localizing the entry point on the patient's skin and an algorithm for automatic real-time slice alignment along the planned trajectory. The chapter closes by discussing further ideas for automatic entry point adaptation and real-time needle artifact segmentation.

Chapter 4 - MR Thermometry

The proton resonance frequency (PRF) shift method is described and established as the accepted technique for performing MR thermometry. Methods for enhanced thermometry visualization and automatic $\boldsymbol{B_0}$ drift correction are introduced. As one aim of the thesis was to validate the proposed methods *in-vivo* in a clinical setting, a prototype which integrates needle guidance and MR thermometry was developed.

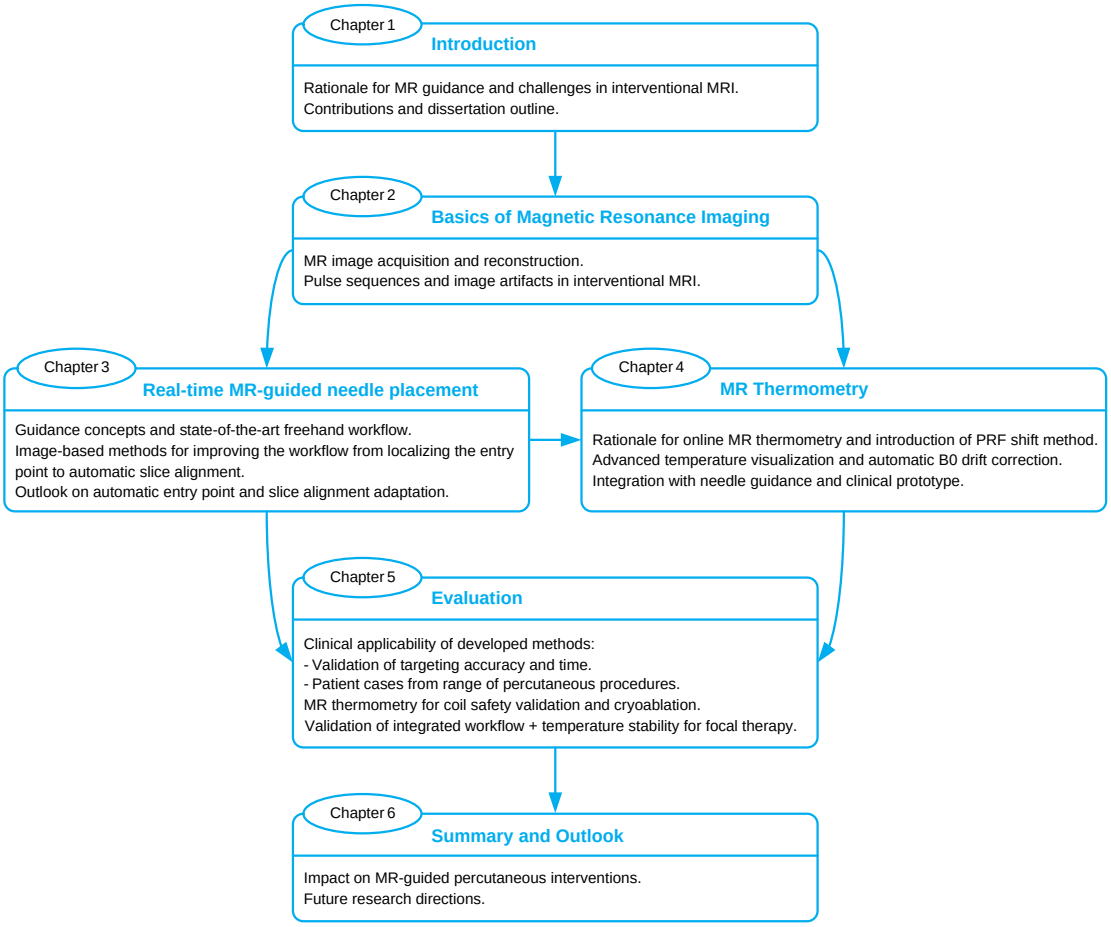

Figure 1.6*: Dissertation outline*

The chapter presents this prototype and shows how it was integrated into the MR scanner setup which is usually focused on diagnostic and not interventional imaging.

Chapter 5 - Evaluation

The methods presented in Chapter 3 and 4 were implemented in a clinical prototype which was evaluated both *in-vitro* and *in-vivo*. The chapter starts by presenting a study validating both targeting accuracy and time for the proposed needle guidance approach. To prove the clinical feasibility of those methods, patient cases from a wide range of percutaneous interventions are presented. The third section of the chapter summarizes studies for which the developed MR thermometry methods have been used ranging from an *in-vivo* cryoablation study, verification of safety validations for a new endorectal coil at 7 T to temperature stability evaluation in prostate cancer patients with focus also on the clinical feasibility of the proposed integrated workflow.

Chapter 6 - Summary and Conclusions

A summary of the innovative techniques presented in this dissertation and their impact on MR-guided percutaneous interventions is discussed.

Basics of Magnetic Resonance Imaging

2

Magnetic resonance imaging is based on the interaction of a nucleus possessing a spin and an applied magnetic field. The goal of this chapter is to give a brief introduction into magnetic resonance imaging with focus on interventional imaging. All image examples presented have been acquired during this project. The first part of the chapter gives an introduction into MR signal generation, spatial encoding, and image reconstruction (Sec. 2.1 and 2.2). The next part focuses on gradient echo pulse sequences and techniques to increase temporal resolution, the key for real-time guidance (Sec. 2.3). The chapter closes by an overview of common artifacts in interventional MRI which play an important role in this work (Sec. 2.4). For further information, the interested reader is referred to "Handbook of MRI Pulse Sequences" by Bernstein et al. [Bern 04] and "Magnetic Resonance Imaging: Physical Principles and Sequence Design" by Haacke et al. [Haac 99]. In addition, fundamental journal articles are referenced throughout this chapter which is partly based on [Roth 08].

2.1 Acquisition

For in vivo imaging, usually the ^1H nucleus is used as it is the most common isotope of hydrogen and the human body mainly consists of water and fat of which ^1H is an elementary part.

2.1.1 Spin and Magnetization

Nuclear spin is an intrinsic property of an atom with an odd atomic number and/or an odd atomic weight. As a circulating charge generates a magnetic moment, nuclei with a spin can be viewed as small rotating magnets, represented by vectors (Fig. 2.1). The MR signal results from a collection of spins in a voxel rather than an individual spin. The vector sum of the magnetization vectors from all of these spins is called net magnetization $\boldsymbol{M}$. In the absence of an external magnetic field, the spins are randomly orientated, the vectors cancel each other out, and consequently no net magnetization is observed in the tissue. If an external homogeneous magnetic field $\boldsymbol{B_0}$ is applied, the proton spins will either align parallel (spin-up) or anti-parallel (spin-down) to the magnetic field and precess about its axis (Fig. 2.1). The precession frequency is proportional to the strength of the magnetic field. This relationship is the underpinning principle behind MRI and is known as Larmor's precession

$$\omega_0 = \gamma \cdot \|\boldsymbol{B_0}\|_2 \,, \tag{2.1}$$

where ω_0 is the resonance frequency, the so-called Larmor frequency, $\|\boldsymbol{B_0}\|_2$ the static magnetic field in Tesla (T), and γ the gyromagnetic ratio of the observed nucleus (2.675×10^8 rad/(s · T) for ^1H).

The two different spin orientations correspond to two different energy levels. The energy difference ΔE is proportional to the Larmor frequency, that is

$$\Delta E = \hbar \cdot \omega_0 = \hbar \cdot \gamma \cdot \|\boldsymbol{B_0}\|_2 \,, \tag{2.2}$$

where $\hbar$ is the Planck's constant ($1.055 \times 10^{-34} J \cdot s$). The spin-up orientation is of lower energy, and its configuration contains more protons than the higher energy, spin-down configuration. In thermal equilibrium the number of protons in each energy level is constant and can be described by the Boltzmann distribution

$$\frac{n\uparrow}{n\downarrow} = \mathrm{e}^{-\frac{\Delta E}{kT}} \,, \tag{2.3}$$

where $n\uparrow$ is the number of protons in the upper energy level, $n\downarrow$ the number of protons in the lower energy level, ΔE the energy difference between the two spin states, k the Boltzmann's constant (1.381×10^{-23}J/K), and T the absolute temperature in Kelvin (K). The excess of up spins described by Boltzmann's distribution causes a constant magnetization in the body with a value $\|\boldsymbol{M_0}\|_2$, known as net bulk magnetization.

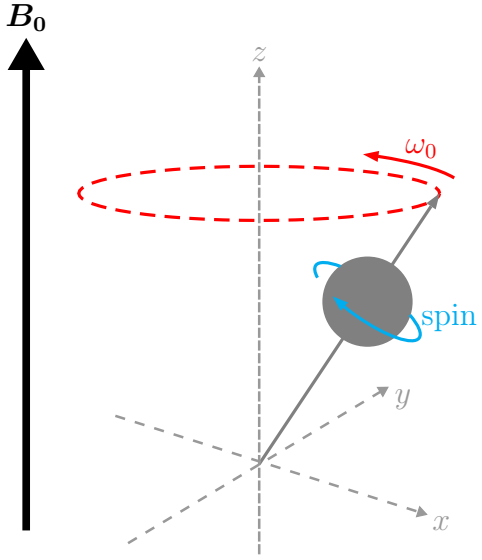

Figure 2.1: *^1H possesses the quantum property of spin resulting in a small magnetic moment. When placed in an external magnetic field $\boldsymbol{B_0}$, the proton precesses about $\boldsymbol{B_0}$ with the resonance frequency ω_0. By convention, $\boldsymbol{B_0}$ is defined to be oriented in the z-direction of a Cartesian coordinate system.*

This arrangement with $\boldsymbol{M_0}$ oriented parallel to the magnetic field with no transverse component is the equilibrium configuration. $\boldsymbol{M_0}$ can be imagined as a macroscopic magnetization vector in z-direction (Fig. 2.2). The magnitude of $\boldsymbol{M_0}$ is proportional to the applied external field strength

$$\|\boldsymbol{M_0}\|_2 = \chi \, \|\boldsymbol{B_0}\|_2 \,, \tag{2.4}$$

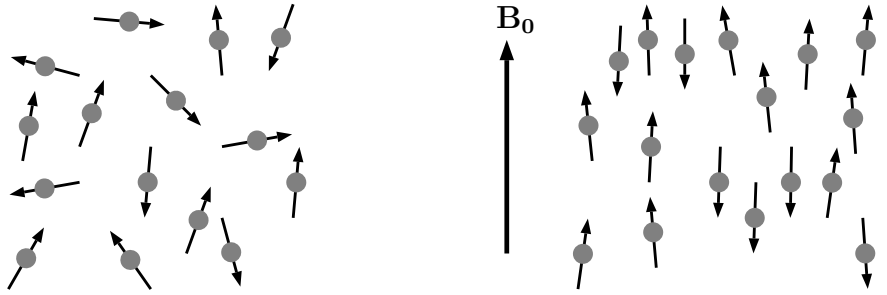

a) No Applied Magnetic Field b) Applied Magnetic Field

Figure 2.2: *Microscopic picture of a collection of protons. a) In the absence of an external magnetic field, the spins are randomly orientated. b) If an external magnetic field* $\boldsymbol{B_0}$ *is applied, the spins either align with the magnetic field or against it resulting in a constant longitudinal magnetization with a value* $\|\boldsymbol{M_0}\|_2$.

where χ is the magnetic susceptibility which defines the extent to which material placed in an external magnetic field becomes magnetized itself. Depending on χ, materials can be classified as diamagnetic ($\chi < 0$), paramagnetic ($\chi > 0$, maximum field increase of 1%) and ferromagnetic ($\chi \gg 0$, field increase > 1%). Variations in magnetic susceptibility can result in artifacts (Sec. 2.4) as the additional magnetic fields of the materials inside the magnet are superimposed on $\boldsymbol{B_0}$ leading to local magnetic field variations and thus a locally changing resonance frequency (Eq. (2.1)).

2.1.2 Spin Excitation and Relaxation

Spins are excited by playing a short pulse of RF energy at resonance frequency ω_0. The RF pulse stimulates transitions between the spin-up and spin-down energy levels and perturbs the net bulk magnetization vector $\boldsymbol{M_0}$ away from the equilibrium orientation. As a result, $\boldsymbol{M_0}$ is flipped towards the xy-plane by a flip angle dependent on the length and amplitude of the RF pulse. Hence, the longitudinal magnetization $\boldsymbol{M_z}$, i.e. the component of $\boldsymbol{M_0}$ in the direction of $\boldsymbol{B_0}$, decreases and the transverse magnetization $\boldsymbol{M_{xy}}$, i.e. the xy-component of $\boldsymbol{M_0}$ perpendicular to $\boldsymbol{B_0}$, rises. The transverse magnetization induces a signal in a receiver coil placed perpendicular to the transverse plane. This signal is called free induction decay (FID) because transverse magnetization precesses freely, induces a signal, and decays immediately after the end of the RF pulse.

After the RF pulse, the spins immediately begin to dissipate the added energy and begin to return to their equilibrium state. This process is known as relaxation and can be described by viewing longitudinal and transverse magnetization as separate entities. The longitudinal magnetization $\boldsymbol{M_z}$ recovers fully due to spin-lattice interactions, an exponential process characterized by the time constant T_1, the time required for the longitudinal magnetization to recover to approximately 63% of its final value. The transverse magnetization $\boldsymbol{M_{xy}}$ decays because the spins lose their phase coherence due to unavoidable spin-spin interactions. The rate of decay follows an exponential curve characterized by the time constant T_2, the time required for the transverse magnetization to decline to 37% of its initial value. Another cause for the

loss of transverse magnetization arises from the fact that B_0 is never 100% uniform. As a consequence, the FID decays faster than T_2, namely at T_{2^*} which is a combination of T_2 and the effects of inhomogeneities (Fig. 2.3). The time constants T_1, T_2 and T_{2^*} are tissue dependent and the reason for the excellent soft-tissue contrast of magnetic resonance imaging. Further information on contrast mechanisms in MR imaging can be found in [Nitz 99, Baze 04].

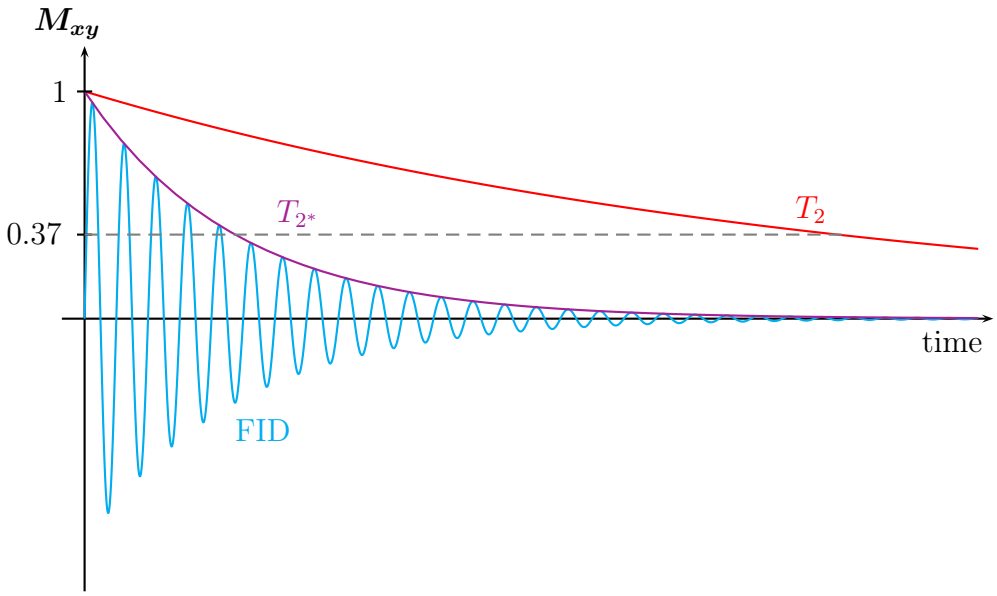

Figure 2.3: *Free induction decay (FID) characterized by T_{2^*}. The contribution of spin-spin relaxation to the decay of the transverse magnetization $\boldsymbol{M_{xy}}$ is given by T_2.*

2.1.3 Spatial Encoding

The preceding section described how an MR signal is generated. For imaging purposes, this signal needs to be spatially encoded [Laut 73]. The underlying principal for spatial encoding in MRI is the relationship between the frequency a proton resonates at and the magnetic field strength it experiences as described by the Larmor Equation (2.1). The local magnetic field is spatially varied by application of magnetic field gradients. A gradient causes a linear variation in the magnetic field, and thus in the Larmor frequency, in a specific direction. Consequently, the local magnetic field is specified by

$$\boldsymbol{B_l} = \boldsymbol{B_0} + \Big(\boldsymbol{G} \cdot \boldsymbol{r}\Big) \cdot \boldsymbol{e_r}, \tag{2.5}$$

where $\boldsymbol{B_l}$ is the local magnetic field at position $\boldsymbol{r}$, $\boldsymbol{G}$ is a vector representing the total gradient amplitude and direction and $\boldsymbol{e_r}$ is the unit vector in r-direction. Since the field strength spatially varies, the spins no longer precess with the same frequency ω_0 everywhere as expressed by an expanded version of the Larmor equation

$$\omega(\boldsymbol{r}) = \gamma \cdot \|\boldsymbol{B_l}\|_2 = \gamma \cdot \Big(\|\boldsymbol{B_0}\|_2 + \boldsymbol{G} \cdot \boldsymbol{r}\Big), \tag{2.6}$$

where $\omega(\boldsymbol{r})$ is the local Larmor frequency at position $\boldsymbol{r}$. In the following sections, the details of spatial encoding are described for an axial slice. However, MRI allows to

acquire an image in any orientation. The interested reader is referred to Haacke et al. Chapters 9 and 10 [Haac 99].

Slice Selection

The first step of spatial encoding is to switch on a slice-selection gradient G_{ss} simultaneously with an RF pulse with a center frequency ω_{RF} and a bandwidth $\Delta\omega_{RF}$. Following, only the spins in a slice of thickness Δz precess with the Larmor frequency in the range $\omega_{RF} \pm \Delta\omega_{RF}/2$ and thus are excited. The slice thickness Δz is determined by the amplitude of G_{ss} and the bandwidth $\Delta\omega_{RF}$ of the RF pulse as depicted in Figure 2.4.

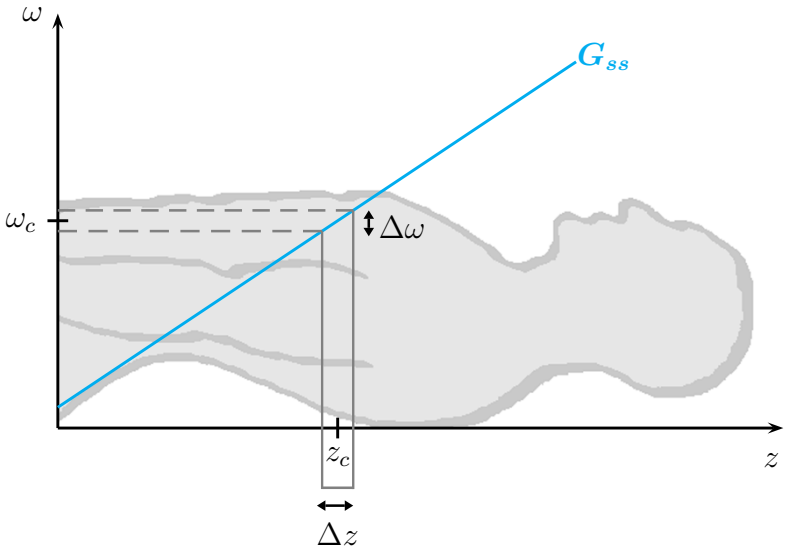

Figure 2.4: *Slice selection by switching on a slice selection gradient G_{ss}. Only protons within the slice Δz are excited by a stimulating RF pulse with a bandwidth $\Delta\omega_{RF}$. A stronger gradient G_{ss} produces a thinner slice for a given $\Delta\omega_{RF}$.*

Frequency Encoding

After slice selection and excitation, there is still no information about the origin of the MR signal within the xy-plane as all protons within the slice precess with the same frequency ω^*. In order to slightly adjust the frequency at which the protons are spinning, an additional gradient G_{re} along the x-axis, generally denoted as the readout or frequency encoding direction, is turned on during acquisition (readout) of the MR signal (Fig. 2.5). This change in Larmor frequency along the readout direction can be described by

$$\omega(x, t_{acq}) = \omega_0 + \Phi_{re}(x, t_{acq}), \tag{2.7}$$

where $\omega(x, t_{acq})$ is the local Larmor frequency and

$$\Phi_{re}(x, t_{acq}) = x\,\gamma \int_0^{t_{acq}} G_{re}(\tau)\mathrm{d}\tau \tag{2.8}$$

the spatially dependent phase along the readout direction x at acquisition time t_{acq}.

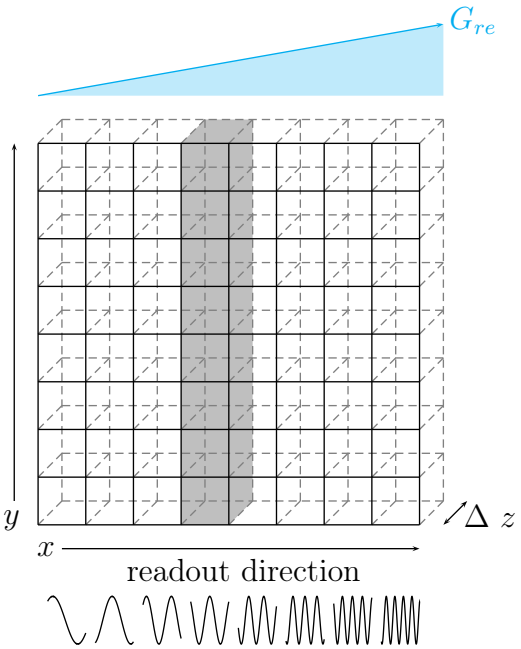

Figure 2.5: *For frequency encoding an additional magnetic gradient G_{re} is applied along the x-axis during detection of the echo. This changes the Larmor frequency of the spins dependent upon their position along the readout direction.*

Phase Encoding

The third localization dimension is provided by the application of a phase encoding gradient G_{ph} orthogonally to the other two gradients. G_{ph} is briefly switched on and off after slice selection and excitation, but before frequency encoding. Once G_{ph} is turned off, the proton precession returns to its original frequency, but the phase of the spins at the one end of G_{ph} leads those at the other end. During readout of the signal, the phase of proton spins in different lines will thus systematically differ. The amount of induced phase shift depends on the duration T_{ph} and magnitude of G_{ph}

$$\Phi_{ph}(y) = y\,\gamma \int_0^{T_{ph}} G_{ph}(\tau)\mathrm{d}\tau, \tag{2.9}$$

where $\Phi_{ph}(y)$ is the spatially dependent phase along the phase encoding direction at the end of G_{ph}.

2.2 Reconstruction

The acquired analog signal received by the RF receive coil is digitized and stored in a raw data matrix, called k-space. The k-space is then Fourier-transformed into image space. Figure 2.6 shows this correspondence. The k-space formalism has first been described by Ljunggren [Ljun 83] and Twieg [Twie 83].

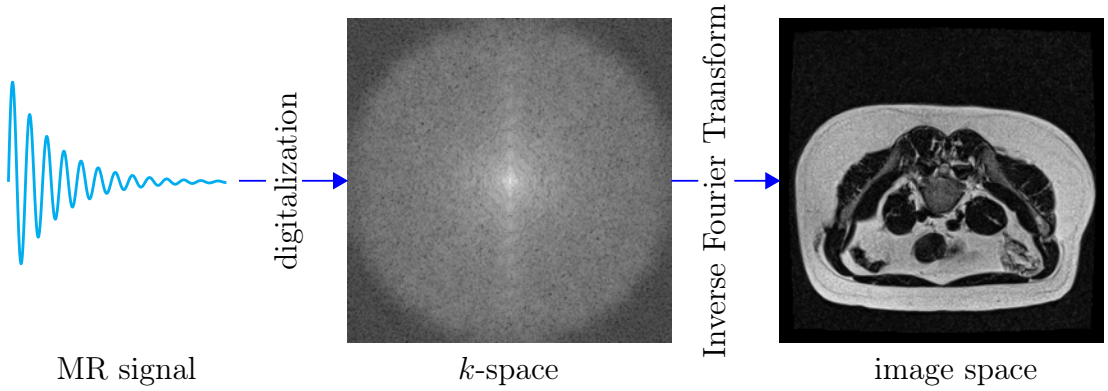

Figure 2.6: *Correspondence between acquired analog MR signal, k-space, and image space, shown on the example of an axial slice acquired for planning a spinal infiltration. For the k-space image the logarithmical absolute values are shown.*

2.2.1 k-Space

For two-dimensional (2-D) acquisition strategies the k-space is a 2-D data matrix. In which order the k-space is filled is defined by the k-space trajectory. The most popular trajectory is the Cartesian raster in which each line corresponds to N_{re} readout (data acquisition) time points during one phase encoding step (Fig. 2.7). Thus, to construct an e.g. 256×256 image, the slice excitation and signal detection is repeated 256 times, with only the amplitude of G_{ph} changing each time. Usually, G_{ph} is varied in a stepwise fashion starting with a high negative amplitude and increasing to a high positive amplitude. Further information on k-space sampling strategies can be found in [Henn 99].

2.2.2 From k-Space to Image Space

Each point in k-space corresponds to the acquired signal at a particular phase encoding gradient G_{ph} and acquisition time t_{acq} and contains information from all voxels in the slice. The k-space is translated into image space using the two-dimensional inverse Fourier transform as described in the following paragraphs. The MR signal $S(t_{acq}, G_{ph})$ induced in the receiver coil by the transverse magnetization under the gradient field G_{ph} at acquisition time t_{acq} reads as

$$S(t_{acq}, G_{ph}) = \iint_{\text{slice}} I(u,v) \mathrm{e}^{-i\Phi_{re}(u,t_{acq})} \mathrm{e}^{-i\Phi_{ph}(v)} \mathrm{d}u\mathrm{d}v, \tag{2.10}$$

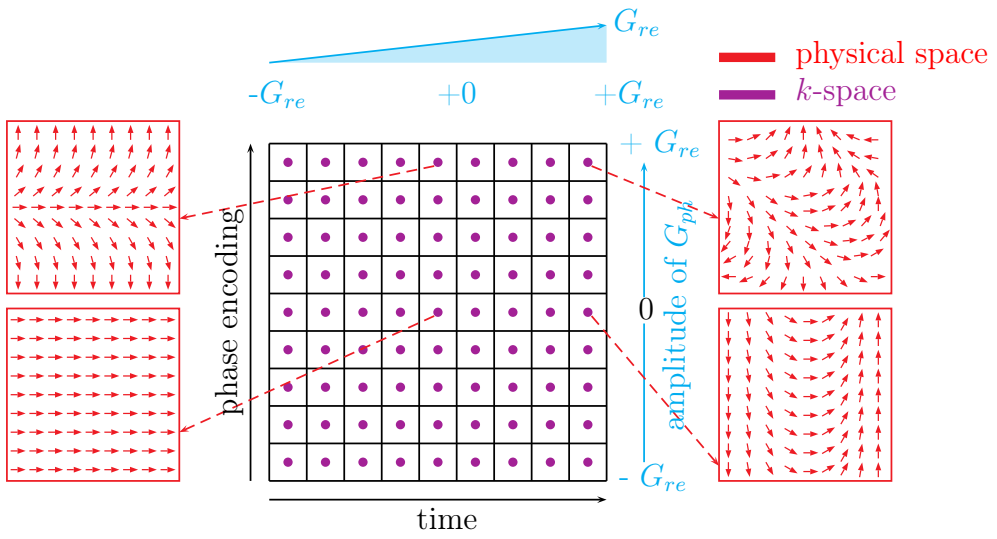

Figure 2.7: *Cartesian k-space sampling strategy. During each phase encoding step the MR signal is acquired at N_{re} readout time points generating one line in k-space. The size of the voxels is defined by N_{re}, the number of phase encoding steps N_{ph} and the size of the FOV. The phase encoding gradient G_{ph} is the only gradient that changes amplitude during the data acquisition loop. Adapted from [Huet].*

where $I(u, v)$ is the signal intensity at voxel (u, v). If we rewrite the phases as $\Phi_{re} = 2\pi\, u\, k_u$ and $\Phi_{ph} = 2\pi\, v\, k_v$ and take Eq. (2.8) and Eq. (2.9) into account, it becomes obvious that they define a position within the k-space matrix

$$k_u = \frac{\gamma}{2\pi} \int_0^{t_{acq}} G_{re}(\tau)\mathrm{d}\tau \ , \ k_v = \frac{\gamma}{2\pi} \int_0^{T_{ph}} G_{ph}(\tau)\mathrm{d}\tau. \tag{2.11}$$

Thus, the MR signal can be expressed as a function of k_u and k_v

$$S(k_u, k_v) = \iint I(u, v)\mathrm{e}^{-i2\pi(k_u u + k_v v)}\ \mathrm{d}u\mathrm{d}v, \tag{2.12}$$

$I(u, v)$ can now be calculated using the inverse two-dimensional Fourier transform by

$$I(u, v) = \iint S(k_u, k_v)\mathrm{e}^{i2\pi(k_u u + k_v v)}\mathrm{d}k_u\mathrm{d}k_v. \tag{2.13}$$

In the scope of this work, gray scale magnitude and phase images are used (Fig. 2.8). Magnitude images are calculated from Eq. (2.13) by

$$||I(u, v)||_2 = \sqrt{\mathrm{Re}(I(u, v))^2 + \mathrm{Im}(I(u, v))^2}, \tag{2.14}$$

and phase images by

$$\Phi(I(u, v)) = \arctan \frac{\mathrm{Im}(I(u, v))}{\mathrm{Re}(I(u, v))}, \tag{2.15}$$

where $||I(u, v)||_2$ is the magnitude and $\Phi(I(u, v))$ the phase of the measured MR signal at voxel (u, v).

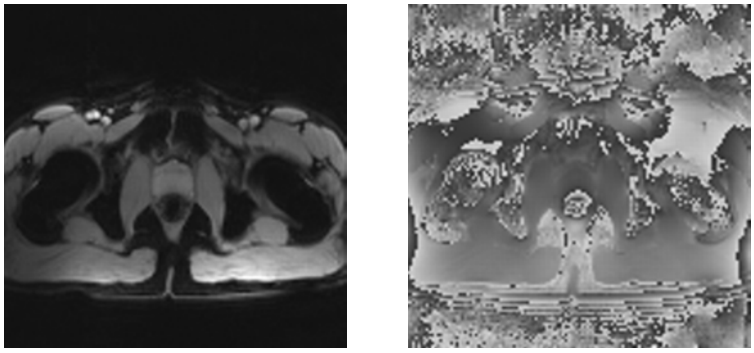

(a) Magnitude image (b) Phase image

Figure 2.8*: Magnitude and phase image of an axial slice acquired with a multishot EPI GRE sequence (Sec. 2.3.3) for MR thermometry in the prostate. (a) The magnitude values are proportional to gray levels on anatomical images. (b) Phase values relate to the proton resonance frequency.*

2.2.3 FOV and Spatial Resolution

The spatial resolution, i.e. voxel size, of an image can be enhanced by increasing the number of readout points N_{re}, the number of phase encoding steps N_{ph}, or decreasing the field of view FOV($\mathrm{L_{re}}, \mathrm{L_{ph}}$) which defines the image size in mm. The field of view along the readout direction (L_{re}) is given by

$$L_{re} = \frac{4\pi\Delta\nu}{\gamma G_{re}}, \tag{2.16}$$

where ν is the receiver bandwidth for which holds

$$2\Delta\nu = \frac{1}{\Delta t} = \frac{N_{re}}{T_{acq}}. \tag{2.17}$$

T_{acq} is the duration of data acquisition, Δt the signal sampling time and N_{re} the number of readout time points. The field of view along the phase encoding direction (L_{ph}) is given by

$$L_{ph} = \frac{4\pi(N_{ph}/T_{ph})}{\gamma G_{ph}}, \tag{2.18}$$

where T_{ph} is the duration and G_{ph} is the maximum amplitude of the phase encoding gradient.

Equations (2.16) and (2.18) indicate that the field of view is inversely proportional to the applied gradient. The field of view along the readout direction can be also modified by changing the receiver bandwidth. Decreasing the receiver bandwidth increases the SNR as Δt is increased (Eq. (2.17)). However, the image gets more susceptible to off-resonance artifacts due to the longer T_{acq}. The field of view along the phase encoding direction is directly proportional to N_{ph} (Eq. (2.18)). However, increasing N_{ph} increases total image acquisition time, proportionally. This shows that there is a always a tradeoff between spatial resolution, FOV, SNR, image acquisition time and artifacts. For each clinical application, an optimal protocol, i.e. set of MR imaging parameters for a specific pulse sequence, has to be found.

2.3 Pulse Sequences for Interventional MRI

For acquisition of an MR image a predefined set of RF pulses and gradients is repeated many times during a scan. The shape of the RF pulses and gradients and the timing of their operation is defined by so-called pulse sequences. Any MRI pulse sequence can be divided into three parts: The excitation, acquisition and end module. The pulse sequences used in this work belong to the family of gradient echo (GRE) pulse sequences. The interested reader is referred to Yutzy et al. [Yutz 08] and Derakhshan et al. [Dera 05] for further details on pulse sequences in interventional MRI.

2.3.1 Gradient Echo

GRE sequences were introduced in 1986 [Haas 86] and allowed for a significant increase in MR image acquisition time in comparison to spin-echo sequences [Bott 82] as they eliminated the need for 180° RF refocusing pulse and related waiting times. Figure 2.9 depicts a timing diagram of a GRE sequence.

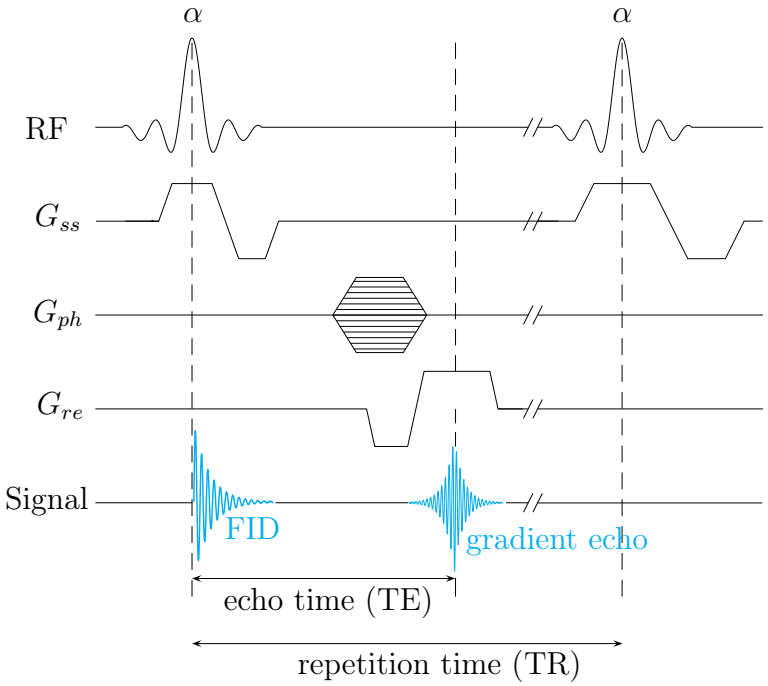

Figure 2.9: *Timing diagram of a gradient echo sequence. After excitation with an RF pulse with flip angle α and application of a slice selection gradient G_{ss}, phase encoding is accomplished by the gradient G_{ph}. The gradient G_{re} in readout direction dephases the spins before they are rephased. Data acquisition takes place during the gradient echo which reaches its maximum amplitude at* TE. *These steps are repeated at intervals of* TR *for each phase encoding step.*

In standard GRE imaging, the steps described in the following section are repeated as many times as image lines are acquired. The time interval between successive excitations is called repetition time (TR). The excitation module of a GRE sequence consists of an excitation pulse, called an alpha pulse. The flip angle α to which the net magnetization is tilted away from the axis of the main magnetic $\boldsymbol{B_0}$ is usually

between 0° and 90°. In general, a larger flip angle gives more T_1 weighting to the image, whereas a smaller flip angle gives more T_{2^*} weighting to the image. The signal acquired in a GRE sequence is the gradient echo of the FID generated by inverting the readout gradient prior to data acquisition. The spins are dephased before they are rephased by an equal but opposite gradient which generates a gradient echo at the time when the areas under the positive and negative gradients are equal. The MR signal is sampled during this induced gradient-echo. The time between the application of the RF pulse and the peak of the gradient echo is known as the echo time (TE). The end module is either absent or consists of additional gradients or RF pulses in order to spoil, i.e. destroy, any remaining transverse magnetization or to refocus the transverse magnetization at the time when the spin system encounters the next excitation RF pulse. Spoiled gradient echo sequences, called fast low-angle shot (FLASH) on Siemens MR scanners, produce images with a T_1 weighted contrast.

2.3.2 Balanced Steady-state Free Precession

For real-time needle guidance in this work a balanced steady-state free precession (SSFP) GRE sequence is used. Steady-state free precession refers to the fact that M_z does not fully recover between application of RF excitation pulses and M_{xy} reaches a nonzero steady-state just before application of each RF excitation pulse. To establish this steady-state, a TR shorter than T_{2^*} is needed. Balanced SFFP GRE sequences have been proposed in 1986 [Oppe 86], however only recent advances in gradient hardware allowed to achieve repetition times in the range of 3-6 ms. This very short TR is needed to minimize banding artifacts, i.e. spatial regions where a signal loss occurs (Fig. 2.10) due to off-resonance effects induced by $\boldsymbol{B_0}$ inhomogeneity (Sec. 2.4.2). From the very short TR follows a short image acquisition time (2-5 fps) which makes balanced SSFP GRE very interesting for real-time device guidance. The very high SNR further allows to work with parallel acquisition methods [Prue 99, Gris 02] with an acceleration factor of 2 or greater. In addition, balanced SSFP GRE sequences provide a T_2 over T_1 weighted image contrast with a maximized fluid signal at flip angles of $70° - 90°$. This allows for a high lesion conspicuity [Numm 03] and a strong contrast between tissue with different T_1 and T_2 relaxation times, e.g. high contrast between muscle and blood. This is important for needle placement as large blood vessels are structures which should not be accidentally punctured. Further information on balanced SSFP GRE sequences, called TrueFISP on Siemens MR scanners, can be found in [Sche 03].

2.3.3 Echo Planar Imaging

Echo planar imaging (EPI) [Mans 77] allows to dramatically accelerate image acquisition speed as the transverse magnetization M_{xy} is maximally used without application of additional RF excitation pulses. It is based on the principle of generating a series of gradient echoes before M_{xy} decays away by application of a bipolar oscillating readout gradient. Thus, multiple k-space lines can be acquired in a single RF excitation leading to an image acquisition time of only a few tens of milliseconds. As balanced SSFP, EPI places stringent requirements on system hardware.

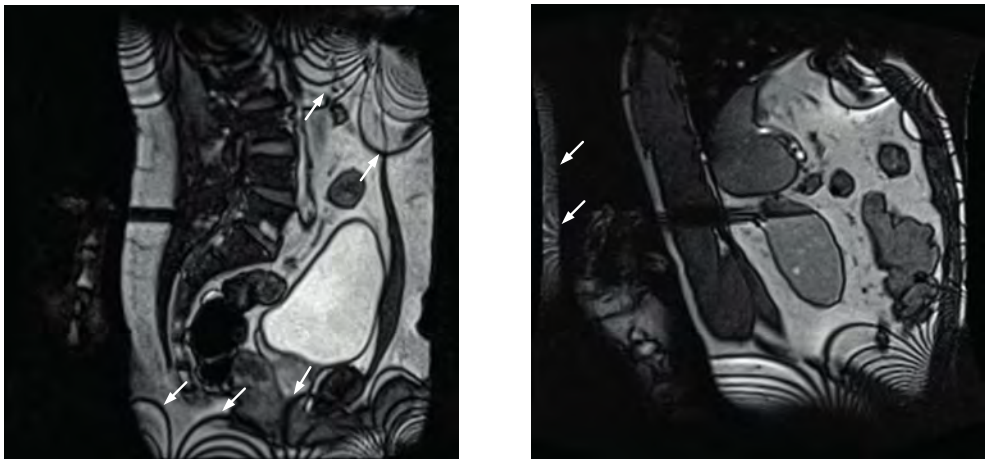

(a) Spinal infiltration (b) Cryoablation needle placement

Figure 2.10*: Real-time needle placement using a balanced SSFP GRE sequence (*TE *2.2 ms,* TR *X ms, flip angle* 50°*, receiver bandwidth 302 Hz/Pixel, acquisition time 0.8 sec) at a 1.5T MR scanner. The arrowheads point to banding artifacts resulting from off-resonance effect in (a) and to wrap around artifacts in (b).*

EPI allows for excellent temporal resolution, but the rapid sampling requires a high receiver bandwidth which drops SNR (compare Sec. 2.2.3). Also spatial resolution is compromised as it depends on gradient amplitude whose maximum is limited due to the rapid gradient switching. However, spatial resolution in echo planar imaging can be increased by using multishot EPI sequences instead of single shot where the entire 2-D k-space is acquired in one single RF excitation, called shot. Multishot EPI sequences (image example in Figure 2.8) acquire a fraction k-space in each RF excitation. This increases SNR and makes the image less prone to ghosting artifacts but at the same time multishot EPI sequences are more sensitive to motion due to the increased acquisition time.

2.4 Image Artifacts in Interventional MRI

In this section common artifacts in interventional MRI are described and the basic physical background on their formation is given to allow for the understanding of reduction strategies. Focus is put on artifacts resulting from aliasing, $\boldsymbol{B_0}$ inhomogeneity and magnetic susceptibility differences as they play an important role for both workflow and algorithm development in this work.

2.4.1 Aliasing

Aliasing artifacts occur if the sampling rate is not at least twice the highest frequency component within the aggregate MR signal, i.e. when objects outside the FOV are excited. When this so-called Nyquist-Shannon theorem is not met, the Fourier transform will assign signal from outside the FOV to frequencies lower than the actual signal component they derive from, leading to wrap-around as illustrated in Figure 2.11. Aliasing artifacts can occur in both the frequency and phase encoding directi-

on, however in the frequency direction one can oversample, i.e. increase the number of frequency encoding steps, with no increase in image acquisition time. Thus, one should carefully select the phase encoding direction and per default oversample in the frequency encoding direction.

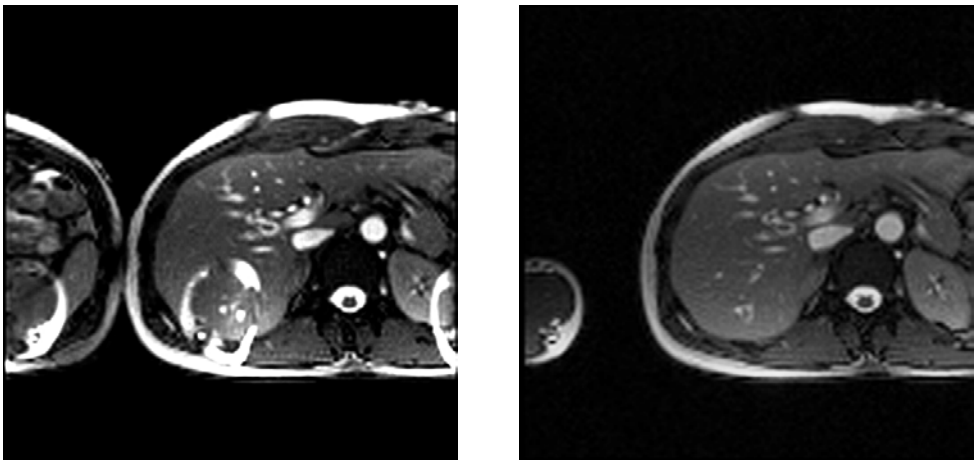

(a) L-R phase encoding direction (b) A-P phase encoding direction

Figure 2.11*: Aliasing artifact. (a) Signal outside the FOV is undersampled along the phase-encoding direction and assigned a frequency corresponding to locations inside the FOV, the subject's left arm and left body part are wrapped around. (b) Same slice as (a) but with A-P phase encoding direction and oversampling along the frequency encoding direction.*

2.4.2 B_0 Inhomogeneity and Magnetic Susceptibility

Spatial encoding in magnetic resonance imaging heavily relies on a homogeneous magnetic field (Sec. 2.1.3). Inhomogeneties, i.e. point-to-point variability in magnetic field strength, cause neighboring spins to precess at a range of frequencies with the result of signal loss due to dephasing and geometric distortions due to frequency shifts.

Changes in local magnetic field strength arise from both system- and patient-induced effects. System-induced inhomogeneties get stronger at the periphery of the field, so one should always scan as close as possible to the isocenter. Patient-induced effects are due to magnetic susceptibility (Eq. 2.4) and chemical shift. Magnetic susceptibility gradients occur at interfaces between substances with different susceptibility values, such as air-bone, bone-tissue interfaces, and can also be caused by metal objects, such as needles. As illustrated in Figures 2.12 to 2.14, the induced needle artifact is strongly dependent on the sequence type, echo time, receiver bandwidth, phase encoding direction, and needle orientation with respect to $\boldsymbol{B_0}$. All needle artifact images have been acquired with a specially designed and built phantom, see Figure 3.20. Further information on needle artifacts in MRI can be found in [Ladd 96, Lewi 96, Koli 04].

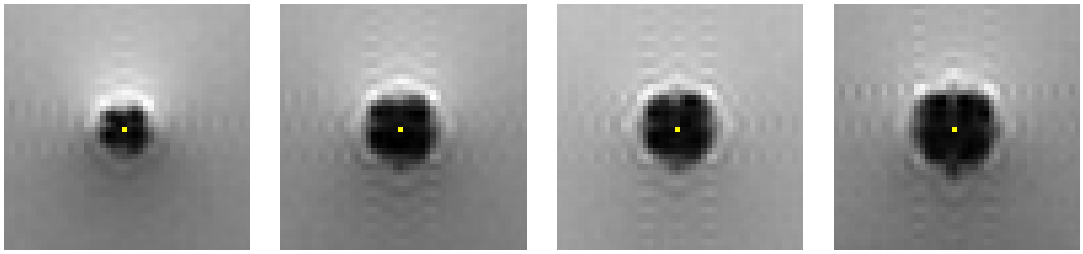

(a) 5 ms (b) 15 ms (c) 20 ms (d) 25 ms

Figure 2.12: *Influence of echo time on artifact size of 17G cryoneedle (marked in yellow). Images were acquired at 1.5T using a GRE sequence with bandwidth 601 Hz/Px.*

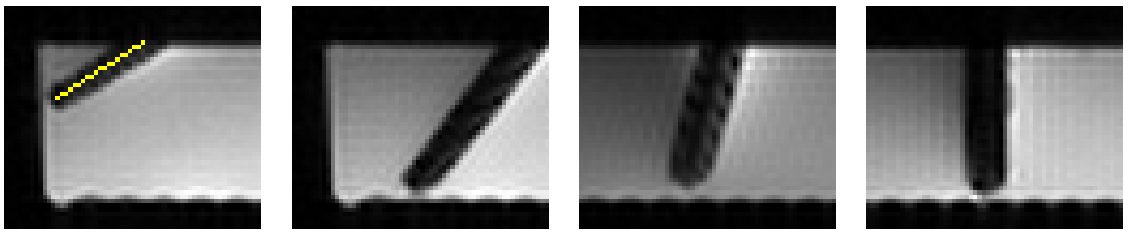

(a) 30° (b) 50° (c) 75° (d) 90°

Figure 2.13: *Influence of needle orientation with respect to $\boldsymbol{B_0}$ on artifact size of 17G cryoneedle (marked in yellow). Images were acquired at 1.5T using a GRE sequence with TE 5 ms and bandwidth 601 Hz/Px.*

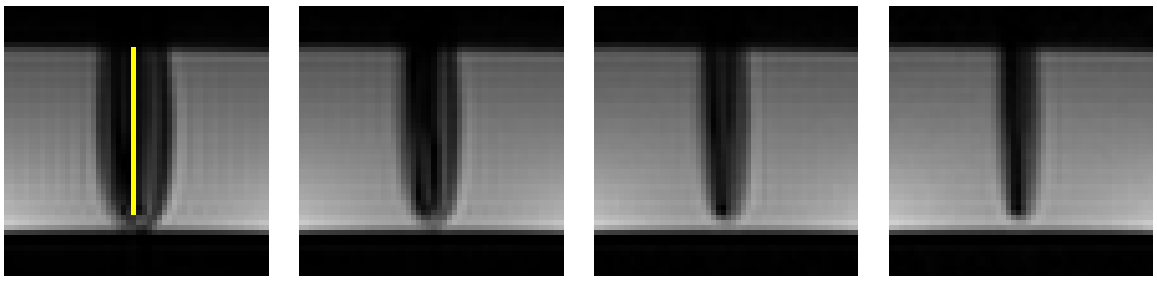

(a) 130 Hz/Px (b) 250 Hz/Px (c) 501 Hz/Px (d) 1002 Hz/Px

Figure 2.14: *Influence of receiver bandwith on artifact size of 17G cryoneedle (marked in yellow).*

2.4.3 Slice Overlap Artifact

As the name suggests, slice overlap artifacts occur if slices are overlapping in a multi-slice acquisition. Protons belonging to more than one slice get saturated and cause a saturation band, i.e. a band of signal loss. In this work, the slice overlap artifact is extensively exploited for real-time needle guidance as described in Section 3.2.4. The section also provides images illustrating the artifact.

2.5 Summary

MR is an attractive imaging modality for guiding percutaneous interventions due to its superior soft-tissue contrast and multi-planar imaging capabilities without the use of any ionizing radiation.

The superior soft-tissue contrast is based on the fact that the MR signal is influenced by several tissue characteristics including T_1, T_2 and T_{2^*} relaxation times and proton density. Those parameters vary significantly between tissue types allowing for a clear discrimination between soft tissues, and between pathological and normal tissue. The image contrast can be enhanced by using contrast media like gadolinium which shortens T_1 and T_2 relaxation times in tissues in which it accumulates [Nels 95]. Variable image contrast can further be achieved by using different pulse sequences and by changing the imaging parameters (such as TR, TE and flip angle α). In this work, a balanced steady-state free precession GRE sequence is used for needle placement which allows for image acquisition at 2-5 frames per second. For real-time MR temperature measurements an echo planar GRE imaging sequence is used which allows for acquisition of several lines up to the entire k-space in one TR and thus can minimize intra-scan motion.

The multi-planar imaging capabilities of MR result from the fact that spatial encoding is based on playing out magnetic field gradients which can be oriented freely in space. Thus, in contrast to X-ray or CT, MR allows to directly image in any orientation without having to reconstruct the image from a stack of images. This is of particular advantage for real-time imaging of needle advancement along double-oblique trajectories.

MR imaging provides unparalleled flexibility in image acquisition but is also prone to a wide range of imaging artifacts [Miro 99, Bern 06] which make MR more complex to use than other imaging modalities. For algorithm design in this dissertation, artifacts arising from aliasing, saturation effects due to overlapping slices, $\boldsymbol{B_0}$ inhomogeneity, and magnetic susceptibility are of major importance.

Real-time MR-guided Needle Placement

3

The number of percutaneous interventional procedures being performed under MR guidance [Tatl 07] is increasing. Such procedures include aspiration [Lewi 00, Saka 03], biopsy [Weis 08, Hoff 12], sclerotherapy [Boll 04], targeted drug delivery [Frit 09] and thermal ablation [Morr 08, Wack 98, Nour 10, Rick 10]. However, over twenty years after the introduction of interventional MRI [Muel 86], these procedures are still performed primarily at academic hospitals. One of the barriers to more widespread adoption is the lack of a streamlined workflow and the complexity with respect to oblique and orthogonal slice prescriptions.

This chapter starts by giving an overview of guidance concepts in the area of MR-guided percutaneous interventions. It then presents image-based methods developed within this thesis for improving the workflow of freehand MR-guided percutaneous needle interventions. The general goal was to introduce no additional hardware for guidance but to make use of the susceptibility artifact created by the device (Sec. 2.4.2) for guiding accurate needle positioning. The methods presented in Section 3.2 have been integrated within a clinical research prototype (Sec. 4.3) which is currently used at 21 sites worldwide. Section 3.3 and 3.4 give an outlook about how those methods could be further improved. Major parts of this chapter have been published in a journal paper [Roth 13] and in conference proceedings [Roth 12b, Roth 11a, Stre 09] cited throughout the text.

3.1 Guidance Concepts

MR-guided percutaneous procedures have been performed for over 20 years using a variety of methods. The freehand technique (Sec. 3.1.1) is the simplest and most common approach for MR-guided percutaneous needle interventions. Motivated by the restricted patient access inside the MR scanner bore and the aim of achieving higher accuracy, various MR-compatible guidance systems have further been developed over the last years (Sec. 3.1.2).

3.1.1 Freehand Technique

The freehand technique most closely approximates the typical workflow for CT- or US-guided needle placements and requires no special equipment beyond a commercially available MR-compatible needle. Since the early clinical studies of MR-guided percutaneous procedures [Lu 97, Lewi 99] it is the most commonly used approach. See

Table 5.3 for an overview of recent clinical studies. The freehand technique is comprised of four basic steps, namely trajectory planning, skin entry point localization, targeting, and needle placement verification, each of which can present significant challenges to the operator.

Planning and Entry Point Localization

Trajectory planning is typically performed by prescribing a single oblique trajectory using a stack of axial, coronal or sagittal images. However, not all lesions, e.g. in the hepatic dome, can be accessed with the entry point being in the same slice as the target point. Methods are therefore needed to improve double-oblique trajectory planning and review capabilities.

Although skin entry point localization sounds straightforward, it consists of multiple, often time-consuming steps including placing a skin marker over the expected area of interest, acquiring a planning scan, measuring the distance of the skin entry site from the marker, moving the marker to the measured location and re-acquiring the initial planning scan. Once close, the skin entry point may be located using a fingertip or water-filled syringe [Lewi 00, Stat 08b, Fisc 11, Frit 09, Gena 02] as shown in Figure 3.1.

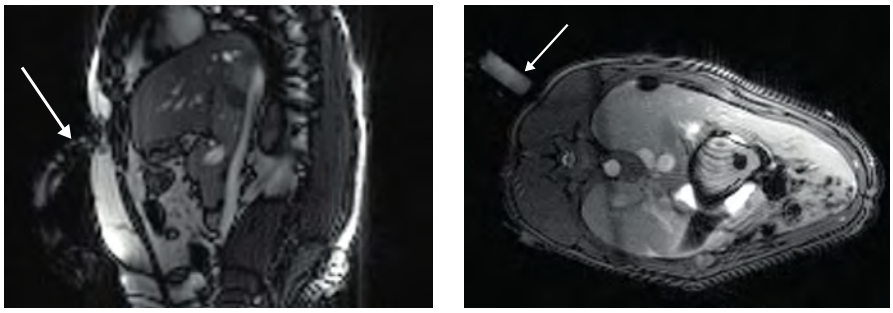

(a) Fingertip (b) Water-filled syringe

Figure 3.1*: Entry point localization is usually performed under continuous imaging using a (a) fingertip or (b) water-filled syringe (see arrows). Accurate and reproducible entry point localization can be challenging and time-consuming.*

Targeting and Needle Placement Verification

There are two approaches for freehand targeting. Needle advancement can either be performed using an in-and-out approach [Lu 97], i.e. moving the patient in for verification images and out for needle adjustments, or under continuous real-time MR image guidance. The in-and-out approach is intrinsically slower than real-time image guidance and can be challenging in particular for moving organs as the needle is not advanced under continuous imaging. Its advantage of not having to work inside the confined space of the MR scanner bore is mitigated by the introduction of wide-bore scanners.

For the increasingly common approach of advancing the needle under continuous MR image guidance, accurate real-time slice alignment is essential for continuous visualization of the entire needle, target lesion, and surrounding anatomy. Manual

slice alignment, even with an experienced team, can be confusing and time-consuming for both the interventionalist and the MR technician and becomes more so when attempting a complicated trajectory [Stat 08a]. In addition, it is still common to use only one [Stat 08b, Frit 08, Frit 09] or two alternating image slices, i.e. to continuously switch between two slices [Fisc 11, Stre 10, Rick 10], for real-time needle guidance. Thus, the needle advancement is only visualized in one slice at a time which can make it difficult to maintain the prescribed trajectory (Fig. 3.2a), in particular for double-oblique trajectories [Stat 08b].

To verify the correct needle position, pre-placement planning and post-placement verification datasets are usually visually compared by manual slice selection and zooming/translating as shown in Figure 3.2b. This is time-consuming and only allows to roughly estimate the needle placement accuracy.

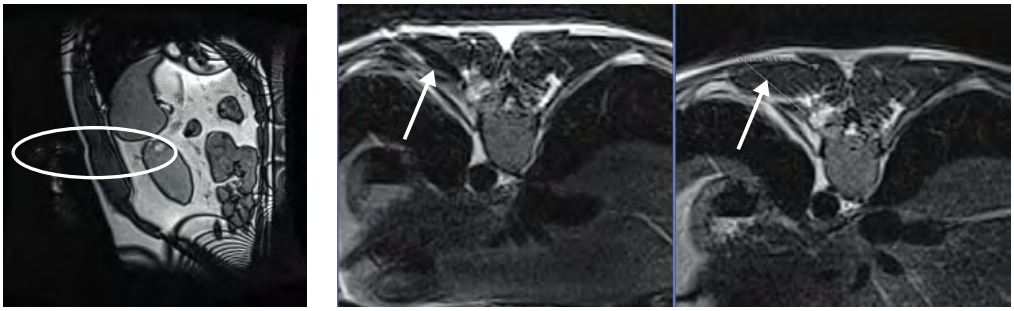

(a) Targeting (b) Needle placement verification

Figure 3.2*: Challenges in current MR-guided needle placement workflow. (a) Using only one real-time slice for guidance, it can be difficult to maintain the planned trajectory. The ellipse highlights the area where the needle is supposed to be. (b) Visual comparison between actual and planned needle path (marked by arrows).*

3.1.2 Navigation and Robotic Assistance Systems

Numerous navigation and robotic assistance systems for use in the MR environment have been developed over the past years [Moch 08]. The optimal choice of system is dependent on the requirements of the specific procedure.

Navigation Systems

Navigation systems aim to aid the physician by tracking the device and continuously visualizing its position with respect to the patient. They can be grouped into systems which work inside or outside the bore. For working outside the bore, and thus having easier access to the patient, augmented reality, optical tracking, and bi-plane laser systems have been proposed (Fig. 3.3). Images used for guidance are reformatted according to the tracked needle orientation from a 3-D dataset acquired in a preceding planning step. One of the challenges is exact registration of patient and image data. Due to the static reference data, these systems are not well suited for regions affected by cardiac or respiratory motion. For applications where real-time imaging is necessary, navigation systems which work inside the bore, and thus allow for real-time

imaging during needle positioning, have been developed. The systems are designed with the goal to continuously visualize the needle and interactively adapt the scan planes with respect to the tracked needle position. Besides optical tracking (Fig. 3.4a) systems with markers attached to the needle which can be detected with special MRI pulse sequences have been proposed (Fig. 3.4b and 3.4c). For all systems, the update rate needs to be carefully determined as it can be very confusing if the scan planes constantly jump around during needle positioning. For optical tracking inside the bore an unobstructed line of sight if further necessary.

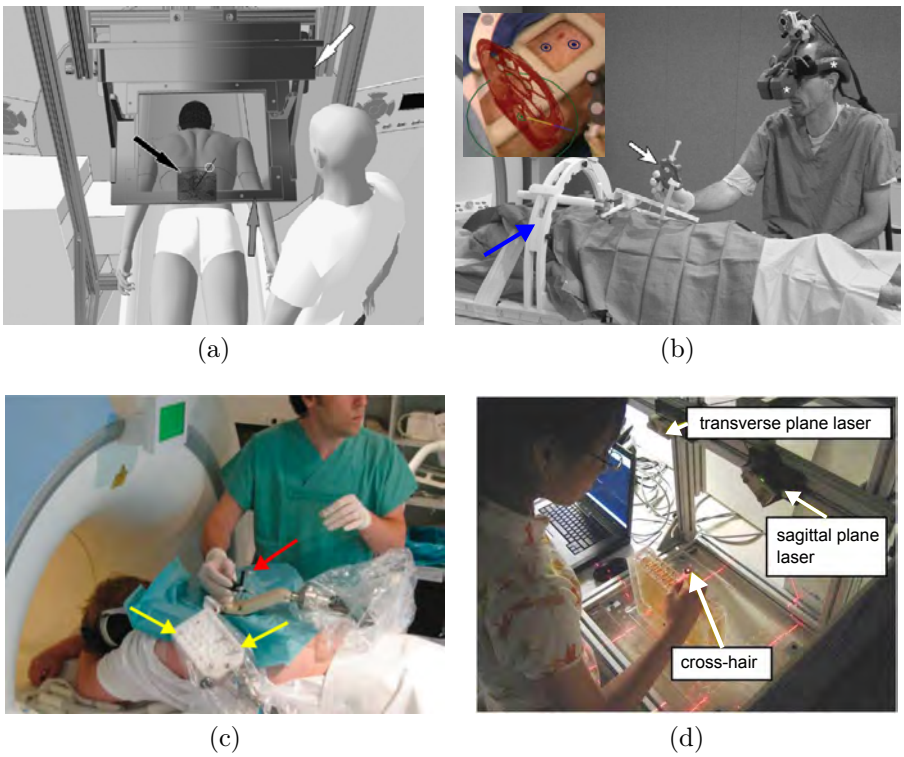

(a) (b) (c) (d)

Figure 3.3: *Guidance systems for needle placement outside the MR scanner bore. (a) Image overlay system with targeting image shown in the inlay [Fisc 07a, U Th 13]. Image reproduced from [Frit 12] with permission from Wolters Kluwer Health. (b) Augmented reality system with reference frame (blue arrow) and augmented reality view shown in upper left corner. Image adapted from [Wack 06], reproduced with permission from Radiology. (c) Optical tracking system for device navigation. The needle can be followed with respect to previously acquired MR images on an in-room screen. The mapping between coordinate systems is achieved with optical (yellow arrows) and MR visible (red arrow) markers integrated into the reference board. Image reproduced from [Buss 12] with permission from John Wiley and Sons. (d) Bi-plane laser guide in which needle axis is delineated by intersection of laser planes [Fisc 07b]. No image feedback is provided. Image reproduced from [Vika 10] with permission from Elsevier.*

(a) (b) (c)

Figure 3.4: *Guidance systems for needle placement inside the MR scanner bore under continuous imaging. (a) Experimental setup for optical needle tracking inside the bore for real-time image-guided needle placement. Image reproduced from [Gttl 10] with permission from Felix V. Güttler. (b) Active tracking system based on MRI gradient fields (EndoScout, Robin Medical). A sensor (arrow) with integrated miniature coils is attached to the needle. Image reproduced from[Staf 09] with permission from ISMRM. (c) Passive marker (arrow) attached to the needle is automatically tracked by a special pulse sequence. Image reproduced from [De O 08] with permission from John Wiley and Sons.*

Robotic Assistance Systems

One goal of robot-assisted needle placement is to increase targeting precision by allowing for needle placement under continuous imaging also in targets which are hard to reach manually when the patient is inside the MR scanner bore. However, building robots for the MR environment is challenging as it is necessary to ensure full MR compatibility, i.e non-metallic components, pneumatic actuation, piezoelectronics and markers for registration with the MR scanner coordinate system. The design of the robots further needs to account for the limited space in the scanner bore.

Research in the area of MR-compatible robotic assistance systems is currently mainly focused on neurosurgery [Suth 08] and prostate interventions [Krie 05, Macu 08, Moze 09]. A detailed review of MR-compatible robotic systems is provided by Tsekos et al. [Tsek 07] and by Elhawary et al. [Elha 08]. In general, the proposed robots require extensive setup before the procedure and are usually very focused on one application. Several clinical studies have been performed in the field of robotic-guided MR prostate biopsies [Xu 10, Yaka 11, Zang 11, Scho 12], an example for such a system is given in Figure 3.5. However, so far only the Innomotion robot [Hemp 03] is commercially available for use in the MR environment.

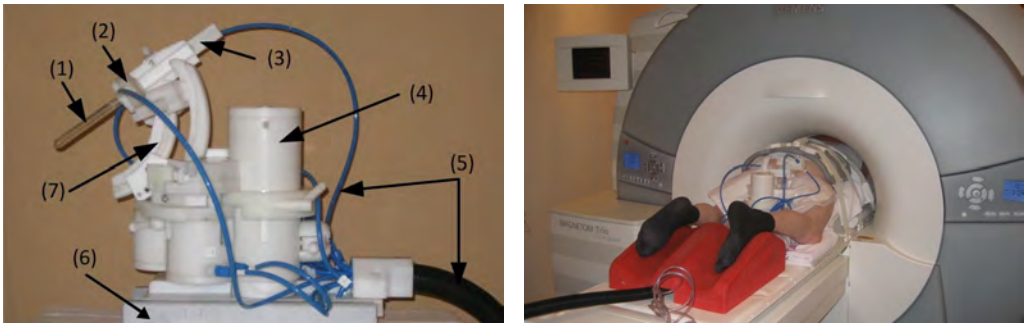

(a) (b)

Figure 3.5: *Robotic needle placement inside the MR scanner bore. (a) Pneumatic controlled robot with five degrees of freedom (1) needle guide, (2) safety mechanism with suction cup, (3) tapping mechanism to introduce needle guide, (4) pneumatic motor, (5) tubings to the motor, (6) ground plate for mounting on the MR scanner table, (7) angulation rail to move the needle guide in the coronal plane. (b) Patient setup on the MR scanner table (Siemens MAGNETOM Trio 3 T) with robot in place. Images reproduced from [Scho 12] with permission from Springer.*

3.1.3 Passive versus Active Visualization

Most needles used today for MR-guided percutaneous interventions are passively visualized, i.e. appear as a dark line in the MR image. This artifact is due to the different magnetic susceptibility of the needle with respect to the surrounding tissue leading to the small inhomogeneties in the local magnetic field $\boldsymbol{B}_i$ and thus signal loss. The needle artifact appearance can vary widely depending on the orientation relative to $\boldsymbol{B_0}$, material composition, and imaging sequence as illustrated in Section 2.4.2. In contrary, active devices have small RF coils or antennas incorporated which are connected to the MR scanner and detect signal only from the spins near the coil. The three-dimensional (3-D) position of the device can be determined by acquisition of orthogonal projection images with the slice selection gradient being switched off, i.e. infinite slice thickness [Dumo 93, Geor 10]. An example for an active needle is shown in Figure 3.6.

(a) (b) (c)

Figure 3.6: *Active needle with (a) incorporated loop antenna and tighter cooper coil windings, (b) interface box for connection with the MR scanner. Images are reproduced from [Saik 11] with permission from John Wiley and Sons. (c) Device projection image overlaid on anatomic image. Image reproduced from [Barb 11] published under the Creative Commons Attribution License.*

3.2 Methods for Improving the Workflow

The goal was to improve and streamline the workflow of freehand MR-guided percutaneous needle interventions by developing purely image-based methods without introducing any additional equipment. Focus was put on target locations which require a highly angulated approach and cannot be easily reached using CT or US guidance. An overview of the developed methods and their interrelation is given in Figure 3.7. An extensive *in-vitro* and *in-vivo* validation of the developed methods is presented in Chapter 5.

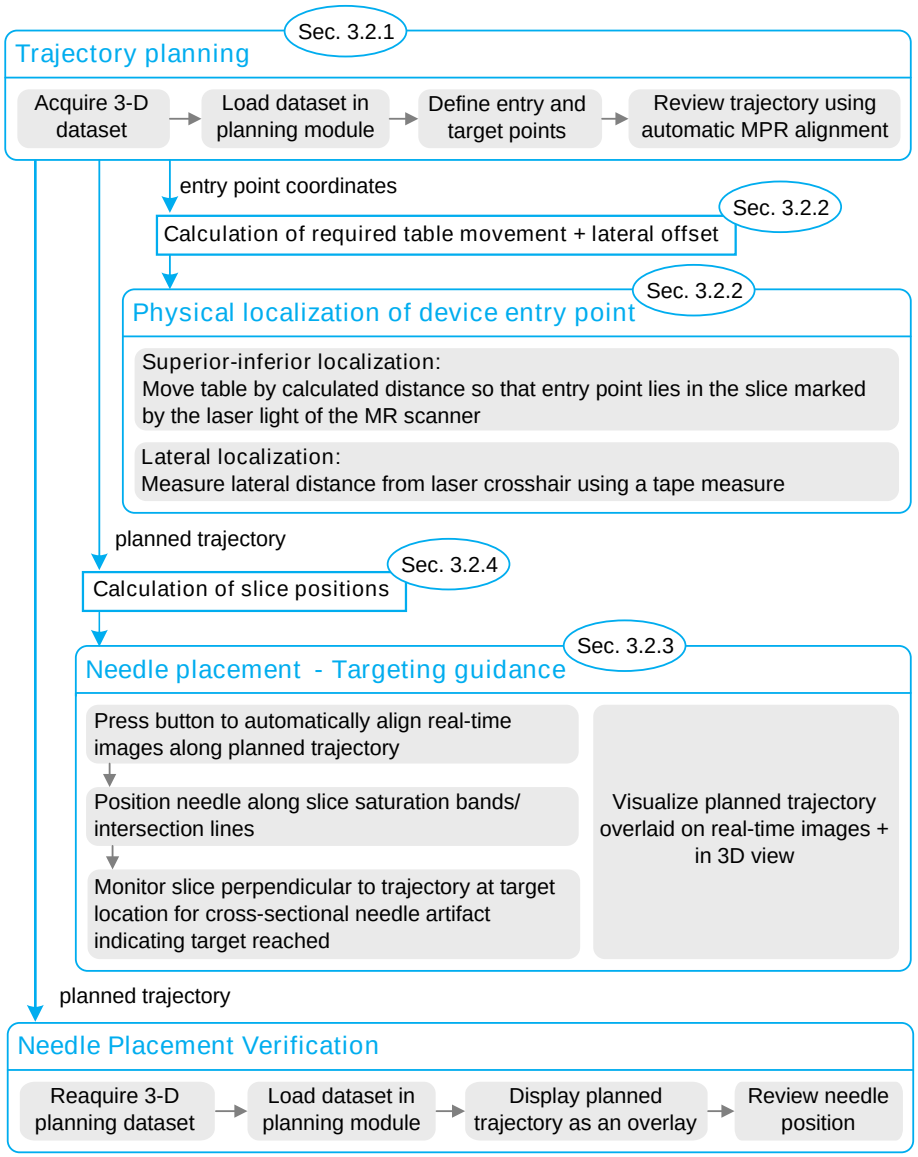

Figure 3.7: *Proposed workflow for rapid freehand MR-guided percutaneous needle placement. A detailed description of the developed methods can be found in the referenced sections. In a procedure where no precise measurement of targeting accuracy is necessary, the verification step could be also replaced by acquisition of a few slices enclosing the lesion.*

3.2.1 Volumetric Trajectory Planning

Current MR scanners do not provide any dedicated features for planning a needle trajectory. A workaround is to use the measurement tool for drawing a line on a 2-D image in order to get an idea of trajectory length and angulation. However, this does not provide any information about the entry and target point location in the patient-centered coordinate system (PCS) which is needed for physical entry point localization and visualization of the planned trajectory in real-time images during targeting. In addition, it is challenging to plan double-oblique trajectories or to review the planned path ensuring no sensitive structures are hit. Thus, the goal was to develop a tool which improves both planning and reviewing of trajectories and allows to incorporate the planning information into the subsequent workflow steps, that is physical entry point localization (Sec. 3.2.2) and targeting (Sec. 3.2.3).

Trajectory Definition

The developed clinical prototype is capable of displaying highly-resolved 3-D MR datasets using multi-planar reformatting (MPR), maximum intensity projection (MIP) and volume rendering (Fig. 3.8). Entry point $\boldsymbol{p}_\mathrm{e}$ and target point $\boldsymbol{p}_\mathrm{t}$ can be defined with a mouse click in MPRs of any orientation and do not have to be in the same MPR. This is of particular importance for double-oblique trajectory planning as it allows to work with image planes in conventional orientations (Fig. 3.9a and 3.9b) instead of highly angulated planes (Fig. 3.9c) which can be hard to read. In many minimally invasive procedures it is further necessary to place several needles. The spatial relation of them with respect to each other plays an important role for treatment success, e.g. the applicator layout in thermal ablations defines size and shape of the necrosis zone. The developed prototype facilitates the planning of multiple trajectories in one session and visualization of them with respect to each other (Fig. 3.8b). This allows for a "plan once, scrub once" procedure strategy which is helpful for decreasing procedure time.

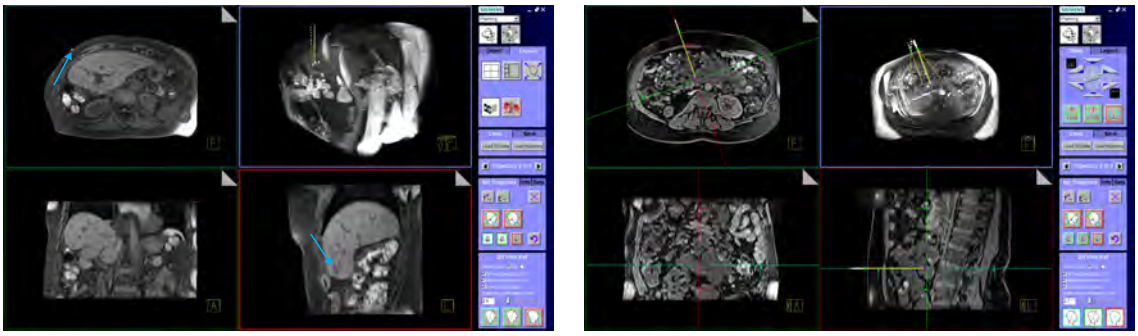

(a) Planning of double-oblique trajectories (b) Planning of multiple trajectories

Figure 3.8: *Screen captures of developed planning tool. (a) Planning of a double-oblique trajectory for RF applicator placement in the liver. Entry and target point (see arrows) are set in MPRs of different orientations. (b) Planning of needle placement for sclerotherapy of a complex intra-peritoneal venous malformation. The MIP (upper right) shows the orientation of the planned trajectories in space. All four needle paths were planned in one session.*

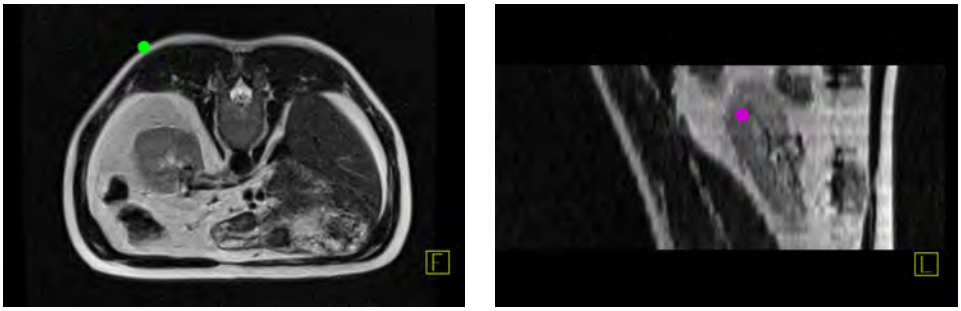

(a) Selection of entry point in axial slice (b) Selection of target in sagittal slice

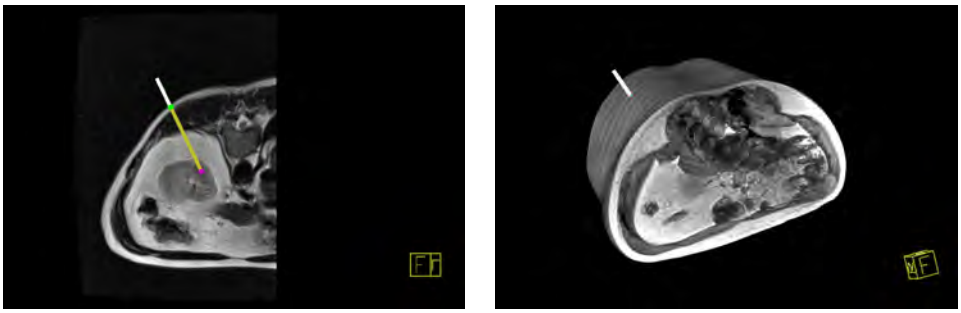

(c) Resulting double-oblique trajectory (d) Volume rendering view

Figure 3.9: *Trajectory planning for a kidney biopsy. (a) - (b) Selection of entry and target points in planes orientated along the principal patient axes. (c) MPR aligned along the planned double-oblique trajectory. (d) Volume rendering showing orientation of needle with respect to patient's body.*

Trajectory Review Using Automatic MPR Alignment

For an effective and safe procedure, it is important to have tools which allow accurate reviewing of planned trajectories. To improve reviewing capabilities, an automatic slice alignment algorithm (Sec. 3.2.4) was developed which aligns two planes along the needle and one orthogonal to them at the planned target location with preference to the principal patient axes. This MPR layout allows the user to fly along the prescribed trajectory making sure no sensitive structures are harmed during device insertion as illustrated in Figure 3.10.

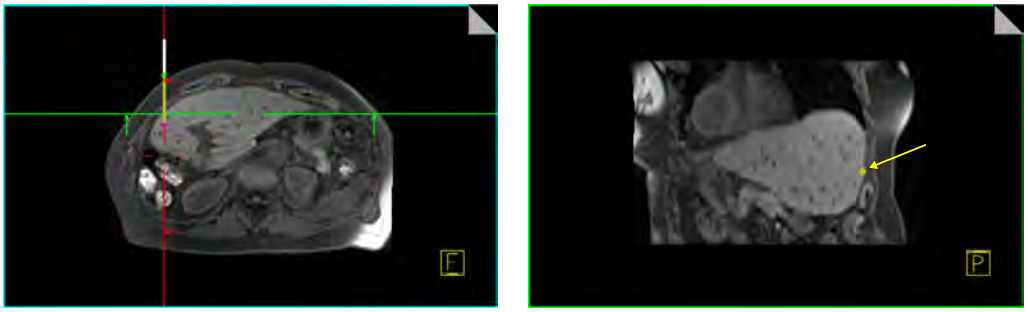

(a) Slice position with respect to trajectory (b) Intersection with planned trajectory

Figure 3.10: *Trajectory review by moving the green slice along the planned trajectory. The yellow dot (see arrow) in the green slice shows the intersection with the trajectory.*

Mapping of Selected Entry Point to 3-D Coordinates

For physical entry point localization, the entry pixel location $\hat{\boldsymbol{p}}_\mathrm{e} = (u_\mathrm{e}, v_\mathrm{e})^\mathrm{T}$ selected in an MPR in the planning tool needs to be mapped to 3-D coordinates $\boldsymbol{p}_\mathrm{e} = (x_\mathrm{e}, y_\mathrm{e}, z_\mathrm{e})^\mathrm{T}$ in the PCS (Fig. 3.11a). $\boldsymbol{p}_\mathrm{e}$, given in mm, is calculated by

$$\begin{pmatrix} x_\mathrm{e} \\ y_\mathrm{e} \\ z_\mathrm{e} \\ 1 \end{pmatrix} = \begin{pmatrix} x_\mathrm{c}\Delta c & x_\mathrm{r}\Delta r & 0 & x_\mathrm{t} \\ y_\mathrm{c}\Delta c & y_\mathrm{r}\Delta r & 0 & y_\mathrm{t} \\ z_\mathrm{c}\Delta c & z_\mathrm{r}\Delta r & 0 & z_\mathrm{t} \\ 0 & 0 & 0 & 1 \end{pmatrix} \cdot \begin{pmatrix} u_\mathrm{e} \\ v_\mathrm{e} \\ 0 \\ 1 \end{pmatrix}, \tag{3.1}$$

where u_e is the column index , v_e the row index of the entry point, Δc the column pixel resolution in mm, and Δr the row pixel resolution in mm. $\boldsymbol{r} = (x_\mathrm{r}, y_\mathrm{r}, z_\mathrm{r})^\mathrm{T}$ and $\boldsymbol{c} = (x_\mathrm{c}, y_\mathrm{c}, z_\mathrm{c})^\mathrm{T}$ are the row and column unit vectors spanning the image plane at distance $\boldsymbol{t} = (x_\mathrm{t}, y_\mathrm{t}, z_\mathrm{t})^\mathrm{T}$ from the origin of the PCS. $\boldsymbol{r}$ and $\boldsymbol{c}$ are stored in the Image Orientation Patient field of the DICOM header, $\boldsymbol{t}$ in the Image Position Patient field. For further information see the DICOM standard, Section C.7.6.2.1.1 [Digi 09].

3.2.2 Entry Point Localization

Physical entry point localization on the patient's skin using a water-filled syringe or fingertip can be time-consuming and challenging with respect to accuracy and reproducibility. Thus, the aim was to directly apply the planned trajectory (Sec. 3.2.1) to skin entry site localization without further imaging using solely the built-in laser and image processing methods [Roth 12b]. The landmark laser is part of any MR scanner and is originally used for defining a position on the object that when moved into the magnet coincides with the isocenter of the magnet. This landmarking step also defines the origin of the PCS which is used by the DICOM standard (Fig. 3.11). Thus, the 3-D coordinates of the entry point $\boldsymbol{p}_\mathrm{e}$, prescribed in the planning step, define a unique location on the patient. A two-step approach, divided into superior-

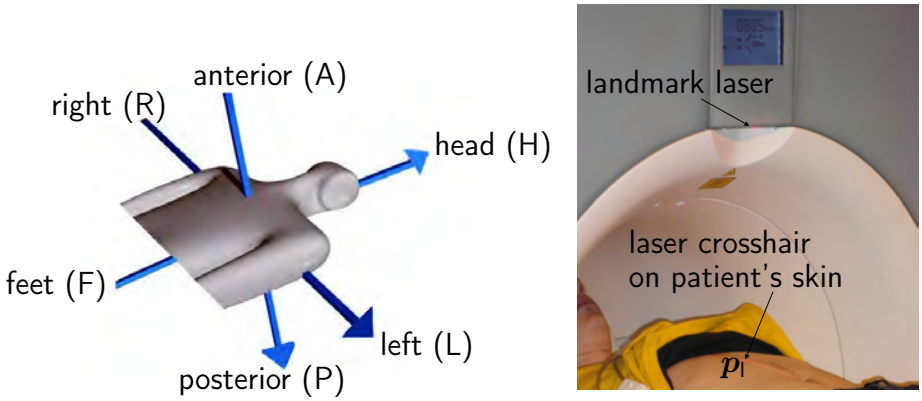

(a) Patient centered coordinate (PCS) system

(b) Landmark laser

Figure 3.11: *(a) The DICOM standard works with a patient-centered coordinate system (PCS) which is a right-handed and based on the patient's main body axes. (b) In MRI the origin of the PCS is defined with the built-in landmark laser.*

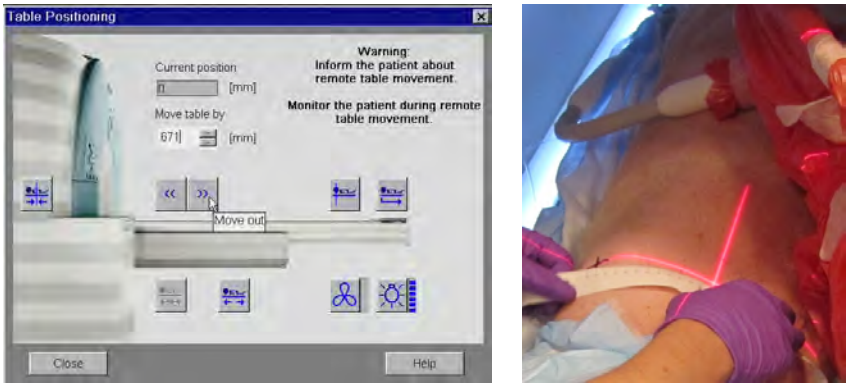

(a) Superior-inferior localization (b) Lateral localization

Figure 3.12: *Two-step approach for physical entry point localization. Distance to move the table (a) and lateral offset from the laser crosshair $\boldsymbol{p}_l$ (b) are calculated by the proposed algorithm.*

inferior and lateral localization, is proposed to physically locate the entry site on the patient without the need for any additional hardware.

1. Superior-Inferior Localization

The first step is to translate the MR scanner table so that the landmark laser delineates the axial slice location corresponding to the entry point. The MR scanner table is moved by manual input of the required table movement (Fig. 3.12a) which is calculated by

$$t_{\text{move}} = d_{\text{iso, laser}} + t_{\text{curr pos}} + \begin{cases} z_{\text{e}} \\ -z_{\text{e}} \end{cases} \quad \text{patient registered} \begin{cases} \text{head} \\ \text{feet} \end{cases} \quad \text{first,} \tag{3.2}$$

where $d_{\text{iso, laser}}$ is the distance between the laser light of the MR scanner and the isocenter of the magnet, $t_{\text{curr pos}}$ the current table position and z_{e} the z-coordinate of the planned entry point. The two cases need to be distinguished as the PCS flips depending on the patient registration.

2. Lateral Localization

Having moved the table by t_{move}, the landmark laser light is switched on and the next step is to measure the left-right (L-R) offset from the laser crosshair using an MR-compatible measuring tape. The L-R offset $d_{\text{l},r}$ is determined by calculating the distance along the patient's surface from the planned entry point to the point $\boldsymbol{p}_{\text{l}}$ marked on the patient's skin by the laser crosshair (Fig. 3.12b). Figure 3.13 illustrates the image processing pipeline.

(A) Segmentation of Object from Background

Based on the 3-D coordinates of the entry point, the axial MPR $I_{\text{a}}(u, v)$ in which the entry point lies is calculated. The next step is to segment the object, e.g. patient abdomen, from the background. The background is characterized as an area of low

(a) Segmentation of object from background

(b) Detection of object contour

(c) Calculation of L-R offset along contour

Figure 3.13*: Image processing pipeline for calculating the L-R offset (yellow line) along the patient's surface between the entry point* $\boldsymbol{p}_e$*(green point in (c)) and the point* $\boldsymbol{p}_l$ *marked on the patient's skin by the laser crosshair (blue point in (c)).*

signal, i.e. air, corrupted by some noise. The algorithm described in the following sections was designed under the assumption that the planning MR images do not suffer from bias fields, i.e. non-anatomic intensity variations of the same tissue over the image. The planning dataset is usually acquired in axial scan orientation using surface body and spin coils with prescan normalize selected, i.e. a homogeneity correction using coil sensitivity maps is applied [Nara 88].

The Otsu method [Otsu 79] is one of the most referenced thresholding methods. However, it requires a similar number of pixels in the background and object class [Sezg 04] which usually does not hold for MRI planning datasets used for percutaneous needle interventions (Fig. 3.14). Thus, the minimum error thresholding method proposed by Kittler [Kitt 86] was applied. Background and subject are modeled by two overlapping normal distributions with grey values g in the range $[0, 4095]$. The idea is to find a threshold T_{opt} for which the amount of overlap between the two distributions, and thus the number of misclassified pixels, is minimized. The histogram $h(g)$ can be viewed as an estimate of the probability density function [Kitt 86]

$$h(g) = \sum_{i=1}^{2} P_i(T)\; h(g|i,T) = \sum_{i=1}^{2} P_i(T)\; \frac{1}{\sqrt{2\pi}\sigma_i(T)} \exp \frac{-(g-\mu_i(T))^2}{2\sigma_i(T)^2}, \tag{3.3}$$

where $\mu_i(T)$ the mean value, and $\sigma_i(T)$ the standard deviation for threshold T, and $P_i(T)$ is the a priori probability given by

$$P_i(T) = \sum_{g=a}^{b} h(g), \tag{3.4}$$

where

$$a = \begin{cases} 0, & i = 1 \\ T+1, & i = 2 \end{cases} \text{ and } b = \begin{cases} T, & i = 1 \\ 4095, & i = 2 \end{cases}. \tag{3.5}$$

The probability of correctly assigning gray level g to either background or subject is given by

$$e(g,T) = h(g|i,T)P_i(T), \tag{3.6}$$

where $i = 1$ for $g \leq T$ and $i = 2$ for $g > T$. Since $h(g)$ is independent of both i and T, $e(g, T)$ can be maximized by minimizing

$$\epsilon(g, T) = \left[\frac{g - \mu_i(T)}{\sigma_i(T)}\right]^2 + 2\log\sigma(T) - 2\log P_i(T). \tag{3.7}$$

Thus, the overall performance is given by

$$J(T) = \sum_g h(g) \cdot \epsilon(g, T). \tag{3.8}$$

The minimum error threshold T_{opt} is thus given by $T_{\text{opt}} = \min_T J(T)$ which can be computed in an iterative fashion as described in [Kitt 86]. The binary image $B(u, v)$ is then calculated by

$$B(u, v) = \begin{cases} 0, & I_{\text{a}}(u, v) < T_{\text{opt}} \\ 1, & otherwise. \end{cases} \tag{3.9}$$

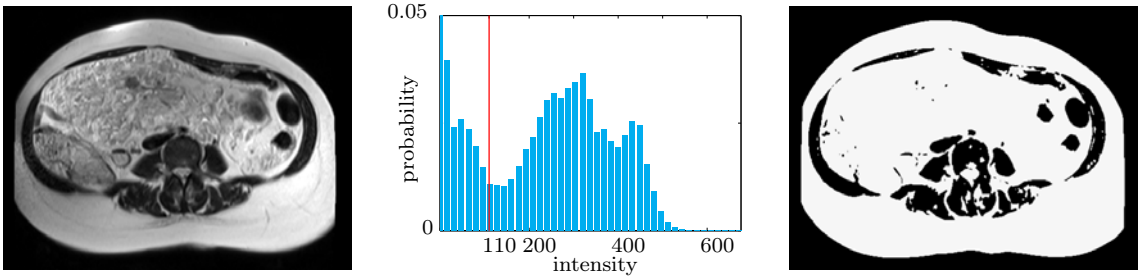

(a) Original image (b) Normalized histogram (c) Segmentation result

Figure 3.14: *Example for applying Kittler's method to the segmentation of a planning dataset. (a) Axial image plane from the planning dataset used for trajectory planning for sclerotherapy. (b) Normalized histogram with intensity values from 0 to 667, the optimal threshold was calculated to be 110. (c) Resulting binary image which is used as an input for the contour detection step.*

(B) Detection of Object Contour.

Having segmented the object from the background, the object's contour is determined by first removing the noise from the binary image. For each pixel it is checked if at least $n \leq \theta$, where θ is the defined threshold, of its 8-connected pixels are part of the object. If not the pixel is identified as noise and assigned to the background class. The object's contour is then identified by walking from the image border towards the center as described in Algorithm 3.1 and illustrated in Figure 3.15.

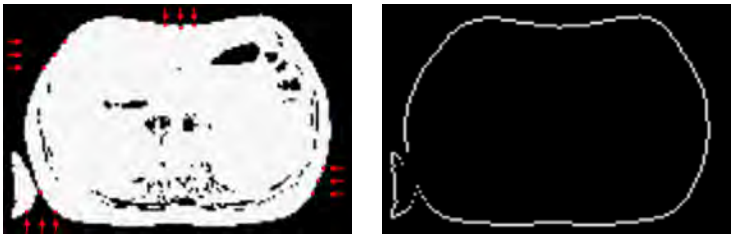

(a) Identification of object contour (b) Segmented object contour

Figure 3.15: *The object contour is identified by walking from the image border towards the center and only keeping the first detected object pixel.*

(C) Calculation of Left-Right (L-R) Offset Along Contour

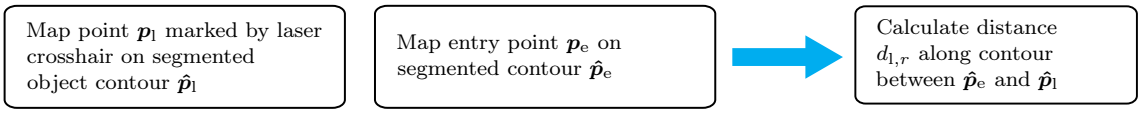

Figure 3.16: *Steps for calculating the L-R offset between the defined entry point $\boldsymbol{p}_e$ and the point $\boldsymbol{p}_l$ marked by the laser crosshair on patient's body.*

Calculating the lateral offset $d_{\mathrm{l},r}$ along the object's contour can be broken down in three main steps as illustrated in Figure 3.16. The first step is to map $\boldsymbol{p}_\mathrm{l} = (x_\mathrm{l}, y_\mathrm{l}, z_\mathrm{l})$ onto the corresponding point $\hat{\boldsymbol{p}}_\mathrm{l} = (u_\mathrm{l}, v_\mathrm{l})$ on the segmented object contour. $\boldsymbol{p}_\mathrm{l}$ is the point marked by the laser crosshair on patient's skin when the table is moved by the calculated superior-inferior distance (Fig. 3.11b). The column index u_l corresponding to x_l can be found by mapping $(0, 0, z_\mathrm{e})$ to image indices $(u_\mathrm{l}, 0)$. The first contour point in this column then defines the row index v_l. The next step is to ensure the entry point $\hat{\boldsymbol{p}}_\mathrm{e}$ is on the segmented contour. This is necessary as the user in the planning step might have placed the entry point slightly off from the object's contour. The entry point is set to the point $\hat{\boldsymbol{p}}_\mathrm{c}$ on the contour with the smallest Euclidean distance to $\hat{\boldsymbol{p}}_\mathrm{e}$. Finally, the L-R offset $d_{\mathrm{l},r}$ is determined by calculating the distance between $\hat{\boldsymbol{p}}_\mathrm{e}$ and $\hat{\boldsymbol{p}}_\mathrm{l}$ along the contour. In each step the closest neighbor to the current point on the contour $\hat{\boldsymbol{p}}_\mathrm{c}$ with the smallest distance to the point marked by the landmark laser $\hat{\boldsymbol{p}}_\mathrm{l}$ is selected. This approach is robust to holes in the contour. Further details on calculation of the $d_{\mathrm{l},r}$ are given in Algorithm 3.2.

Algorithm 3.1: Detection of object contour

Input: $B(u,v)$ with $u \in [0, M[$ and $v \in [0, N[$ `// binary image`
M `// number of columns`
N `// number of rows`
θ `// threshold for noise removal`
Output: $E(u,v)$ `// edge image`
begin
`// noise removal from binary image`
for $u \leftarrow 1$ **to** $M-2$ **do**
for $v \leftarrow 1$ **to** $N-2$ **do**
$s \leftarrow \sum_{i=u-1}^{u+1} \sum_{j=v-1}^{v+1} B(i,j)$
if $s < \theta$ **then**
$B(u,v) = 0$
end
end
end
`// search for closest edge points from top of image`
for $u \leftarrow 0$ **to** $M-1$ **do**
$v \leftarrow 0$
while $B(u,v) \neq 1$ *and* $v < N-1$ **do** $v \leftarrow v+1$
$E(u,v) = 1$
end
`// search for closest edge points from bottom of image`
for $u \leftarrow 0$ **to** $M-1$ **do**
$v \leftarrow N-1$
while $B(u,v) \neq 1$ *and* $v > 0$ **do** $v \leftarrow v-1$
$E(u,v) = 1$
end
`// search for closest edge points from left side of image`
for $v \leftarrow 0$ **to** $N-1$ **do**
$u \leftarrow 0$
while $B(u,v) \neq 1$ *and* $u < M-1$ **do** $u \leftarrow u+1$
$E(u,v) = 1$
end
`// search for closest edge points from right side of image`
for $v \leftarrow 0$ **to** $N-1$ **do**
$u \leftarrow M-1$
while $B(u,v) \neq 1$ *and* $u > 0$ **do** $u \leftarrow u-1$
$E(u,v) = 1$
end
end

Algorithm 3.2: Calculation of L-R offset

Input: $E(u, v)$ // edge image
$C = \{(u, v)|E(u, v) == 1\}$ // set of contour pixels
$\hat{\boldsymbol{p}}_{\mathrm{e}} = (u_{\mathrm{e}}, v_{\mathrm{e}})^{\mathrm{T}}$ // entry point pixel location
$\boldsymbol{p}_{\mathrm{e}} = (x_{\mathrm{e}}, y_{\mathrm{e}}, z_{\mathrm{e}})^{\mathrm{T}}$ // 3-D coordinates of entry point
$\boldsymbol{p}_{\mathrm{l}} = (x_{\mathrm{l}}, y_{\mathrm{l}}, z_{\mathrm{l}})$ // 3-D coordinates of point marked on patient's skin by the laser crosshairs
T_{plane} // matrix defining plane in which $\boldsymbol{p}_{\mathrm{e}}$ lies, see Eq. (3.1)
Output: $d_{\mathrm{l},r}$ // L-R offset
begin
  // map $\boldsymbol{p}_{\mathrm{l}}$ onto contour point $\hat{\boldsymbol{p}}_{\mathrm{l}} = (u_{\mathrm{l}}, v_{\mathrm{l}})^{\mathrm{T}}$
  $(u_{\mathrm{l}}, 0, w_{\mathrm{l}}, 1)^{\mathrm{T}} = {M_{plane}}^{-1} \cdot (0, 0, z_{\mathrm{e}}, 1)^{\mathrm{T}}$ and
  $v_{\mathrm{l}} = \mathrm{argmin}_v \{E(u_{\mathrm{l}}, v) \,|\, E(u_{\mathrm{l}}, v) == 1\}$
  // make sure the entry point is on segmented contour
  if $\hat{\boldsymbol{p}}_e \notin C$ **then**
    $\hat{\boldsymbol{p}}_{\mathrm{e}} = \mathrm{argmin}_{u,v} \{\|\hat{\boldsymbol{p}}_{\mathrm{e}} - \hat{\boldsymbol{p}}_{\mathrm{c}}\|_2 \,|\, \hat{\boldsymbol{p}}_{\mathrm{c}} \in C\}$
  end
  // calculate $d_{\mathrm{l},r}$ along segmented contour
  $\hat{\boldsymbol{p}}_{\mathrm{c}} = \hat{\boldsymbol{p}}_{\mathrm{e}}$
  $d_{\mathrm{l},r} \leftarrow 0$
  while $\hat{x}_c \neq u_l$ and $\hat{y}_c \neq v_l$ **do**
    // find next point $\hat{\boldsymbol{p}} = (u, v)^{\mathrm{T}}$ along contour
    $(u, v) = \mathrm{argmin}_{u,v} \{\|\hat{\boldsymbol{p}}_{\mathrm{c}} - \hat{\boldsymbol{p}}\|_2$ and $\|\hat{\boldsymbol{p}}_{\mathrm{l}} - \hat{\boldsymbol{p}}\|_2 \,|\, \hat{\boldsymbol{p}} \in C\}$
    // map $\hat{\boldsymbol{p}}_{\mathrm{c}}$ and $\hat{\boldsymbol{p}}$ to world coordinates $\boldsymbol{p}_{\mathrm{c}}$ and $\boldsymbol{p}$ and add their distance to the L-R offset
    $d_{\mathrm{l},r} = d_{\mathrm{l},r} + \|\boldsymbol{p}_{\mathrm{c}} - \boldsymbol{p}\|_2$
    $\hat{\boldsymbol{p}}_{\mathrm{c}} = \hat{\boldsymbol{p}}$
  end
end

3.2.3 Targeting

After entry point localization, the needle is partially inserted and the patient table is returned to the isocenter of the magnet. Continuous real-time imaging (2-5 fps) is used during needle advancement. Once triggered by the user, three MR slices are automatically aligned to the planned path $\boldsymbol{t}_{\mathrm{p}} = (\boldsymbol{p}_{\mathrm{t}} - \boldsymbol{p}_{\mathrm{e}})$ - two along the path and one orthogonal to it at the target. As a general guideline, these slices are oriented with preference to the standard axial, coronal, and sagittal planes (Sec. 3.2.4). This slice layout was chosen as the overlapping image planes cause slice overlap artifacts (Sec. 2.4.3) which can be exploited for needle guidance. As illustrated in Figure 3.17, the resulting saturation bands correspond to the planned trajectory with the target location at the intersection of these bands. The user can follow those saturation bands during needle advancement and knows the target is reached as soon as a cross-sectional needle artifact appears in the orthogonal target slice.

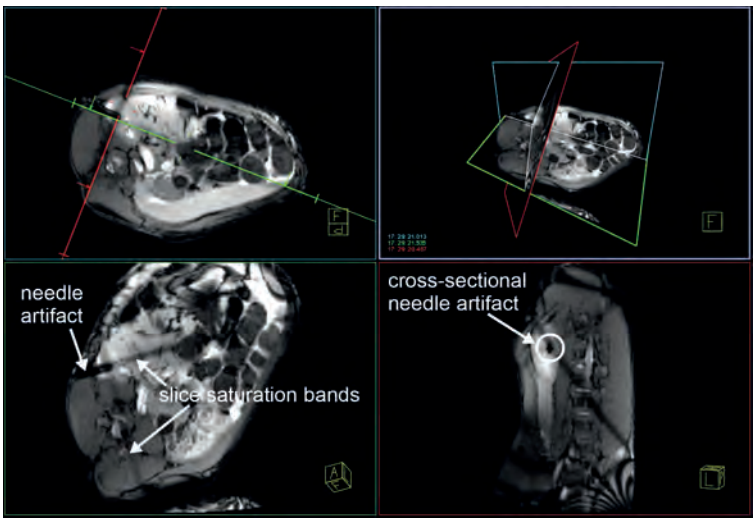

Figure 3.17*: Needle placement under real-time MR imaging guided by the slice saturation bands. The image planes are automatically aligned. The cross-sectional needle artifact in the plane perpendicular to the planned path at the target location indicates successful needle placement.*

3.2.4 Automatic Slice Alignment

Manual slice alignment can be very time-consuming and challenging in particular for double-oblique paths. Thus, the goal was to simplify this step by developing an automatic slice alignment algorithm which aligns the slices in an intuitive and reproducible manner along the planned path. The algorithm presented in the following pages is used for both MPR alignment for trajectory review during planning and initial scan plane alignment during real-time MR-guided targeting. In both workflow steps, three slices are used with two slices along the planned path orthogonal to each other and the third slice orthogonal to the trajectory at the planned target location. To allow for slice orientations the user is familiar with, the slices are oriented so that they are most closely aligned to the standard axial, coronal, and sagittal planes which span the patient coordinate system. These conventional image orientations are given in Table 3.1 and illustrated in Figure 3.18.

Table 3.1: *Conventional image orientations and the corresponding directions of row, column and normal vectors.*

	Row	Column	Normal
axial and axial-like oblique	patient's left $\boldsymbol{r}_{\mathrm{a}} = (1,0,0)^{\mathrm{T}}$	anterior $\boldsymbol{c}_{\mathrm{a}} = (0,1,0)^{\mathrm{T}}$	head $\boldsymbol{n}_{\mathrm{a}} = (0,0,1)^{\mathrm{T}}$
coronal and coronal-like oblique	patient's left $\boldsymbol{r}_{\mathrm{c}} = (1,0,0)^{\mathrm{T}}$	feet $\boldsymbol{c}_{\mathrm{c}} = (0,0,-1)^{\mathrm{T}}$	anterior $\boldsymbol{n}_{\mathrm{c}} = (0,1,0)^{\mathrm{T}}$
sagittal and sagittal-like oblique	posterior $\boldsymbol{r}_{\mathrm{s}} = (0,1,0)^{\mathrm{T}}$	head $\boldsymbol{c}_{\mathrm{s}} = (0,0,-1)^{\mathrm{T}}$	patient's left $\boldsymbol{n}_{\mathrm{s}} = (-1,0,0)^{\mathrm{T}}$

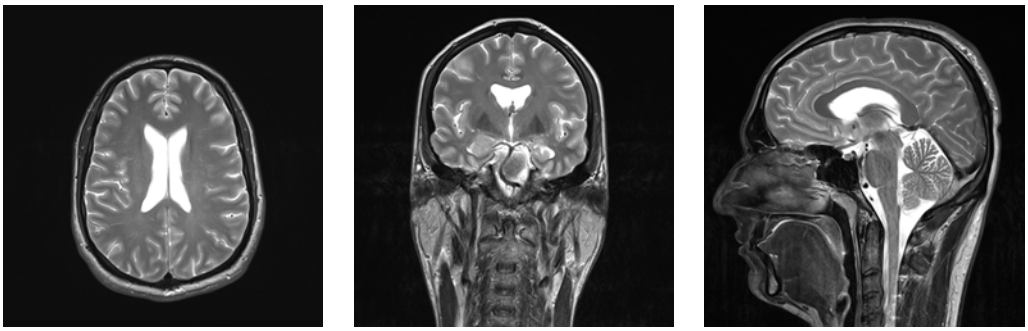

(a) Axial (b) Coronal (c) Sagittal

Figure 3.18*: Conventional image orientation on the example of T2-weighted TSE brain images acquired at a 3 T MR scanner (Siemens MAGNETOM Verio).*

The developed automatic slice alignment algorithm can be broken into the following steps. Details are given in Algorithm 3.3

1. Determine how close each standard plane is to the planned path. The two closest ones are used for the two slices along the planned path, the third one is used as the orthogonal one.

2. Span the first slice along the planned path.

3. Ensure default slice orientation so that its row, column, and normal vectors point in the same direction as those of the corresponding standard axial, coronal, or sagittal plane. The conventional orientations are given in Table 3.1.

4. In order to minimize wrap artifacts for a given field of view, the center of the slice is translated so that the normal through its center coincides with the center of the volume dataset.

5. Span the second slice along the planned path orthogonal to the first one. Apply steps 3 and 4 accordingly.

6. Align the third slice orthogonal to the first two ones intersecting at the target point. Set the center of the slice to the target point and apply step 3 accordingly.

Algorithm 3.3: Automatic slice alignment

Input: $\boldsymbol{p}_\mathrm{e} = (x_\mathrm{e}, y_\mathrm{e}, z_\mathrm{e})^\mathrm{T}$ `// 3-D coordinates of entry point`
$\boldsymbol{p}_\mathrm{t} = (x_\mathrm{t}, y_\mathrm{t}, z_\mathrm{t})^\mathrm{T}$ `// 3-D coordinates of target point`
$\boldsymbol{r}$, $\boldsymbol{c}$, and $\boldsymbol{n} \leftarrow$ vectors of conventional imaging planes (see Table 3.1)

Output: $\boldsymbol{r_s}$, $\boldsymbol{c_s}$, and $\boldsymbol{n_s} \in \mathbb{R}^3$ with $s \in \{1, 2, 3\}$ `// vectors spanning slices`

begin

`// 1. Find standard plane which is closest to planned path.`
$\boldsymbol{t}_\mathrm{p} = \boldsymbol{p}_\mathrm{t} - \boldsymbol{p}_\mathrm{e}$ `// planned trajectory`
$\boldsymbol{r_1} = \mathrm{argmax}_v \{{\boldsymbol{t}_\mathrm{p}}^\mathrm{T} \cdot \boldsymbol{v} | \boldsymbol{v} \in \{(1,0,0)^\mathrm{T}, (0,1,0)^\mathrm{T}, (0,0,1)^\mathrm{T}\}\}$

`// 2. Span first slice.`
$\boldsymbol{n} \leftarrow$ normal of closest conventional plane
$\boldsymbol{r_1} = \boldsymbol{t}_\mathrm{p}$ and $\boldsymbol{c_1} = \boldsymbol{n} \times \boldsymbol{t}_\mathrm{p}$

`// 3. Ensure default slice orientation.`
$i \leftarrow$ number of slice which is aligned, i.e. $i \in 1, 2, 3$
for $\boldsymbol{v_s} \in \{\boldsymbol{r_s}, \boldsymbol{c_s}, \boldsymbol{n_s}\}$ *and* $\boldsymbol{v} \in \{\boldsymbol{r}, \boldsymbol{c}, \boldsymbol{n}\}$ **do**
  if ${\boldsymbol{v_s}}^T \cdot \boldsymbol{v} < 0$ **then**
    $\boldsymbol{v_s} = -\boldsymbol{v_s}$
  end
end

`// 4. Set center of slice.`
$\boldsymbol{z_s} \in \mathbb{R}^3 \leftarrow$ center of slice i
$\boldsymbol{z}_\mathrm{new} \in \mathbb{R}^3 \leftarrow$ new center of slice i
$\boldsymbol{z}_\mathrm{v} \in \mathbb{R}^3 \leftarrow$ center of volume dataset
$\boldsymbol{z}_\mathrm{new} = \boldsymbol{z_s} + \mu \boldsymbol{r_s} + \xi \boldsymbol{c_s}$, where $\mu = (\boldsymbol{z}_\mathrm{v} - \boldsymbol{z})^\mathrm{T} \cdot \boldsymbol{r_s}$ and $\xi = (\boldsymbol{z}_\mathrm{v} - \boldsymbol{g})^\mathrm{T} \cdot \boldsymbol{c_s}$

`// 5. Span second slice.`
$\boldsymbol{r_2} = \boldsymbol{t_p}$ and $\boldsymbol{c_2} = \boldsymbol{c_1} \times \boldsymbol{t_p}$
Apply steps 3 and 4 accordingly.

`// 6. Span third slice.`
$\boldsymbol{r_3} = \boldsymbol{r_1} \times \boldsymbol{c_1}$ and $\boldsymbol{c_3} = \boldsymbol{c_1} \times \boldsymbol{c_2}$
$\boldsymbol{z_3} \leftarrow \boldsymbol{p}_\mathrm{t}$ `// set center of third slice to target point`
Apply step 3 accordingly.

end

3.3 Automatic Entry Point Adaptation

The automatic slice alignment algorithm described in Section 3.2.4 uses the planned entry point for scan plane alignment and does not account for deviations from that plan. As the needle is usually first inserted a few millimeters into the subcutaneous tissue, one can first detect this actual device entry point and then automatically align the slices along the updated trajectory information. Figure 3.19 illustrates the proposed algorithm. To detect the needle while it is inserted under continuous MR imaging into the subcutaneous tissue, three scan planes are aligned orthogonal to the planned trajectory at the planned entry point to allow for detection of the actual device entry point. The needle causes a cross-sectional artifact (Fig. 2.12) in the images. The algorithm is performed independently for each of the three imaging slices and the winner from the detected candidates is selected based on the distance to the planned path. The methods presented within this section have been published in [Roth 11a, Stre 09].

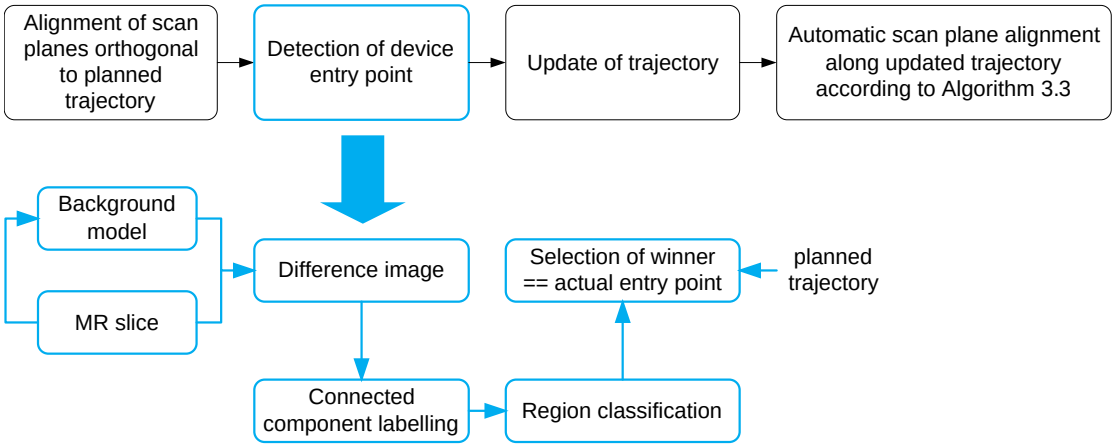

Figure 3.19: *Block diagram of entry point adaptation algorithm and its integration into the automatic slice alignment method. The entry point detection is performed independently for each slice.*

3.3.1 Algorithm

The first step of the algorithm is to classify the pixels of the incoming MR image slice as either foreground, i.e. potential needle artifact, or background by means of background subtraction [Herr 09]. The goal is to extract pixels in the incoming MR image frame exhibiting a significantly lower image intensity compared to the background. To allow for adaptivity of the background model to small intensity changes, the background G is updated by exponential running average [Wren 97]. Thus, more recent real-time images are weighted stronger and older image data is discounted in an exponential manner. G is initially set to the first image I_0 and updated for each pixel (u, v) by

$$G_{t+1}(u, v) = (1 - \alpha)G_t(u, v) + \alpha I_t(u, v), \tag{3.10}$$

where the learning rate $\alpha \in [0, 1]$ specifies how fast new information supplants old observations.

The binary difference image B_t is then computed by

$$B_t(u,v) = \begin{cases} 1, & \text{if } G_t(u,v) - I_t(u,v) \geq \theta, \\ 0, & \text{otherwise.} \end{cases} \tag{3.11}$$

The threshold θ and α were heuristically set to 50 and 0.25.

In the next step, connected component labeling [Lumi 83] is used to extract candidate regions $\mathcal{R}$ from the binary difference image B_t. The region is classified as needle artifact or discarded based on circularity of the region and proximity to the target path. Circularity can be computed by

$$K(\mathcal{R}) = 4\pi \frac{A(\mathcal{R})}{Pe^2(\mathcal{R})}, \tag{3.12}$$

where $A(\mathcal{R}) = \sum_{(x,y)\in\mathcal{R}} 1$ is the area of the region and $Pe(\mathcal{R})$ its perimeter [Yang 94]. For a circle K is equal to 1, for all other shapes it is between 0 and 1. The perimeter of a region can be estimated by

$$Pe(\mathcal{R}) = n_\mathrm{e} + \sqrt{2} n_\mathrm{o}, \tag{3.13}$$

where n_o is the number of odd and n_e the number of even Freeman chain codes [Free 61].

The proximity of a region to the planned path $d_{\boldsymbol{p}_\mathrm{c},\boldsymbol{t}_\mathrm{p}}$ is given by the distance between the region's centroid $\boldsymbol{p}_\mathrm{c}$ and its orthogonal projection $\boldsymbol{\Gamma}$ onto the planned path

$$d_{\boldsymbol{p}_\mathrm{c},\boldsymbol{t}_\mathrm{p}} = \left\| \boldsymbol{\Gamma} - \boldsymbol{p}_\mathrm{c} \right\|_2 . \tag{3.14}$$

The centroid $\hat{\boldsymbol{p}}_\mathrm{c} = (\overline{u}, \overline{v})^\mathrm{T} \in \mathbb{R}^2$ of a region is the arithmetic mean of the coordinates in x and y directions with

$$\overline{u} = \frac{1}{A(\mathcal{R})} \sum_{(u,v)\in\mathcal{R}} u \quad \text{and} \quad \overline{v} = \frac{1}{A(\mathcal{R})} \sum_{(u,v)\in\mathcal{R}} v. \tag{3.15}$$

The projection $\boldsymbol{\Gamma} \in \mathbb{R}^3$ of the region's centroid onto the planned path $\boldsymbol{t}_\mathrm{p}$ is given by

$$\boldsymbol{\Gamma} = \boldsymbol{p}_\mathrm{e} + \frac{(\boldsymbol{p}_\mathrm{c} - \boldsymbol{p}_\mathrm{e}) \cdot \boldsymbol{t}_\mathrm{p}}{\left\| \boldsymbol{t}_\mathrm{p} \right\|_2^2} \, \boldsymbol{t}_\mathrm{p}, \tag{3.16}$$

where $\boldsymbol{p}_\mathrm{c}$ are the 3-D coordinates (see Eq. 3.1) of $\hat{\boldsymbol{p}}_\mathrm{c}$.

3.3.2 Evaluation - Results of Phantom Experiments

In order to measure the accuracy of the proposed entry point detection algorithm, a fully MR-compatible, precisely machined phantom was designed from plexiglas (Fig. 3.20). It served as ground truth for needle position as the phantom coordinate system can be aligned with the image coordinate system by landmarking at the center of the clipped-in white board. Landmarking with the laser crosshair defines a position on the object that when moved into the magnet coincides with the center of the DICOM

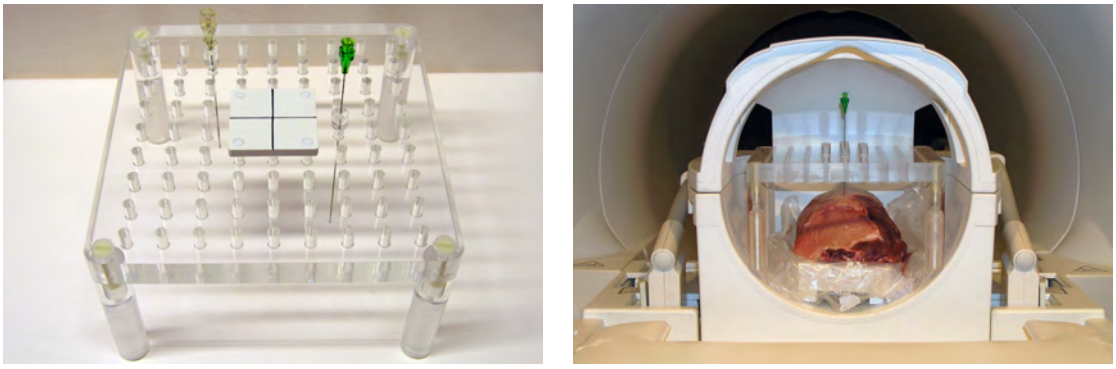

(a) (b)

Figure 3.20*: (a) Custom-built, fully MR-compatible phantom for validation of needle detection accuracy. The needle sleeves can be exchanged to exactly fit the used needle. Calibration is performed with the freely placeable white board by aligning it with the isocenter of the magnet, and thus the DICOM coordinate system, using the built-in laser. (b) For the needle entry point detection experiment the phantom was placed on top of a pork sample inside the head coil on a MAGNETOM Avanto 1.5 T MR scanner.*

coordinate system (Sec. 3.2.2). To further enhance accuracy, the needle clips were designed to exactly fit the needles for precise positioning into the sample.

Two MR-compatible biopsy needles (COOK Medical and E-Z-EM, Inc) of size 18 G (Gauge) and 21 G were used. The effect of needle size and composition on artifact size is illustrated in Figure 3.21. Using the phantom, a pork sample was biopsied 11 times with each needle under continuous imaging at a sampling rate of 5 frames per second using a balanced SSFP sequence. The needle artifact was successfully detected in all 66 slices. The mean detection accuracy was 1.3 mm ($\sigma = 0.6$ mm) for the 18 G needle and 1.6 mm ($\sigma = 0.9$ mm) for the 21 G needle. This accuracy is sufficient for online entry point adaptation as the error is smaller than the standard slice thickness (5 - 8 mm) used.

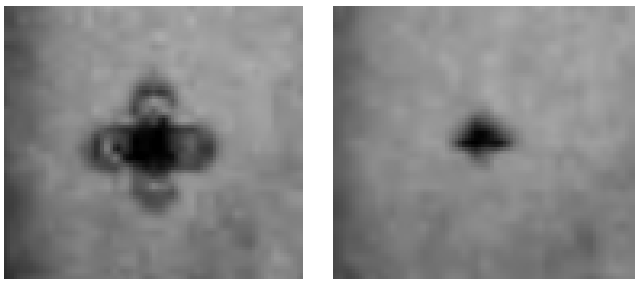

(a) 18G, Cook Medical (b) 21G, E-Z-EM, Inc

Figure 3.21*: Artifacts created by the needles are strongly dependent on needle size and composition. Sequence parameters were the same for both needles which were placed perpendicular to the main magnetic field (Fig. 3.20) and imaged orthogonal to the needle trajectory.*

3.4 Real-time Needle Artifact Segmentation

Having automatically aligned the slices along the planned trajectory taking into consideration the adapted entry point, the next step is to advance the needle along the slice saturation bands. The clinical prototype implemented within this thesis supports manual adjustment of the image planes during scanning if the needle deviates from the planned trajectory. In the following sections, a method is presented which allows for automatic segmentation of the needle artifact during targeting as illustrated in Figure 3.22.

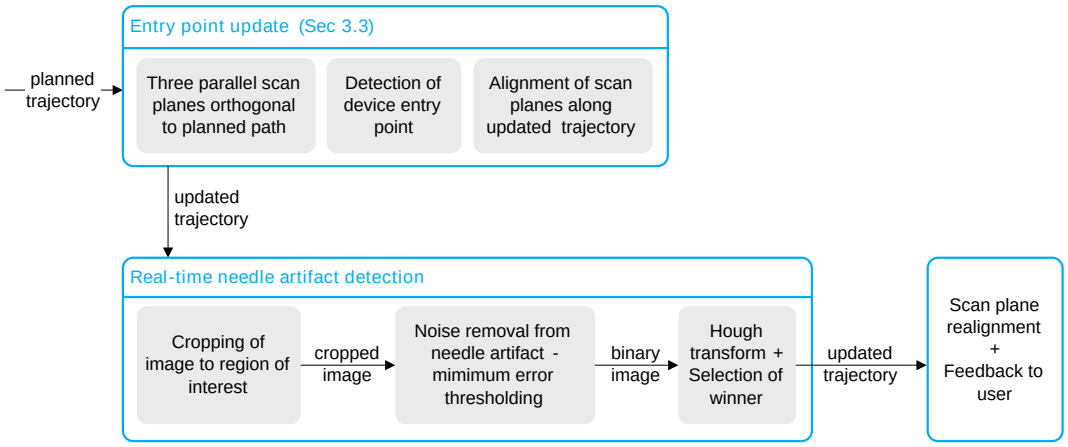

Figure 3.22: *Proposed algorithm for real-time needle artifact segmentation.*

The information about the current needle position can be used for automatic slice realignment during needle advancement and for providing feedback to the user about the deviation from the planned trajectory.

3.4.1 Algorithm

The proposed algorithm by intention does not employ any background subtraction as the goal was to ensure the method also works when no background image is available, e.g. when the user has moved the image plane. Instead, as the needle appears as a linear artifact in the image planes along the trajectory, the proposed algorithm employs the Hough Transform [Houg 62], a commonly used technique for straight line detection in binary images [Duda 72]. Before the Hough transform is applied, the image is preprocessed by

1. Cropping the image to a region of interest (ROI) around the planned trajectory.

2. Applying Kittler's method to segment the patient's body from the needle artifact and background.

Parts of this algorithm result from joint work with Jessica Magaraggia during her master's thesis [Maga 11].

Calculation of region of interest

To save computational time and reduce the likelihood for detecting false straight lines, e.g. subcutaneous fat tissue, the search region for real-time needle segmentation is restricted to an area around the planned path as illustrated in Figure 3.23. The planned trajectory $\boldsymbol{t}_\mathrm{p}$ is orthogonally projected onto the image plane and the entry point is then moved along the direction of the path to $\boldsymbol{p}_\mathrm{es}$ by

$$\boldsymbol{p}_\mathrm{es} = \boldsymbol{p}_\mathrm{e} - 0.05 \cdot \boldsymbol{t}_\mathrm{p} \tag{3.17}$$

This is done in order to avoid cutting the upper part of the needle artifact.

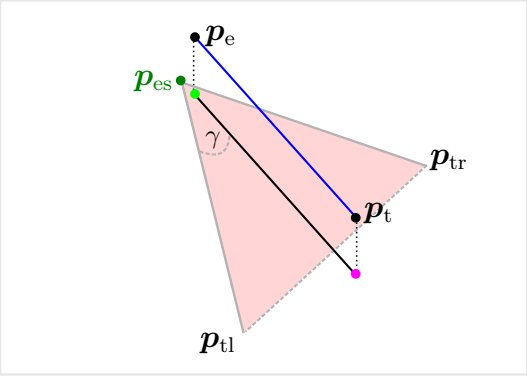

Figure 3.23: *Projection of the planned entry point $\boldsymbol{p}_e$ and target point $\boldsymbol{p}_t$ onto the image plane and definition of sector in which needle artifact is searched.*

The left $\boldsymbol{p}_\mathrm{tl}$ and right $\boldsymbol{p}_\mathrm{tr}$ point restricting the sector can be found by rotating the target point $\boldsymbol{p}_\mathrm{t}$ by the angle $-\gamma/\gamma$ about the line going through $\boldsymbol{p}_\mathrm{es}$ and pointing into the direction of the image plane normal $\boldsymbol{p}_\mathrm{n} = (x_\mathrm{n}, y_\mathrm{n}, z_\mathrm{n})^\mathrm{T}$. The rotation matrix $R(\gamma)$ is given by

$$R(\gamma) = T_{\boldsymbol{p}_\mathrm{t}}^{-1} \cdot T_\mathrm{xz}^{-1} \cdot T_\mathrm{z}^{-1} \cdot R_\mathrm{z} \cdot T_\mathrm{z} \cdot T_\mathrm{xz} \cdot T_{\boldsymbol{p}_\mathrm{t}}, \tag{3.18}$$

where $T_{\boldsymbol{p}_\mathrm{t}}$ is the transformation matrix moving $\boldsymbol{p}_\mathrm{t}$ to the origin, T_xz the transformation matrix rotating $\boldsymbol{p}_\mathrm{t}$ about the z-axis to the xz-plane, T_z the transformation matrix rotating $\boldsymbol{p}_\mathrm{t}$ in the xz-plane to the z-axis, and R_z the rotation matrix rotating $\boldsymbol{p}_\mathrm{t}$ by γ around the z-axis. Equations 3.19 and 3.20 give the matrices, the expanded 3-D rotation matrix formula for Equation 3.18 can be found in [Murr].

$$T_{\boldsymbol{p}_\mathrm{t}} = \begin{pmatrix} 1 & 0 & 0 & -x_\mathrm{t} \\ 0 & 1 & 0 & -y_\mathrm{t} \\ 0 & 0 & 0 & -z_\mathrm{t} \\ 0 & 0 & 0 & 1 \end{pmatrix} T_\mathrm{xz} = \begin{pmatrix} \frac{x_n}{\sqrt{x_\mathrm{n}^2+y_\mathrm{n}^2}} & \frac{y_n}{\sqrt{x_\mathrm{n}^2+y_\mathrm{n}^2}} & 0 & 0 \\ \frac{-y_n}{\sqrt{x_\mathrm{n}^2+y_\mathrm{n}^2}} & \frac{x_n}{\sqrt{x_\mathrm{n}^2+y_\mathrm{n}^2}} & 0 & 0 \\ 0 & 0 & 1 & 0 \\ 0 & 0 & 0 & 1 \end{pmatrix} \tag{3.19}$$

$$T_\mathrm{z} = \begin{pmatrix} \frac{z_\mathrm{n}}{\sqrt{x_\mathrm{n}^2+y_\mathrm{n}^2+z_\mathrm{n}^2}} & 0 & -\frac{\sqrt{x_\mathrm{n}^2+y_\mathrm{n}^2}}{\sqrt{x_\mathrm{n}^2+y_\mathrm{n}^2+z_\mathrm{n}^2}} & 0 \\ 0 & 1 & 0 & 0 \\ \frac{\sqrt{x_\mathrm{n}^2+y_\mathrm{n}^2}}{\sqrt{x_\mathrm{n}^2+y_\mathrm{n}^2+z_\mathrm{n}^2}} & 0 & \frac{z_\mathrm{n}}{\sqrt{x_\mathrm{n}^2+y_\mathrm{n}^2+z_\mathrm{n}^2}} & 0 \\ 0 & 0 & 0 & 1 \end{pmatrix} R_\mathrm{z} = \begin{pmatrix} \cos\gamma & -\sin\gamma & 0 & 0 \\ \sin\gamma & \cos\gamma & 0 & 0 \\ 0 & 0 & 1 & 0 \\ 0 & 90 & 0 & 1 \end{pmatrix} \tag{3.20}$$

Having calculated $\boldsymbol{p}_{\text{tl}}$ and $\boldsymbol{p}_{\text{tr}}$, one needs to determine if a point is inside the triangle. This can be done with the help of barycentric coordinates which allow to express the coordinates of a point $\hat{\boldsymbol{p}} = (u, v)$ in terms of the vertices of a triangle

$$\hat{\boldsymbol{p}} = \hat{\boldsymbol{p}}_{\text{tl}} + \mu(\hat{\boldsymbol{p}}_{\text{tr}} - \hat{\boldsymbol{p}}_{\text{tl}}) + \nu(\hat{\boldsymbol{p}}_{\text{es}} - \hat{\boldsymbol{p}}_{\text{tl}}), \tag{3.21}$$

where

$$\mu = \frac{\begin{vmatrix} u_{\text{tl}} - u_{\text{es}} & u - u_{\text{es}} \\ v_{\text{tl}} - v_{\text{es}} & v - v_{\text{es}} \end{vmatrix}}{\begin{vmatrix} u_{\text{tr}} - u_{\text{tl}} & u_{\text{es}} - u_{\text{tl}} \\ v_{\text{tr}} - v_{\text{tl}} & v_{\text{es}} - v_{\text{tl}} \end{vmatrix}} \quad \text{and} \quad \nu = 1 - \mu - \frac{\begin{vmatrix} u_{\text{tr}} - u_{\text{tl}} & u - u_{\text{tl}} \\ v_{\text{tl}} - v_{\text{tl}} & v - v_{\text{tl}} \end{vmatrix}}{\begin{vmatrix} u_{\text{tr}} - u_{\text{tl}} & u_{\text{es}} - u_{\text{tl}} \\ v_{\text{tr}} - v_{\text{tl}} & v_{\text{es}} - v_{\text{tl}} \end{vmatrix}}. \tag{3.22}$$

The derivation of Eq. 3.22 can be found in [Lava]. $\hat{\boldsymbol{p}}$ is inside the triangle if $\mu \geq 0$, $\nu \geq 0$, and $\mu + \nu < 1$.

Noise removal from needle artifact

The needle artifact is characterized as an area of low signal corrupted by noise. To reliably detect the needle artifact in the next step, the needle needs to be clearly separated from the patient body which is a classical object-background separation problem. As described in Section 3.2.2, Kittler's method is well suited for that purpose. Figure 3.24 shows an example image with a needle in place before and after applying this minimum-error threshold method.

(a) Original (b) Thresholded

Figure 3.24*: Example image from a kidney biopsy (a) before and (b) after applying the minimum-error threshold method.*

Calculation of Hough transform and selection of winner

Having removed the noise from the needle artifact, the next step is to identify the centerline of the needle artifact. This problem can be modeled by finding the longest straight line within the cropped image. The Hough transform is well suited for that purpose as it is based on a voting scheme which only requires a binary image as an input. The needle artifact is usually wider than one pixel, i.e. in theory it would be represented by two parallel lines in an edge image. However, detecting those two parallel lines in an edge image using the Hough transform [Jung 06] does not yield reliable results [Maga 11]. This is due to the fact that the needle artifact does not

show up as perfectly parallel edges in the real-time MR images but instead the edges tend to be frayed. Thus, it is proposed to calculate all potential needle centerlines using the Hough transform, to identify maxima in the Hough accumulator array and to then select the winner needle centerline from those candidates.

The underlying principle of the Hough transform is the duality between image space, (u, v), and parameter space, (m, b), where m is the slope and b the intercept of the line $v = um + b$. Detecting a straight line in a binary image can thus be modeled by finding the maximum in an accumulator array, $A(m, b)$, as collinear points increase the vote for a specific parameter set (m, b). However, for lines which are near vertical, both m and b are infinite. This can be solved by using the Hessian normal form of the equation of a line which writes as

$$\rho = u \cos\theta + v \sin\theta, \tag{3.23}$$

as proposed in [Duda 72]. ρ is the normal from the origin to the line and θ, $0° \leq \theta < 180°$, the angle of the line's normal with respect to the x-axis. To speed up computation time, the search space for the Hough transform is restricted to $\pm 30°$ around the planned trajectory.

Having calculated the accumulator array, maxima are identified and the winner needle centerline is detected based on the following two criteria:

1. The number of votes in $A(\theta, \rho)$. The higher the votes the longer the line.

2. Its position within the needle artifact. As illustrated in Figure 3.25, the optimal straight line l_{opt} should be positioned in the center of the needle artifact. It can be selected from all candidate lines l_c by

$$l_{opt} = \underset{l_c}{\operatorname{argmin}} \sum_{\hat{p} \in l_c} |\hat{p}_a - \hat{p}_b|, \tag{3.24}$$

   where $\hat{p} \in l_c$ are all points on the line and $\hat{p}_a$ is the closest object point above $\hat{p}$ and $\hat{p}_b$ is the closest object point below $\hat{p}$.

The voting scheme employed by the Hough Transform allows to also detect broken lines which makes the method robust to imperfect background/ object separation.

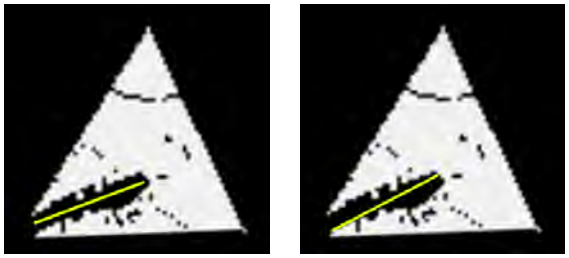

(a) Centered line (b) Longer but not centered line

Figure 3.25: *Selection of winner line (a) based on its position within the needle artifact. (b) shows the longest line within the ROI.*

3.4.2 Evaluation

The needle artifact centerline was segmented and compared with the automatically detected needle centerline in 169 *in-vivo* images from MR-guided abdominal biopsies. An example is given in Figure 3.26. The mean difference in ρ between detected and segmented needle centerline was 2.1 ± 1.5 mm, the median difference 1.8 mm. This is sufficient to accurately realign the 4 mm thick scan plane along the needle trajectory. A limitation of the study relates to the fact that the needle artifact centerline had to be manually segmented as no ground truth position data can be derived from the passive needles. For non-human data one can derive ground truth data by interchanging the metal needle with a glass needle as proposed in [Song 12].

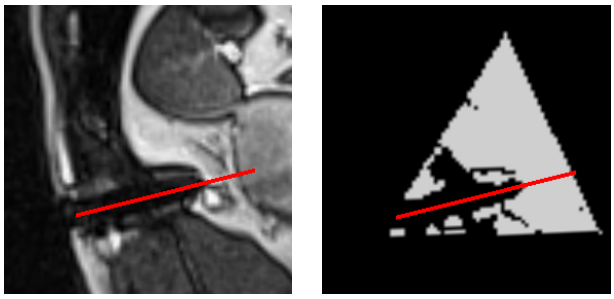

Figure 3.26*: Exemplary result of automatic needle artifact detection with the detected centerline overlaid in red.*

3.5 Summary

The presented simplification of workflow overcomes many of the potential barriers to percutaneous needle interventions in what is typically considered a "procedure-hostile" environment, without extra hardware, such as robots [Zang 11, Moch 08, Moch 10], tracking cameras [Ojal 02, Sequ 02, Buss 10], needle guides [Chri 07] or augmented reality overlay systems [Wack 06, Fisc 07a] that can disrupt and complicate the interventionalist's normal workflow and contribute to increased total intervention time [Moch 10].

For planning, the ability to prescribe multiple trajectories at one time supports a "plan once, scrub once" procedure strategy and allows the user to proceed from one needle placement to the next quickly without the need to break scrub for planning or to identify the next skin entry site. This has been reported as a limitation of other systems [Moch 10]. Multiplanar reformatting also allows for complex trajectory selection and when combined with automatic MPR plane alignment can enhance safety by providing advanced reviewing capabilities to ensure avoidance of critical structures. Furthermore, intra-procedure trajectory adjustments can be made without the need for needle repositioning.

Skin entry point localization is significantly improved by eliminating the multiple, time-consuming steps associated with the standard water-filled syringe and fingertip approaches [Beye 05]. Using only the MR system's laser and a tape measure, all skin entry sites can be accurately located before scrubbing the patient, and the interventionalist can move quickly from one site to the next without needing to re-identify entry sites and trajectories for each needle placement.

Automatic slice alignment overcomes one of the most significant challenges in a freehand MR-guided needle intervention [Stat 08b]. Because it is essential to continuously visualize the entire needle, the target and the surrounding structures, slice alignment typically requires significant intra-procedure communication [Fisc 11]. This can be confusing and time-consuming for both the interventionalist and MR technician, and is particularly challenging for complex trajectories [Stat 08a, Moch 10]. Unlike other studies which use only one [Stat 08b, Frit 08, Frit 09] or two alternating image planes [Fisc 11, Stre 10, Rick 10] during guidance, our strategy automatically prescribes three real-time image planes – two perpendicular planes along the needle path and a third orthogonal to them at the target location. Intuitive slice orientation is further improved by automatically aligning the slices as closely as possible to the principal patient axes. This orientation strategy gives the interventionalist the ability to detect deviations and correct for them. As the planes are acquired with 2-5 frames per second and instantly visualized, there is no need to switch between them using a foot pedal [Rick 10] or selecting a different mode [Silv 95].

In summary, the proposed methods presented hold promise to improve and simplify real-time MR-guided needle placement. Chapter 5 provides an overview of the clinical evaluation performed so far. Both targeting accuracy and time were validated *in-vivo* and *in-vitro*, taking into account trajectory obliquity, level of experience and organ motion.

MR Thermometry 4

In modern oncology, percutaneous thermal ablations are increasingly used as a regional treatment option to supplement systemic treatment strategies such as chemotherapy and immunotherapy [Solo 10]. They provide an attractive alternative to surgery for the treatment of focal malignancies in the liver, kidney, prostate, lung, and bone [Vogl 02, Ahme 11, Staf 12]. Percutaneous thermal ablations may be performed with a variety of energy sources, including radiofrequency, microwave, laser, and cryoablation. The goal of all thermal ablation procedures is to cause cell death of disease tissue while sparing surrounding healthy structures. Thus, real-time assessment of thermal damage is key to therapeutic efficiency and safety of such ablative procedures. Current techniques of monitoring thermal damage, like the placement of temperature probes, are inadequate. They generally use sparse sampling methods to measure the heating or impedance during the interventions. Magnetic resonance thermometry allows for real-time, non-invasive monitoring of spatial distribution and temporal evolution of temperature changes by exploiting changes in the physical properties of the hydrogen protons undergoing thermal manipulation.

The chapter begins by giving a short technical introduction into the energy sources used for thermal ablations (Sec. 4.1.1) and further motivates the use of MR image guidance (Sec. 4.1.2). Several temperature-dependent MR parameters can be exploited for MR thermometry. This work focuses on the PRF shift with details given in Section 4.1.3. Having provided the necessary background information, methods for improving the workflow and clinical usability of MR thermometry are introduced (Sec. 4.2). As accurate applicator placement is essential for the success of any percutaneous thermal ablation, a prototype was implemented which integrates the developed needle guidance algorithms with methods for enhanced MR thermometry visualization and treatment monitoring (Sec. 4.3). For the prototype to be used in a clinical setting, it had to be integrated into the MR scanner setup which is originally focused on diagnostic imaging (Sec. 4.3.2). Parts of this chapter are based on publications cited throughout the text.

4.1 Motivation

Most percutaneous thermal ablations are currently performed under CT or US guidance. However, MR imaging is a promising tool for guiding thermal ablations due to its high soft-tissue contrast, multi-planar imaging capabilities and sensitivity to thermal effects without ionizing radiation. In the following section, RF and laser ablation are briefly discussed as examples for heat-based thermal ablation devices. Focus

is put on their compatibility with MR. In the next sections, the necessity of spatial temperature measurement is motivated and the technical background on PRF shift-based MR thermometry is provided to the reader. Parts of this section are based on [Roth 08].

4.1.1 Thermal Ablation Procedures

Thermal ablations induce irreversible cellular damage by increasing or decreasing tissue temperatures sufficiently. There are two main approaches to thermal therapies, namely cryoablation (Sec. 5.3.1) and heat-based ablations working with focused ultrasound or electromagnetic (laser, microwave, RF) energy. In the following paragraph, RF ablation is described as it is the most well-studied and clinically relevant ablation source to date [Ahme 11]. Details on laser ablation are further provided as laser energy is fully MR-compatible, and laser fibers do not cause any MR image artifacts.

RF Ablation RF thermal ablation (RFA) works by transforming RF energy into heat, which is deposited into the target tissue through a non-insulated electrode tip connected to an RF generator providing power in the range of 60 to 250 W. A grounding pad is placed on the patient's skin. The current flow from the electrode tip to the pad leads to frictional heating in the tissue around the tip. Coagulation necrosis, causing irreversible tissue damage, occurs instantly at temperatures in the range of 60 to 100 °C. Lower temperatures in the range of 50 to 60 °C may induce coagulation in minutes, whereas temperatures below 50 °C do not reliably induce necrosis. Temperatures over 100 °C should be avoided as air bubbles from boiling tissue have an insulating effect on the deposition of heat energy into the surrounding cancerous tissue [Bela 07]. Using RF under MR image guidance is complicated by the fact that RF energy can cause severe artifacts in MR images. Thus, shielded cables are necessary and the RF generator needs to be placed outside the MR magnet room with the output signal filtered to attenuate RF interference artifacts around the MR frequency [Sero 08].

Laser Ablation Laser-induced thermal therapy (LITT) is based on local emission of electromagnetic radiation increasing tissue temperatures to lethal levels [Staf 10, Lee 14]. Laser energy can be delivered through thin and flexible fibers placed interstitially in the tumor. Thus, LITT is attractive for small ablation zones (1 - 2 cm diameter) where a high spatial precision is needed. The light wavelength defines the extent of tissue penetration with clinical lasers usually operating in the range of 600 - 1000 nm [Ahme 11]. The primary advantage of using laser energy is its inherent MR compatibility with the laser fibers causing no MR image artifacts.

4.1.2 Rationale for MR Thermometry

Regardless of which energy source is used, the common goal is selective tumor treatment that does not damage healthy structures. One approach to achieve this goal is to directly monitor ablation-induced tissue changes using imaging modalities such as US, CT, or MR. However, the extent of cell death might be underestimated as temperatures needed to induce structural changes are higher than temperatures needed

to cause cell death. Thus, it is desirable to continuously measure *in-vivo* the spatial and temporal temperature distribution during the procedure.

Several strategies exist for measuring tissue temperature *in-vivo*. One approach uses exposure length and power delivered by the treatment device to predict the actual tissue temperature. However, temperature prediction based on this information is difficult since tissue properties (absorption, blood perfusion and flow, etc.) vary largely, and hence modify local heat conduction and energy absorption [Senn 07]. This, in particular, holds for tumors close to large blood vessels which can act as a heat-sink [Than 08]. Thermocouples, thermistors, or fiber-optic temperature probes can accurately measure temperature at a single location. However, the prediction of the entire ablation zone based on this information is challenging as blood flow, effects of tissue heterogeneity, and physiological reactions have to be accounted for. Consequently, instead of based on a model derived from single-point temperature measurements, a non-invasive imaging technique that can map temperatures directly to spatial locations is required.

4.1.3 Principles of PRF-based Temperature Mapping

The tomographic nature of MR and the linear sensitivity of its ^1H phase signal to temperature make MR well-suited for non-invasive, *in-vivo* measurement of the spatial and temporal distribution of temperature changes. Further, changes in soft tissue contrast in magnitude images can reflect irreversible tissue necrosis, adding to the thermal information derived from temperature sensitive phase images.

Several temperature-dependent MR parameters such as the longitudinal relaxation time T_1 [Park 84], the molecular diffusion coefficient D [Le B 89], or the PRF shift [Ishi 95] can be exploited for the purpose of temperature mapping. The PRF shift method is currently the most widely used MR thermometry method at mid and high field (0.5 T and above) [Deni 05] due to the following advantages. First, the PRF shows a linear correlation with temperature over a wide range of temperatures from -15 °C to 100 °C [Hind 66]. Second, its temperature sensitivity coefficient α is almost constant and nearly independent of tissue type, except for tissue with high content of fat.

Temperature mapping using the PRF shift is based on the fact that the proton resonance frequency ω is dependent on the local magnetic field strength (Sec. 2.1.3). As illustrated in Figure 4.1, the electron around the hydrogen nucleus (proton) has a shielding effect so that the local magnetic field $\boldsymbol{B}$ experienced by the proton is slightly smaller than the external macroscopic field strength $\boldsymbol{B_0}$. The dependence of $\boldsymbol{B}$ on the nuclear shielding effect can be expressed by

$$\boldsymbol{B} = (1 - \sigma)\boldsymbol{B_0}, \tag{4.1}$$

where σ denotes the nuclear shielding constant which can be further described by

$$\sigma(T) = \sigma_0 + \sigma_T. \tag{4.2}$$

σ_0 is the temperature independent contribution, i.e. resulting from $\boldsymbol{B_0}$ field inhomogeneities, and σ_T the temperature dependent contribution which is influenced by hydrogen bonds between water molecules which pull electrons away from the protons

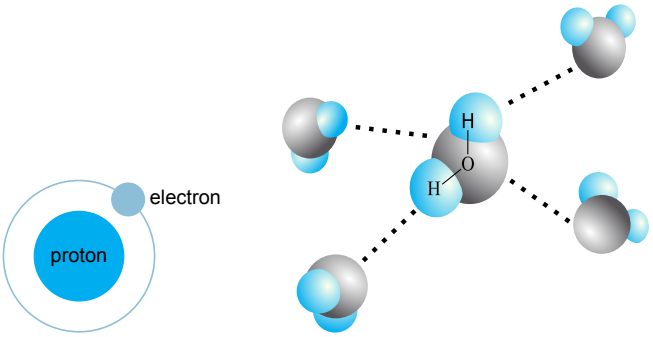

Figure 4.1: *(a)* ^1H *has a nucleus with one proton and no neutrons. Its electron shell consists of one electron which shields the proton from the applied magnetic field. (b) Hydrogen bonds (dashed lines) between water molecules pull the electrons away from the protons decreasing the nuclear shielding effect of the electrons.*

(Fig. 4.1a). With increasing temperature those hydrogen bonds stretch, bend, and break. This increases the nuclear shielding effect of the electrons and thus reduces the magnetic field $\boldsymbol{B}$ seen by the protons. The change of σ with temperature is given by the linear relationship

$$\Delta\sigma(T) = \alpha \cdot \Delta T, \tag{4.3}$$

where α is the temperature coefficient -0.01 ppm/°C which is independent of tissue type for a temperature range of -15°C to 100°C. However, due to the absence of hydrogen bonds this relationship does not hold for adipose tissues.

The relationship between σ and the proton resonance frequency at temperature $\omega(T)$ can be described by extending Eq. 2.6 to

$$\omega(T) = \gamma \cdot \|\boldsymbol{B}(T)\|_2 = \gamma \cdot \|\boldsymbol{B_0}\|_2 \, (1 - \sigma(T)). \tag{4.4}$$

A change in temperature thus induces a shift in the proton resonance frequency. This results in a phase shift in GRE images [Ishi 95] for which the phase Φ can be calculated by

$$\Phi(T) = \gamma \, \|\boldsymbol{B_0}\|_2 \, \sigma(T) \, TE. \tag{4.5}$$

As the temperature dependent and independent contributions to σ cannot be separated, the absolute temperature cannot be calculated. Rather the temperature change ΔT compared to a baseline temperature can. Based on the phase difference, the relative temperature change at time t can be calculated for each voxel by

$$\Delta T_t(u,v) = \frac{\Delta\Phi_t(u,v)}{\gamma\,\alpha\,\|\boldsymbol{B_0}\|_2\,TE} = \frac{\Phi_t(u,v) - \Phi_0(u,v)}{\gamma\,\alpha\,\|\boldsymbol{B_0}\|_2\,TE}, \tag{4.6}$$

where $\Phi_t(u,v)$ is the phase at time t and voxel (u,v). Φ_0 can be derived from a baseline phase image acquired before the thermal ablation (Fig. 4.2). If the baseline temperature T_0 is known the absolute temperature at time T_t can be calculated by

$$T_t(u,v) = T_0(u,v) + \Delta T_t(u,v). \tag{4.7}$$

Usually, the baseline temperature is set to body temperature of 37.2 °C.

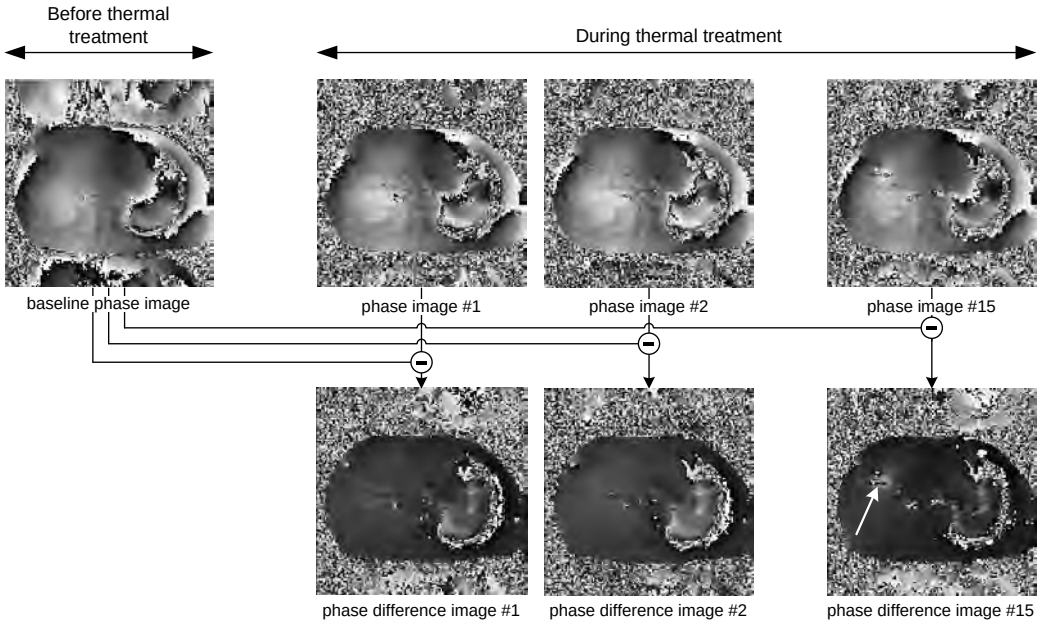

Figure 4.2: *Principle of PRF shift MR thermometry. Illustration of temperature change calculation during a laser-induced liver ablation. For each voxel the phase at time t is subtracted from the corresponding voxel in the baseline phase image. With progress of the ablation, the induced ablation zone can be clearly seen in the phase difference image (white arrow).*

4.2 Methods for Improving the Workflow

The PRF method itself has been extensively validated *in-vitro* [McDa 05]. To advance its use in a clinical setting hurdles associated both with workflow, and real-time visualization need to be overcome. Thus, the aim within this thesis was to develop and implement methods to allow for further exploration of MR thermometry in a clinical setting independent of the heating source used.

4.2.1 Dealing with Motion

The clinical applicability of MR thermometry has been shown for stationary targets such as uterine fibroids [McDa 06] and brain tumors [Carp 11]. Monitoring real-time temperature in moving organs, such as the kidney or liver, can be challenging as the PRF shift method is highly sensitive to motion due to the reference-based approach (Fig. 4.2). Both intra-scan, i.e. motion during one image acquisition, and inter-scan motion, i.e. motion between consecutive image acquisitions, need to be accounted for. The main source of motion in the abdomen is breathing motion [Maie 12]. Currently, respiration in MRI is monitored by either a breathing belt which is placed on the patient's abdomen to sense abdominal wall movement or by navigator echoes [Khle 11, Maie 12].

Intra-scan motion can be minimized by using fast acquisition techniques such as GRE EPI sequences which allow to acquire several lines up to the entire k-space in one TR as described in Section 2.3.3.

To deal with inter-scan motion several strategies exist. Clinically, respiration triggering is often used and has been demonstrated to be effective [Mori 04]. Another ap-

proach is the multi-baseline method [Vige 03] in which baseline images are acquired at various stages of respiration before the ablation. For temperature calculation the best registered phase image is then selected based on a similarity criterion between the current magnitude image and the baseline magnitude images. However, irregular breathing patterns in consciously sedated patients can present a challenge for both methods. Thus, 'reference-free' methods have been introduced which estimate the baseline phase from each acquired image itself [Riek 04, Kuro 06, Gris 10, Lang 11, Salo 12]. The background phase of the heated region is reconstructed by smoothly extending the image phase around the hot spot into it. Disadvantages of reference-free MR thermometry methods are that they require prior knowledge about the heating region for appropriate ROI selection. In addition, they are sensitive to rapid anatomical phase variations which commonly exist at organ interfaces. This is of importance e.g. for tumors in the upper liver segments close to the lung. For further information on strategies for dealing with motion in PRF-based MR thermometry, the interested reader is referred to [Deni 05, Riek 08, Yuan 12].

The clinical prototype implemented within this thesis supports both the reference-based PRF shift thermometry method as well as the 'reference-free' one proposed by Salomir et al. [Salo 12]. This method has recently been shown to outperform other 'reference-free' methods in terms of temperature accuracy [Tie 13].

Identification of Motion-Corrupted Images

From a workflow perspective the reference-based PRF method is easier to use in a clinical setting than reference-free strategies. First, it requires no prior knowledge about the heating region and thus is not dependent on appropriate ROI selection which requires experience with MR thermometry and can be challenging depending on the location of the lesion, in particular if it is at an organ interface. Second, the temperature can be monitored over the entire image, e.g. also along the applicator, and unexpected temperature changes can be detected as illustrated in Figure 4.3.

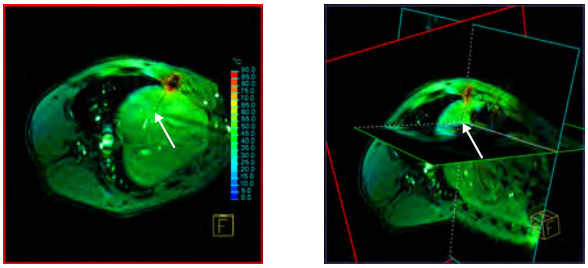

(a) (b)

Figure 4.3: *Reference-based PRF temperature monitoring over the entire image. The temperature increase is not at the planned heating spot (marked by arrows). The laser fiber had accidentally moved which was not detected in the magnitude MR images as the laser fiber is not visible once the introducing trocar has been removed.*

To further enhance the clinical use of reference-based MR thermometry, methods were developed to identify motion-corrupted PRF images.

Motion in magnitude images directly translates to non-temperature related phase shifts in the corresponding phase images and thus incorrect temperature. Weidenstei-

ner et al. [Weid 04] proposed to use cross-correlation for detection of motion-corrupted images. The cross-correlation coefficient P between the magnitude baseline image I_0 and the magnitude image I_t at time t during the procedure can be calculated by

$$P_{I_0,I_t} = \frac{\sum_{u=0}^{M-1}\sum_{v=0}^{N-1}\left(I_0(u,v)-\overline{I_0}\right)\left(I_t(u,v)-\overline{I_t}\right)}{\sqrt{\left[\sum_{u=0}^{M-1}\sum_{v=0}^{N-1}\left(I_0(u,v)-\overline{I_0}\right)^2\right]\left[\sum_{u=0}^{M-1}\sum_{v=0}^{N-1}\left(I_t(u,v)-\overline{I_t}\right)^2\right]}}, \tag{4.8}$$

where $\overline{I_0}$ is the mean gray value of the baseline magnitude image and $\overline{I_t}$ of the magnitude image at time t. Weidensteiner et al. proposed to calculate P over the entire image. However, our temperature stability study in prostate showed that this is not always sufficient. The prostate can move due to peristaltic movement and/or bladder filling. Figure 4.4 gives an example in which the patient had not moved but the prostate shows motion. By restricting the calculation of P to a region around the prostate, effective motion detection was possible. See Section 5.3.3 for further details.

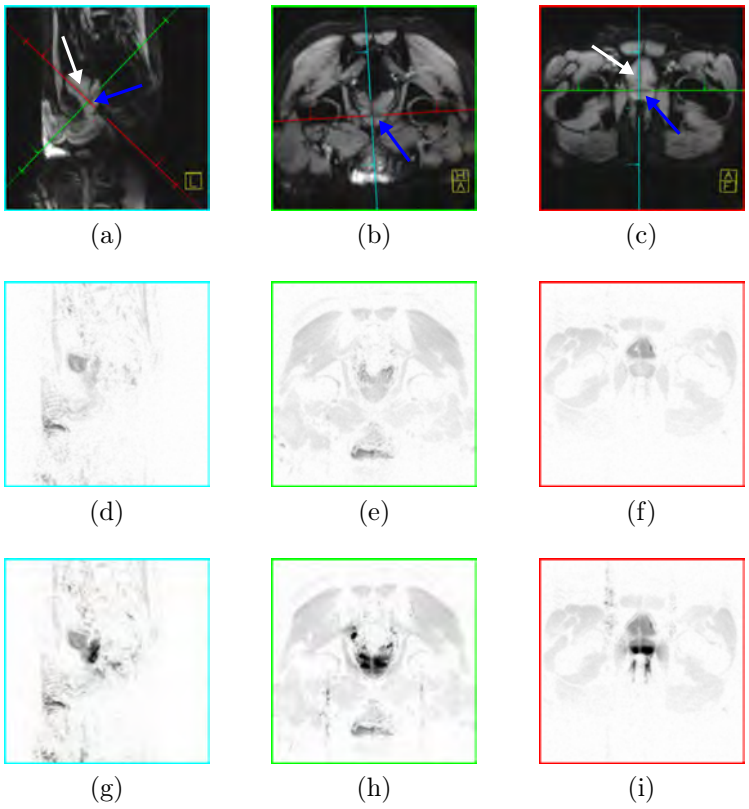

Figure 4.4: *Detection of prostate movement in magnitude difference images with slice alignment shown in (a)-(c). The prostate is marked by a blue arrow, the bladder by a white one. The difference images at time point 1 (d)-(f) show no prostate movement. At time point 3 (g)-(i), they show no bulk patient movement, but prostate movement is observed indicating that the temperature maps are corrupted.*

Besides setting a threshold for P_{I_0,I_t} below which images are automatically discarded, a method for visual detection of motion was developed. The incoming magnitude

images are subtracted from the baseline magnitude image and scaled by a user-defined factor s. The difference magnitude image D thus calculates by

$$D(u,v) = |I_0(u,v) - I_t(u,v)| \cdot s. \tag{4.9}$$

D is inverted and displayed in real-time in the monitoring panel of the user interface (UI). Thus, black regions indicate regions of potential motion. An example is given in Figure 4.4 demonstrating that motion of single organs can be well detected.

4.2.2 Automatic B_0 Drift Correction

From Equation 4.6 follows that reference-based PRF thermometry is very sensitive to variations of the external magnetic field $\boldsymbol{B_0}$. Variations in $\boldsymbol{B_0}$ can, for example, be caused by intense gradient utilization [El S 06]. They lead to an extra phase shift, commonly referred to as phase drift [Riek 08] which increases over time as illustrated in Figure 4.5. A change of 0.001 ppm in $\boldsymbol{B_0}$ results in a phase drift equivalent to a temperature shift of 1°C. Figure 4.6 illustrates this effect in an example of temperature monitoring over time in a volunteer's brain. In the absence of heating and continuous imaging for 13 minutes, $\boldsymbol{B_0}$ phase drift occurred resulting in an inaccurate temperature change measurement of more than 5°C. This illustrates the importance of correcting for $\boldsymbol{B_0}$ drift to allow for precise and reliable temperature monitoring, e.g. in MR-guided focused ultrasound procedures for treatment of various brain diseases [McDa 10, Jean 12]. The algorithm described in the following pages has been published in [Roth 11a, Roth 11c].

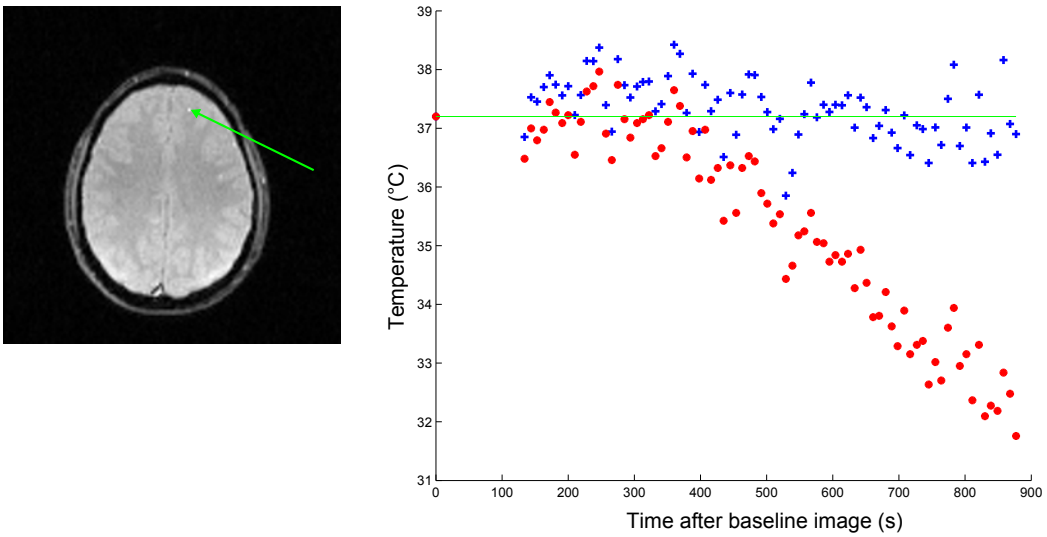

Figure 4.5: *Temperature over time for a voxel in the frontal lobe of the brain as marked in the magnitude image. The plot compares the uncorrected temperature over time (red) with the one corrected for $\boldsymbol{B_0}$ field drift (blue) by the proposed automatic approach.*

Algorithm

To correct for the $\boldsymbol{B_0}$ field drift over time, the mean phase drift μ_d can be calculated from a manually defined area which is not heated and thus remains at baseline temperature [De P 94]. Proper location and size selection of this region can be difficult

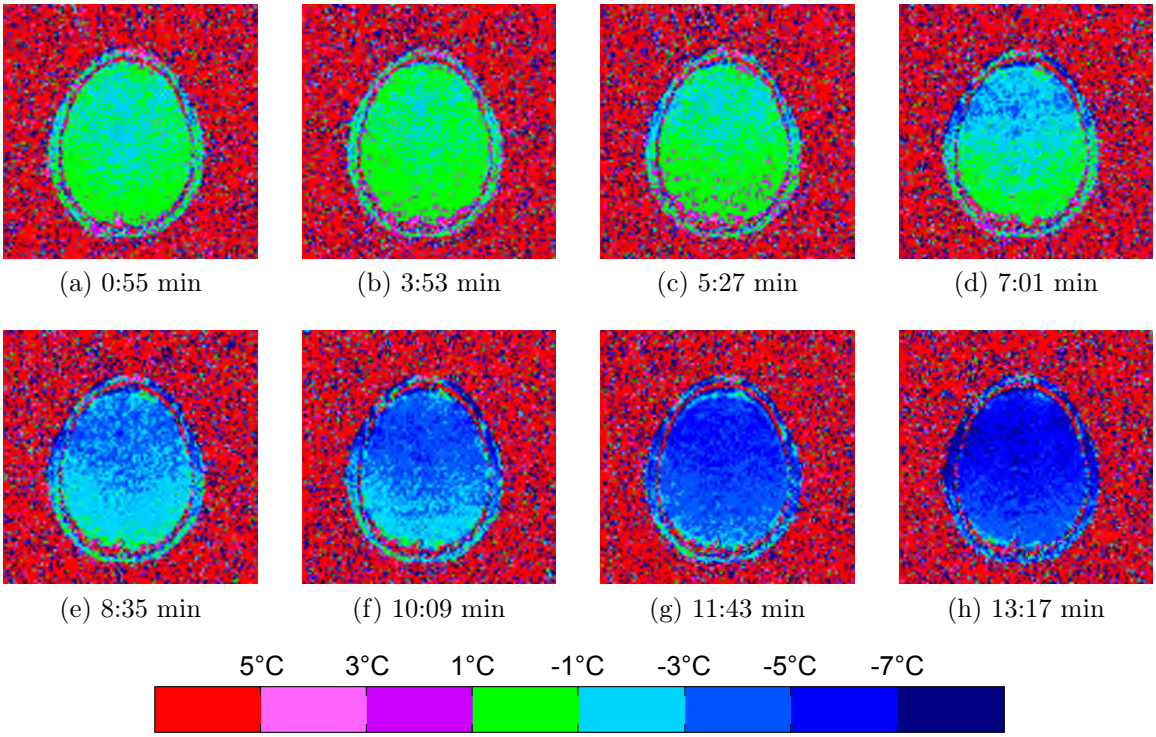

(a) 0:55 min (b) 3:53 min (c) 5:27 min (d) 7:01 min

(e) 8:35 min (f) 10:09 min (g) 11:43 min (h) 13:17 min

Figure 4.6*: Temperature maps over time in a volunteer's brain corrupted by* $\boldsymbol{B_0}$ *field drift. As no heat/cold was applied, there was no temperature drop as suggested by the temperature maps. The given times refer to the time difference from the baseline image acquisition.*

to place and is critical as it highly influences the effectiveness of correction. For an optimal result, the region needs to be placed at an area with maximal magnitude signal intensity and homogeneity, free of heating or motion during the intervention [Kick 10]. To simplify the application of $\boldsymbol{B_0}$ drift correction in a clinical setting, the goal was to develop a method which does not require any user interaction.

The proposed algorithm works by automatically determining the mean phase drift μ_d from all voxels which show a standard deviation smaller than a threshold θ_d in the phase. Having corrected the phase image $\Phi_t(u, v)$ at time t for $\boldsymbol{B_0}$ drift according to Algorithm 4.1, the relative temperature change $\Delta T_t(u, v)$ is then calculated by

$$\Delta T_t(u, v) = \frac{\Phi_{t_{corr}}(u, v) - \Phi_0(u, v)}{\gamma\, \alpha\, \|\boldsymbol{B_0}\|_2\, TE}, \tag{4.10}$$

where $\Phi_{t_{corr}}(u, v)$ is the corrected phase image. For MR thermometry in the brain, we propose a threshold based on the phase equivalent to 1°C, i.e. $\theta_d = \gamma\, \alpha\, \|\boldsymbol{B_0}\|_2\, TE$. Figure 4.7 shows the temperature maps from Figure 4.6 corrected by the proposed approach.

Algorithm 4.1: $\boldsymbol{B_0}$ drift correction

Input: $\Phi_t(u,v)$ with $u \in [0, M[$, $v \in [0, N[$ and $t \in [1, n]$ // phase images with images at $t < n$ corrected for $\boldsymbol{B_0}$ drift
M // number of columns
N // number of rows
n // current time point
θ_d // threshold for $\boldsymbol{B_0}$ drift correction
μ_d // mean phase drift
Output: $\Phi_{t_{corr}}(u,v)$ corrected phases image at $t = n$
begin
  $c \leftarrow 0$
  $d \leftarrow 0$
  for $u \leftarrow 0$ **to** $M-1$ **do**
    for $v \leftarrow 0$ **to** $N-1$ **do**
      $\mu_\Phi \leftarrow \frac{1}{n}\sum_{t=1}^{n}[\Phi_t(u,v) - \Phi_0(u,v)]$
      $\sigma_\Phi \leftarrow \sqrt{\frac{1}{n}\sum_{t=1}^{n}[\Phi_t(u,v) - \Phi_0(u,v)] - \mu_\Phi}$
      if $\sigma_\Phi < \theta_d$ **then**
        $d = \mathrm{d} + \mu_\Phi$
        $c = c + 1$
      end
    end
  end
  $\mu_d \leftarrow \frac{d}{c}$
  for $u \leftarrow 0$ **to** $M-1$ **do**
    for $v \leftarrow 0$ **to** $N-1$ **do**
      $\Phi_{t_{corr}}(u,v) = \Phi_t(u,v) + \mu_d$
    end
  end
end

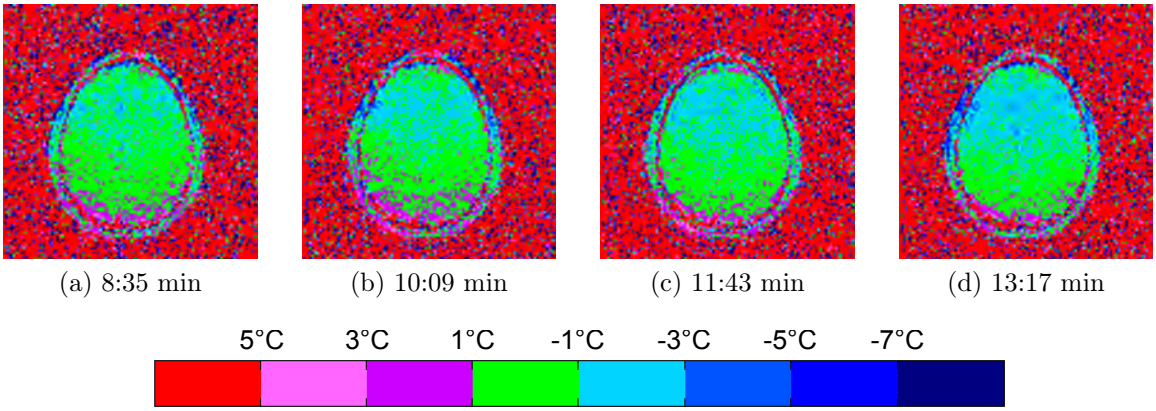

(a) 8:35 min (b) 10:09 min (c) 11:43 min (d) 13:17 min

Figure 4.7*: Temperature maps from Figure 4.6 (e) - (h) corrected by the proposed automatic* $\boldsymbol{B_0}$ *drift corerection approach.*

Evaluation

For validation of the proposed $\boldsymbol{B_0}$ drift correction algorithm, MR thermometry was performed on the brains of five volunteers (11 measurements) on a 1.5 T MR scanner (Siemens MAGNETOM Espree). The volunteers gave their written consent to the study. For continuous MR thermometry, the healthy volunteers' heads were positioned in a 12-channel head matrix coil with foam cushions to minimize motion. In neurosurgical interventions, the patient's head is usually fixed by either a stereotactic frame or a head holder with screws inserted into the skull.

For temperature acquisition, a GRE sequence was used as it is considered the gold standard for real-time MR temperature mapping [Kick 10]. To monitor the gradual $\boldsymbol{B_0}$ field drift, it was continuously imaged over 13 minutes in 3-7 axial slices with the following parameters: 17 msec TE, 156 msec TR, 25 ° flip angle, $2 \times 2 \times 2$ mm resolution, 160 Hz/Pixel bandwidth.

Analysis of temperature measurements was performed by calculating the mean deviation from baseline temperature in two regions of interest. One region was placed in the frontal lobe of the brain adjacent to the frontal sinus where susceptibility artifacts are most pronounced. The second region was positioned in the deep brain. The mean deviation from baseline temperature was significantly lower with the proposed automatic $\boldsymbol{B_0}$ drift correction than without. The median deviation from baseline temperature over all volunteers and slices for the frontal lobe was 0.8 °C (range, 0.6 - 1.4 °C) with and 1.4 °C (range, 0.7 - 2.4 °C) without $\boldsymbol{B_0}$ drift correction. For the deep brain, a median temperature deviation of 0.7 °C (range, 0.5 - 0.9 °C) with and 1.3 °C (range, 0.7 - 2.0 °C) without $\boldsymbol{B_0}$ drift correction was achieved. Those results are in the same range as the 0.58 °C ±0.28 reported by Kickhefel et al. [Kick 10] in which the manual $\boldsymbol{B_0}$ drift correction approach was applied. Table 4.1 provides an overview of the results demonstrating that the proposed method successfully corrects for zero-order phase drifts during MR thermometry without the need of manually defining an ROI for $\boldsymbol{B_0}$ drift correction or an additional stable reference.

Table 4.1: *Mean deviation in °C from baseline temperature over a 13 min PRF image acquisition period averaged over all slices. Numbers in parentheses are standard deviations.*

Measurement	Frontal lobe ROI		Deep brain ROI	
	Uncorrected	Corrected	Uncorrected	Corrected
1	2.4 (±2.0)	0.8 (±0.8)	1.8 (±1.7)	0.6 (±0.7)
2	1.5 (±1.4)	0.6 (±0.7)	1.3 (±1.3)	0.6 (±0.7)
3	1.3 (±1.6)	0.9 (±0.9)	1.5 (±1.8)	0.9 (±1.0)
4	2.2 (±2.0)	0.7 (±0.9)	2.0 (±1.9)	0.7 (±0.8)
5	1.0 (±1.1)	0.9 (±1.2)	1.0 (±1.1)	0.9 (±1.2)
6	1.4 (±1.3)	0.9 (±1.1)	1.5 (±1.3)	0.8 (±1.0)
7	1.0 (±1.0)	0.7 (±0.7)	1.2 (±0.9)	0.5 (±0.6)
8	0.7 (±0.8)	0.7 (±0.8)	0.7 (±0.7)	0.6 (±0.6)
9	1.1 (±1.3)	0.8 (±0.9)	1.0 (±1.1)	0.7 (±0.8)
10	1.7 (±0.9)	1.4 (±0.9)	1.0 (±0.9)	0.9 (±1.0)
11	1.0 (±1.1)	0.8 (±1.0)	1.0 (±1.2)	0.8 (±1.0)
All	**1.4**	**0.8**	**1.3**	**0.7**

4.2.3 Enhanced Visualization

For monitoring thermal ablations, both the anatomical (magnitude) and thermal (phase-based) images provide valuable and complementary information. The magnitude image delineates structural changes due to heating. However, the extent of irreversible tissue necrosis might be underestimated due to the fact that temperatures needed to induce structural changes are higher than temperatures needed to cause cell death. Consequently, for real-time assessment of the completeness of thermal therapy, it is desirable to also monitor the spatial and temporal temperature distribution using the phase images. The work presented in the following sections builds on the master's thesis [Roth 08] and has been partly published in [Roth 10a].

Fusing Anatomical and Thermal Information

The visualization of MR thermometry information at the user interface of current MR scanners is limited. An example is provided in Figure 4.8 which illustrates the visualization capabilities of the standard Siemens MR syngo UI. In the following paragraph, a method is presented which allows to fuse thermal information with magnitude images in an intuitive and consistent manner.

Usually, MR images are stored in 12-bits, while the display devices can only resolve 256 shades of gray. However, the brightness and contrast of an image can be changed by mapping the shade range linearly from $[c - \frac{w}{2}, c + \frac{w}{2}]$ to [0, 255], whereas center c

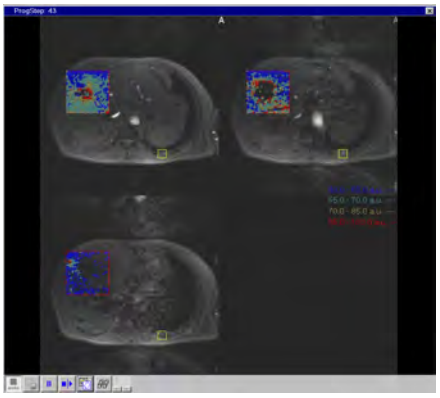

Figure 4.8: *Visualization of MR thermometry data on the Siemens syngo MR user interface. The derived temperatures are indicated by small crosses, the number of color bins is limited to four. The screen capture was acquired during an MR-guided laser ablation in liver.*

and width w are adjusted by the user with the mouse. The linear transformation is given by

$$g_o = \begin{cases} 0, & \text{if } g_i < g_{min}, \\ 255 \cdot \frac{g_i - g_{min}}{g_{max} - g_{min}}, & \text{if } g_{min} \leq g_i \leq g_{max}, \\ 255, & \text{otherwise}, \end{cases} \tag{4.11}$$

where g_o is the 8-bit output gray value and g_i the 12-bit input gray value. g_{min} is calculated by $\max(0, c - \frac{w}{2})$ and g_{max} by $\min(4095, c + \frac{w}{2})$.

As windowing is extensively used in MRI to highlight tissue boundaries, a method for combining gray values from magnitude images with color-coded thermal data was conceived based on the concept of luminance. It employs the HLS (hue, lightness, saturation) color space which is symmetric to lightness and darkness. As illustrated in Figure 4.9, fusion of anatomic and thermal images can be performed by combining the lightness value of each pixel in the magnitude image with the hue value of the corresponding pixel in the color coded temperature image to generate one joint HLS-coded pixel which is then converted to RGB for display.

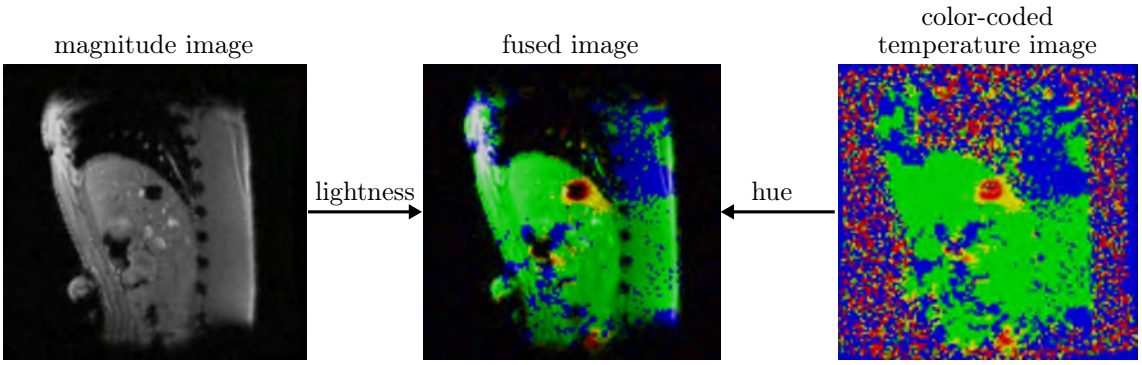

Figure 4.9: *Fusion of magnitude and color-coded temperature images employing the HLS color space. The images show an RF ablation in swine liver.*

Besides supporting intuitive and consistent windowing, another advantage of the fusion approach is that anatomical structures, such as large vessels which can cause

heat sink effects, are still well visible in the combined magnitude/temperature image. Furthermore, no thermal information is shown in areas with low signal. This simplifies the image interpretation as temperature in areas with low signal cannot be reliably calculated and their temperature values are unreliable. An example is given in Figure 4.9 in which the signal void in the center of the ablation zone was caused by the susceptibility artifact of the RF applicator. Figure 4.10 further illustrates the different visualization modes implemented in the clinical prototype which can be changed interactively during the intervention. The user can, for example, restrict the temperature overlay to an ROI around the treatment zone (Fig. 4.10b) or display isotherms (Fig. 4.10c) generated with the Marching Squares [Lore 87] algorithm. The 3-D view (Fig. 4.10d) further allows monitoring the progress of thermal ablation in space.

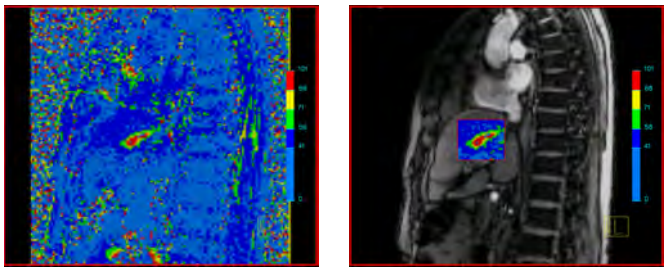

(a) Temperature map (b) Temperature ROI

(c) Isotherms (d) 3-D view

Figure 4.10*: Illustration of visualization modes for fusion of anatomical and thermal information.*

Enhanced Monitoring Capabilities

Thermal ablations can be performed with a variety of energy sources including RF, laser, FUS, microwaves, and cryo. Many centers not only work with one energy sources but use different energy sources depending on the tumor type, location, and size. However, the MR imaging component with respect to thermometry does not differ significantly between those procedures. Thus, the goal was to design one common UI for visualizing the treatment progress independent of the energy source used and tailored for an intuitive clinical workflow.

Figure 4.11 provides an overview of state-of-the art user interfaces designed for MR-guided thermal ablations. They are often linked to a specific device, like the 3D slicer for focused ultrasound (Fig. 4.11a) or the Visualase (Houston, TX) laser UI (Fig. 4.11b). However, MR-guided thermal ablations are usually not performed on a

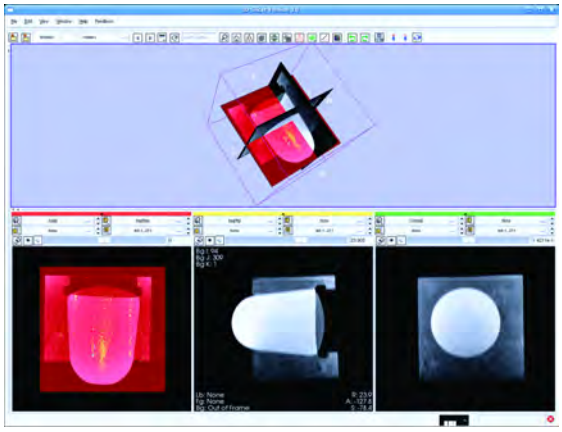

(a) 3D Slicer UI for focused ultrasound ablation. Image reproduced from [Yuan 12] with permission from AME Publishing Company.

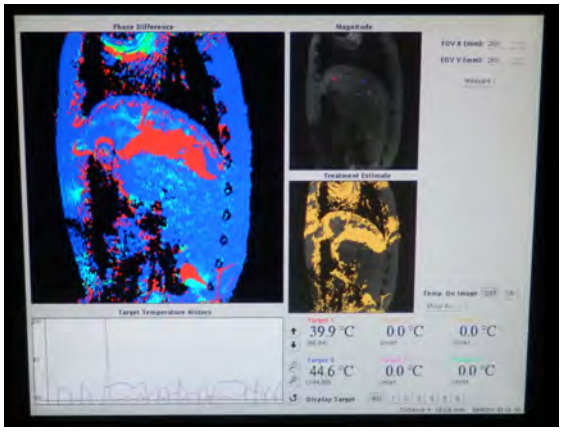

(b) Visualase (Houston, TX) laser ablation UI

Figure 4.11: *State-of-the art user interfaces designed for MR-guided thermal ablations. Further examples can be found in [Maie 09] and [Senn].*

daily basis and MRI requires special attention of the whole clinical team. Thus, it is advantageous to not also have to adapt to a different UI at every procedure but to have a framework which allows employing MR thermometry in a standardized fashion independent of the thermal device used.

The thermotherapy guidance tool developed within this work was implemented in C++ within the open source eXtensible Imaging Platform (XIP) [Pala 09] and integrated into the Interactive Front End (IFE) [Lore 05], a prototype for advanced visualization and real-time parameter control of MR image acquisition. To provide an intuitive and clear user interface, the thermotherapy guidance tool (TMAP) features visualization of up to three multi-planar slices. Magnitude and phase-based thermal images can be visualized either separately or fused (see previous section for algorithm), with flexibility to change the visualization mode interactively during the thermal ablation procedure. The thermal imaging slices can be displayed in individual 2-D views, as well as in a 3-D graphic which gives information about the orientation of the slices in 3-D space. Besides visualizing thermal images, the developed prototype can display the temperature over time for selected seed points, e.g. to monitor the temperature close to sensitive structures. In addition, it supports $\boldsymbol{B_0}$ drift correction (Sec. 4.2.2) which is not supported by any of the systems shown in (Fig. 4.11). To detect bulk patient motion or organ displacement (Sec. 4.2.1), magnitude difference images can be further displayed. Figure 4.12 presents a screen capture of the developed prototype which was used for multiple *in-vitro* and *in-vivo* studies as summarized in Chapter 5.

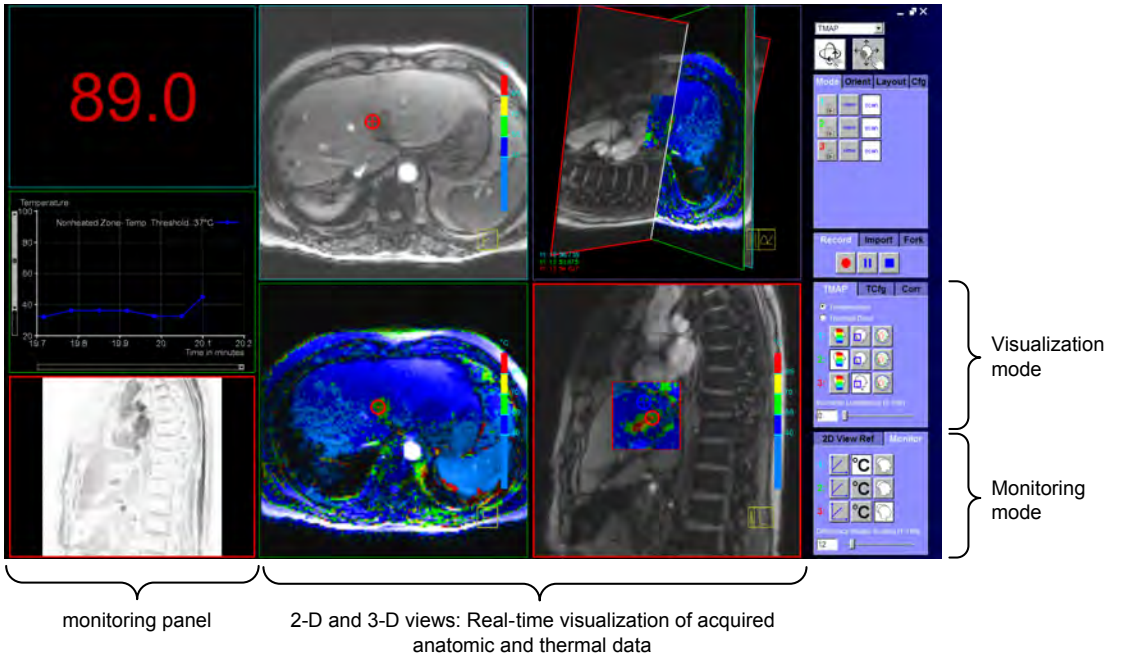

Figure 4.12: *Screen capture of developed thermotherapy guidance system showing a respiratory belt triggered laser-induced thermal ablation in the liver. In the monitoring panel on the left, the user can either display a difference image, the graph over time or the current temperature for a selected seed point. In the 2-D and 3-D views, the acquired slices are visualized in real-time according to the visualization mode set by the user in the control panel on the right. The colormap in this example was set by the physician performing the procedure. The generation of colormaps is very flexible, there are no restrictions to the number of bins or the individual bin width.*

4.3 Clinical Prototype

The methods presented throughout this thesis were implemented in a clinical prototype which is currently in use at over 20 sites worldwide. Chapter 5 provides an overview of the clinical studies performed so far. This section illustrates the interplay between the workflow modules and explains how the prototype is integrated into the MR scanner setup.

4.3.1 Integration of Workflow Modules

The clinical prototype implemented within this work supports the entire MR-guided thermal ablation workflow from planning to real-time temperature monitoring independent of the heating source used. As illustrated in Figure 4.13, the thermal ablation workflow can be divided into two key steps: 1) thermal applicator placement (planning and targeting) and 2) online temperature monitoring of thermal treatment. All three modules of the developed prototype were implemented in C++ within XIP and integrated into the IFE. In the following sections, the key features of each module are summarized and corresponding sections/figures throughout the thesis are referenced.

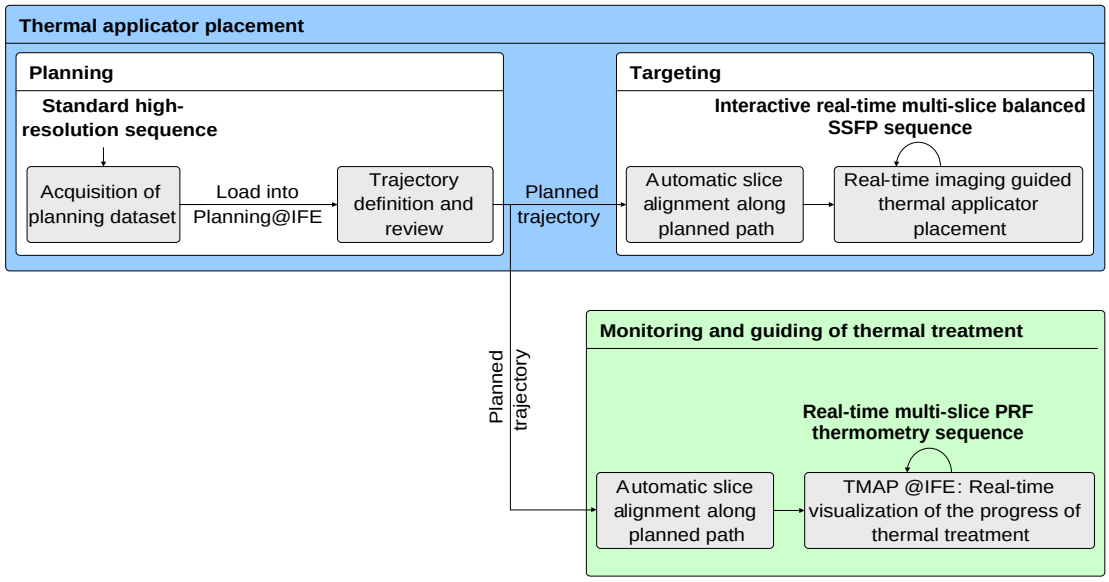

Figure 4.13: *Fully integrated system for MR-guided thermal ablations independent of the heating source used. Dedicated MRI pulse sequences are combined with visualization/analysis tools for trajectory planning, device placement, and advanced MR thermal mapping.*

Planning

Any treatment begins by identifying the best locations for thermal applicator placement such that the ablation zone adequately covers the target tumor but spares healthy and/or critical structures. Figure 4.14 shows the developed planning module. As described in Section 3.2.1, it allows for flexible visualization of any high-resolution dataset and definition of the needle trajectories in MPRs of any orientation. For reviewing the trajectory, the planned path can be overlaid on datasets with different contrasts, e.g. optimized for lesion visualization or optimal depiction of sensitive structures. The automatic slice alignment strategy (Sec. 3.2.4) further assists in reviewing the trajectory prior to applicator placement as it supports flying along the planned trajectory (Fig. 3.10). In addition, multiple trajectories can be planned in one session (Fig. 3.8b) which is useful for thermal ablations of large lesions that require accurate placement of several applicators in a defined spatial relationship to each other. Planning in one step further supports an efficient workflow as one does not have to break the scrub for planning the next needle trajectory. Figures 5.5a, 5.6a and 5.21a show screen captures of the planning module from clinical procedures.

Targeting

Having defined the trajectory, targeting can be performed at 2 to 5 frames per second using real-time imaging with an interactive multi-slice, balanced SSFP sequence (Sec. 2.3.2). The slices are automatically aligned along the prescribed trajectory as described in Section 3.2.3. This reduces the complexity of the needle placement and saves time as no manual slice alignment is needed. In addition, the resulting slice saturation bands (Fig. 3.15) can be used to guide thermal applicator placement. Figures 5.5b and 5.6b show screen captures of the targeting module from clinical procedures.

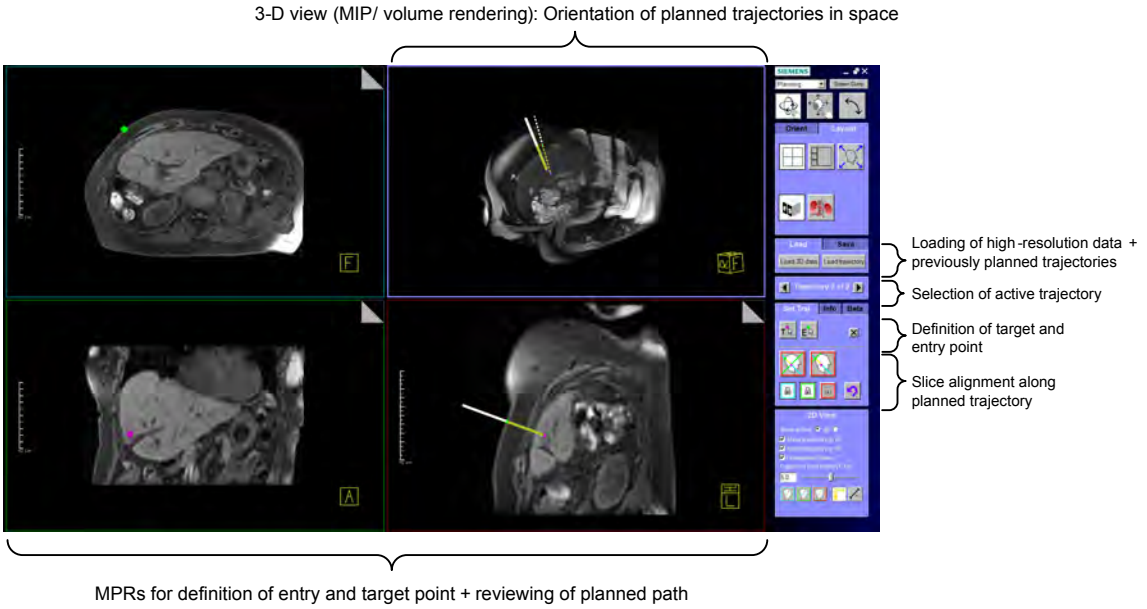

Figure 4.14: *Screen capture of the developed planning module. In this example, two RF applicators were placed along double-oblique trajectories into a liver lesion. The entry point was selected in an axial MPR and the target point in a coronal MPR. The sagittal slice was aligned along the planned trajectory using the proposed automatic slice alignment algorithm. The 3-D view shows the positions of the thermal applicators with respect to each other.*

Monitoring

The clinical prototype supports thermal treatment monitoring based on the proton resonance frequency using a multi-slice GRE EPI thermometry sequence with up to 5 frames per second (Sec. 4.1.3). Both the baseline subtraction as well as a reference-free approach are supported. The temperature imaging planes can be automatically aligned with respect to the planned trajectory based on the algorithm described in Section 3.2.4. Enhanced and $\boldsymbol{B_0}$ drift corrected temperature visualization (Sec. 4.2) combined with various monitoring tools supports accurate treatment monitoring.

The temperature monitoring tool has been designed to be independent of the heating source used. Figures 4.12 and 5.22b show screen captures from laser ablation procedures in patients. *In-vivo* studies using a range of ablation devices are shown in Figure 4.15.

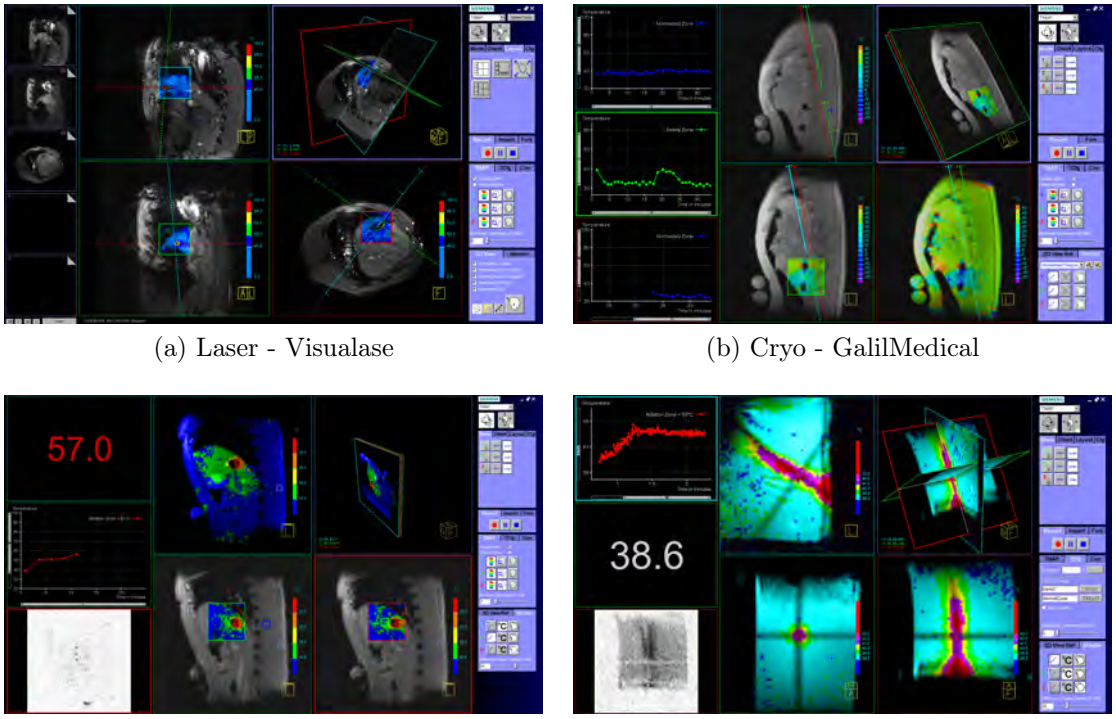

(a) Laser - Visualase (b) Cryo - GalilMedical

(c) RF - Olympus (d) FUS

Figure 4.15*: Screen captures of the developed temperature monitoring module during thermal ablations using a range of energy sources.*

4.3.2 Communication between Prototype and MR Scanner

The developed prototype runs on an independent PC (iMRI PC) connected to the standard Siemens MR scanner network via Ethernet and receives magnitude and phase pixel data acquired by the MR system in real-time. The pixel data is sent with additional header information like patient position, $\boldsymbol{B_0}$ field strength, slice position. Figure 4.16 illustrates the phase/magnitude data stream and further shows how the presented prototype can adjust protocol parameters (Fig. 4.17) via the remote protocol control tool [Lore 05] without any user interaction on the MR scanner side. In this work, this mechanism is used for automatic slice alignment along the planned path. The user interface of the clinical prototype is duplicated to an MR-compatible console (Fig. 5.10) inside the magnet room with an integrated mouse and/or displayed on a projection screen (Fig. 5.9).

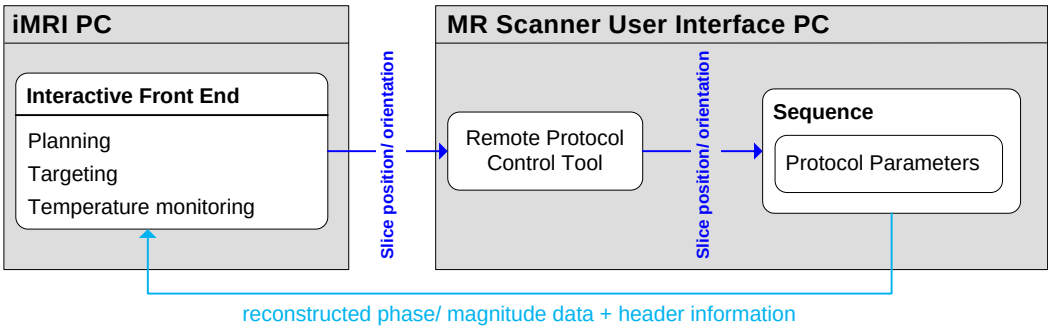

Figure 4.16: *Communication via TCP/IP between MR scanner and developed prototype running on the iMRI PC. The header contains information on slice position, orientation and information needed for temperature calculation, such as main magnetic field strength.*

Figure 4.17: *Siemens MR scanner UI with an interactive pulse sequence running (blue arrow). The displayed images are not updated in real-time which makes real-time slice alignment on the standard MR scanner UI challenging. Protocol parameters which can be changed during image acquisition are marked in white (green arrow). The user can reposition the real-time imaging slices by moving the yellow boxes in the top three viewports (yellow arrow). The developed prototype allows automatic alignment of those slices along the planned path.*

4.4 Summary

To make full use of the advantages of MRI for guiding thermal ablations and to enhance the clinical applicability of MR thermometry, an integrated solution supporting the entire thermal therapy workflow from thermal applicator placement to enhanced MR thermometry was developed. Image-based methods and tools were developed to reduce the complexity of performing MR thermometry in a clinical setting.

To allow for straightforward MR thermometry slice positioning covering the entire ablation zone, information about thermal applicator placement from the planning step is reused. The reliability of online temperature measurement is further improved both by automatically correcting for $\boldsymbol{B_0}$ drift and by identifying motion-corrupted images. As it is key to treatment success to correctly interpret the thermal data which is very sensitive to artifacts, anatomical and thermal data is fused in an intuitive way, enhanced by tools for closely monitoring the temperature over time for critical spots.

The studies presented in the next chapter show that the proposed integrated system is effective in guiding a variety of thermal ablation procedures. It is anticipated that the proposed methods will be useful in making MR-guided thermal ablations more effective and efficient, and could facilitate more widespread clinical adoption of MRI for guiding minimally-invasive thermal procedures.

Evaluation 5

This evaluation takes the reader through the entire imaging workflow for an MR-guided percutaneous procedure and examines the impact of the developed methods described in Chapter 3 and 4. Incorporation of the proposed methods in one CE-labeled clinical prototype (Sec. 4.3) allowed for extensive *in-vitro* and *in-vivo* validation. As accurate needle placement is essential for any thermal ablation or targeted drug delivery, the chapter starts by a phantom and animal study validating targeting accuracy and time of the proposed needle guidance methods (Sec. 5.1). Section 5.2 shows the clinical feasibility of the developed methods by summarizing the initial clinical experience for a range of MR-guided percutaneous procedures. The third section of this chapter presents studies for which the developed MR thermometry methods and framework have been used. Corresponding journal papers and conference proceedings are cited throughout the text.

5.1 Needle Guidance - Validation of Targeting Accuracy and Time

A central goal of this thesis was to develop methods for improving the workflow of MR-guided percutaneous procedures and to allow for accurate and efficient needle placement along complex trajectories by both "expert" and "non-expert" users. Chapter 3 provided the technical background. To validate targeting accuracy and time, phantom experiments (96 targets) and *in-vivo* paraspinal and kidney needle punctures in two pigs (55 targets) were performed. The influence of trajectory obliquity, level of experience and organ motion on targeting accuracy and time was analyzed.

The study was published in the Journal for Magnetic Resonance Imaging [Roth 13], the following sections are largely based on this publication.

5.1.1 Study Setup

Phantom Experiments

Ninety-six needle (20 gauge, 20 cm Chiba MReye biopsy needle [Cook, Bloomington, Indiana]) punctures were performed in a custom-designed stiff gelatin phantom (36 g per 500 ml pure water) with twelve embedded rubber O-rings (8 mm inner diameter). Twelve wooden beads (12 mm diameter) were also embedded to mimic vital structures to be avoided during the insertions. A layer of red gelatin was poured on top to

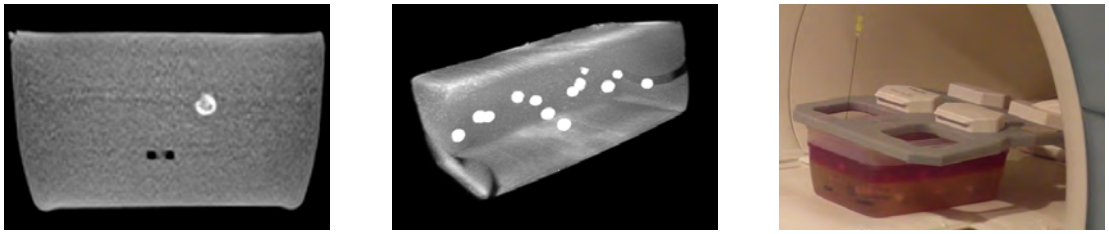

(a) (b) (c)

Figure 5.1*: Axial MR image (a), maximum intensity projection (b), and photograph (c) of gelatin phantom with embedded O-rings as targets and wooden beads to mimic vital structures.*

obstruct visibility of targets by the user from above. See Figure 5.1 for details of the phantom.

Following the procedure workflow proposed in Section 3.2, two "expert" interventionalists (5 and 15 years of experience) and two "non-expert" users (no interventional experience) selected and planned a single-oblique and a double-oblique trajectory for each target (24 needle insertions per users), reviewed the planned path to avoid the beads, localized the entry point on the phantom and inserted the needle along the planned path into the defined target point. A 3-D validation dataset was acquired after each insertion with the needle still in place to verify the needle position with respect to the planned path and target point.

Animal Experiments

The protocol for animal experiments was approved by the local institutional animal care and use committee. Fifty-five needle (20 gauge, 20 cm Chiba MReye) insertions were performed by an expert interventionalist in two living pigs (45 - 50 kg). The animals were initially sedated with an intramuscular injection of dexmedetomidine 0.8-1 ml and Ketamine, 10 mg/kg, then intubated and maintained on a mechanical ventilator with inhaled 1 % - 1.5 % isoflurane. The animals were positioned on the MR scanner table prone or decubitus.

Twenty points in the paraspinal muscles of the two pigs were selected as targets. To validate the proposed methods in a moving organ, 35 target points were further selected in all segments of the kidney. The task was to insert the needle into the target point following the planned trajectory. The planned path, entry and target points could be displayed as overlays on the real-time images. Following the procedure workflow proposed in Section 3.2, the interventionalist first planned and reviewed the trajectory to the defined target point. Depending on the target location, the trajectory was planned within a single slice plane (single-oblique) or using two planes (double-oblique). Trajectory lengths ranged between 30 and 88 mm. The lateral localization of the entry point in this study was identified by measuring the x-offset from the laser-cross hairs (Fig. 5.2a). The advanced method proposed in Section 3.2.2 was developed as a result of this study.

The needle insertions were planned in groups of five to mimic a complicated procedure and to allow for assessment of procedure time for multiple needle placements

(a) Entry point localization (b) Targeting under real-time image guidance

Figure 5.2*: Setup for in-vivo needle guidance study on a 1.5 T Siemens MAGNETOM Espree scanner. (a) The entry point is localized using the method described in Section 3.2.2. The needle is positioned through the hole in the 6-element body matrix coil (see arrow). (b) The developed needle guidance user interface is displayed on a screen inside the MR scanner room. Noise reduction optical headsets (Optoacoustic, Or-Yehuda, Israel) are used for communication with the control room (see arrow).*

in a single patient. During free breathing, the needles were inserted in a single advancement into the target point, 10 along single-oblique and 10 along double-oblique trajectories for the paraspinal targets, and 13 along single-oblique and 22 along double-oblique trajectories for the targets in the kidney. A 3-D validation dataset was acquired after each insertion with the needle still in place to verify the needle position with respect to the planned path and target point.

MR Imaging Protocol

MR imaging was performed on a wide-bore 1.5 T MR scanner (MAGNETOM Espree, Siemens Healthcare, Erlangen, Germany) using the 6-element body matrix coil combined with 6 elements of the spine matrix coil (Fig. 5.2a). The real-time navigation user interface was projected onto a screen in the scanner room (Fig. 5.2b) to provide live feedback about the current needle position to the user.

The imaging protocol consisted of (a) acquisition of a 3-D planning dataset by using a three-dimensional T1-weighted gradient echo sequence (volumetric interpolated breath-hold examination (VIBE)), (b) real-time imaging during the procedure using a real-time, interactive, multi-slice balanced SSFP sequence (Sec. 2.3.2), (c) re-acquisition of (a) with the needle in place for validation of needle position with respect to the planned path.

For the phantom experiments, VIBE images were acquired in 41 seconds covering 144 slices (4.88 msec repetition time (TR), 2.38 msec echo time (TE), 10° flip-angle, 2 mm slice thickness, 140×200 mm FOV, 112×160 matrix). For the animal experiments, 104 - 128 slices were acquired under breath-hold conditions in 35 - 38 seconds (5 msec TR, 2 msec TE, 9° flip-angle, 2 mm slice thickness, (233-250) × (320-340) mm FOV, (352-400) × 512 matrix).

The needles were placed free-breathing using real-time, multi-slice interactive imaging (4.6 msec TR, 2.3 msec TE, 60° flip-angle, 5 - 10 mm slice thickness, 300 × 300 mm FOV, 192 × 192 matrix, imaging time of 0.5 seconds per plane). All real-time and

VIBE imaging was performed with GRAPPA [Gris 02] parallel imaging (acceleration factor 2, 24 reference lines).

Data Analysis

For evaluation of targeting accuracy in phantom and animal experiments, the needle centerline was manually segmented in each 3-D verification dataset by selecting the entry and target point (consensus by three observers). In-plane, out-of-plane, and total 3-D errors were calculated by comparing the 3-D coordinates of the segmented needle centerlines and the 3-D coordinates of the corresponding planned trajectories (Fig. 5.3). For calculation of the targeting error in x and y direction, a plane is placed parallel to the target plane at the segmented target point $\boldsymbol{p}_{\mathrm{t_s}}$. The in-plane error is then calculated by

$$d_{in-plane} = \frac{\left\|(\boldsymbol{p}_{\mathrm{t}} - \boldsymbol{p}_{\mathrm{e}}) \cdot (\boldsymbol{p}_{\mathrm{t_s}} - \boldsymbol{p}_{\mathrm{e}})\right\|_2}{\left\|\boldsymbol{p}_{\mathrm{t}} - \boldsymbol{p}_{\mathrm{e}}\right\|_2}, \tag{5.1}$$

where $\boldsymbol{p}_{\mathrm{e}} \in \mathbb{R}^3$ is the planned entry point, $\boldsymbol{p}_{\mathrm{t}} \in \mathbb{R}^3$ the planned target point, and $\boldsymbol{p}_{\mathrm{t_s}} \in \mathbb{R}^3$ the segmented target point. The out-of-plane error is given by

$$d_{\mathrm{out-of-plane}} = \left\|\boldsymbol{p}_{\mathrm{t}} - \boldsymbol{\Gamma}\right\|_2, \tag{5.2}$$

where $\boldsymbol{\Gamma}$ is the projection of $\boldsymbol{p}_{\mathrm{t_s}}$ on the planned trajectory (see Eq. 3.16). The 3-D error is calculated by

$$d_{3D} = \left\|\boldsymbol{p}_{\mathrm{t_s}} - \boldsymbol{p}_{\mathrm{t}}\right\|_2. \tag{5.3}$$

The influence of trajectory obliquity, level of experience, and organ type on targeting accuracy was analyzed using two-way analysis of variance (ANOVA) with one factor being trajectory obliquity (single-, double-oblique) and the other factor being level of expertise (non-expert, expert) for the phantom study and organ type (paraspinal muscle, kidney) for the *in-vivo* study.

Time needed for preprocedure imaging, planning, entry point localization, targeting, and verification imaging was recorded. As the assumption of normality was not met for targeting time, the non-parametric Kruskal-Wallis [Krus 52] test was used to analyze differences in targeting time for single versus double-oblique trajectories, non-expert versus expert users for the phantom experiments, and paraspinal versus kidney for the animal experiments. Linear regression was performed to analyze trajectory length vs. targeting error. For all evaluations, a significance level of $p < 0.05$ was used.

5.1.2 Results

Phantom Experiments

All 96 targets were successfully punctured with a mean skin-to-target time of 100 ± 50 seconds. The Kruskal-Wallis test revealed a significant difference in targeting time between single and double-oblique paths ($p = 0.03$). Expert users were significantly faster than non-expert users for single-oblique paths ($p = 0.03$) but not for double-oblique paths ($p = 0.18$). The median path length for single-oblique paths was 71 mm (range, 64 - 94 mm) and 79 mm (range, 66 - 116 mm) for double-oblique paths.

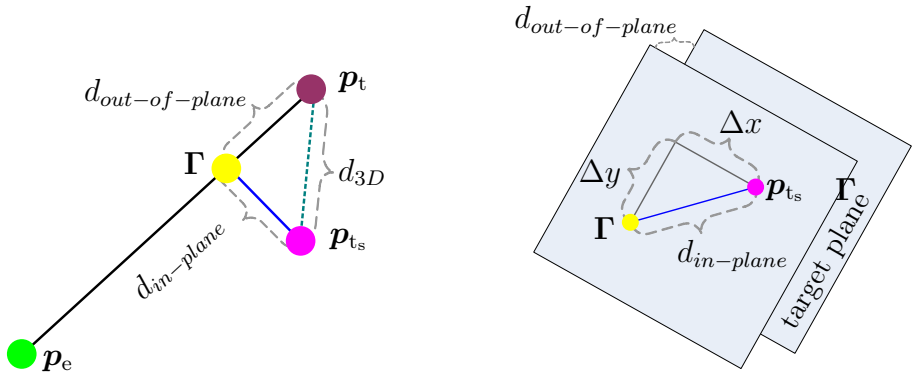

(a) Out-of-plane and 3-D error (b) In-plane error

Figure 5.3: *Targeting error calculation with the planned trajectory defined by $\boldsymbol{p}_e$ and $\boldsymbol{p}_t$. (a) $\boldsymbol{p}_{t_s}$ is the segmented 3-D target point and $\boldsymbol{\Gamma}$ is the projection of $\boldsymbol{p}_{t_s}$ onto the planned trajectory. (b) For in-plane error (blue line) calculation, a plane is placed at the segmented target point $\boldsymbol{p}_{t_s}$ parallel to the target plane used during real-time needle guidance.*

As illustrated in Figure 5.4a, no relation could be found between trajectory length and targeting error.

The mean targeting error was 1.8 ± 1.5 mm (standard deviation) in all directions. Detailed results are given in Table 5.2. Two-way ANOVA showed no significant difference in targeting accuracy between non-expert and expert users (p = 0.36) and between single and double-oblique paths (p = 0.19). No interaction effect between level of expertise and trajectory obliquity on targeting accuracy was found (p = 0.85). The mean 3-D distance between the actual entry point and the planned trajectory was 3.9 ± 2.3 mm.

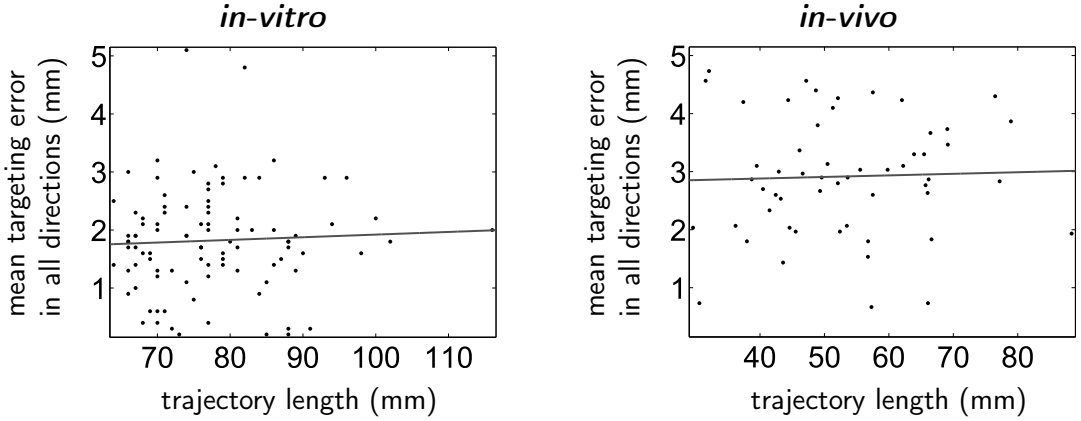

(a) (b)

Figure 5.4: *The targeting error is independent of trajectory length for both in-vitro (a) and in-vivo (b). The solid lines represent the linear regression fits.*

Animal Experiments

All 55 needles were successfully placed into the selected target points with a mean intervention time from acquisition of planning images to verification of correct needle

placement of 6 minutes. The mean skin-to-target time was 113 ± 57 seconds, with further details on the components of the procedure times given in Table 5.1. The Kruskal-Wallis test showed no significant difference in targeting time between paraspinal and kidney insertions ($p = 0.80$) but a significant difference between single and double-oblique trajectories ($p = 0.003$). The median path length was 49 mm (range, 30 - 69 mm) for single-oblique paths and 55 mm (range, 31 - 88 mm) for double-oblique paths. As illustrated in Figure 5.4b, the targeting error was independent of the trajectory length.

The mean targeting error was 2.9 ± 1.9 mm in all directions. Detailed results are given in Table 5.2. Two-way ANOVA showed no significant difference in targeting accuracy between paraspinal and kidney insertions ($p = 0.26$) and between single and double-oblique trajectories ($p = 0.90$). There was no significant interaction effect between targeted organ and trajectory obliquity on targeting accuracy ($p = 0.14$). The mean 3-D distance between the actual entry point (i.e. skin nick) and the entry point of the planned trajectory was 5.1 ± 2.6 mm.

Table 5.1: *Procedure time for in-vivo study. The total intervention time includes planning, entry point localization, targeting, and verification for 5 needles.*

Parameter		**Time**
Preprocedure imaging time (scout images + planning dataset)		70 sec
Mean planning time		6 ± 2 min for 5 needles
Entry point localization time		< 60 sec
Mean skin-to-target time per needle		113 ± 57 sec
Verification imaging time		41 sec
		Total intervention time
Animal 1	Procedure 1 - 2: Paraspinal	26 min/ 26 min
	Procedure 3 - 5: Kidney	24 min/ 23 min/ 27 min
Animal 2	Procedure 6 - 7: Paraspinal	23 min/ 18 min
	Procedure 8 - 11: Kidney	22 min/ 18 min/ 21 min

Table 5.2: *Targeting accuracy and time for needle guidance study. Numbers in parentheses are standard deviations.*

	Mean targeting error (mm)				Mean targeting time
	In-plane		Out-of-plane	Total	
	Δx	Δy			
Phantom Single-Oblique Paths					
Novice users n=24	2.3 (±1.5)	1.3 (±1.0) 1.7 (±1.5)	1.9 (±1.5)	3.3 (±1.6)	1:46 (±0:36)
Expert users n=24	3.1 (±1.5)	2.1 (±1.6) 1.8 (±1.3)	1.2 (±1.0)	3.6 (±1.3)	1:08 (±0:35)
Phantom Double-Oblique Paths					
Novice users n=24	3.0 (±1.9)	1.6 (±1.3) 2.2 (±1.9)	1.9 (±1.3)	3.7 (±2.0)	2:04 (±0:47)
Expert users n=24	2.7 (±1.3)	1.8 (±1.4) 1.7 (±1.0)	2.7 (±2.0)	4.1 (±1.9)	1:42 (±1:02)
Phantom All Paths					
All paths n=96	2.8 (±1.6)	1.7 (±1.4) 1.9 (±1.4)	1.9 (±1.6)	3.7 (±1.8)	1:40 (±0:50)
***In-Vivo* Single-Oblique Paths**					
Paraspinal n=10	3.9 (±0.9)	2.7 (±0.6) 2.4 (±1.7)	3.0 (±2.1)	5.1 (±1.7)	1:23 (±30)
Kidney n=13	5.9 (±1.7)	3.7 (±1.6) 4.2 (±1.9)	2.1 (±1.8)	6.4 (±1.8)	1:31 (±0:43)
***In-Vivo* Double-Oblique Paths**					
Paraspinal n=10	5.2 (±2.2)	2.5 (±2.3) 4.1 (±2.0)	2.1 (±1.3)	5.8 (±2.0)	2:09 (±0:56)
Kidney n=22	4.8 (±1.8)	3.4 (±1.7) 2.5 (±1.8)	2.2 (±2.0)	5.5 (±1.7)	2:19 (±1:18)
***In-Vivo* All Paths**					
All paths n=55	4.9 (±1.8)	3.2 (±1.7) 3.2 (±2.0)	2.3 (±1.9)	5.7 (±1.8)	1:53 (±0:57)

5.1.3 Discussion

Targeting accuracy is essential for successful image-guided therapy. An in-plane error of 5 mm is clinically acceptable in most situations. This study evaluated not only the in-plane error but also the out-of-plane error for both phantom and *in-vivo* studies, and showed that in-phantom non-expert users were able to perform needle insertions within this accuracy limit even for double-oblique trajectories (Table 5.2). Only two of the *in-vivo* studies on manual MR-guided percutaneous interventions listed in Table 5.3 report targeting accuracy. The results are equivalent to the median lateral deviation of 3.4 mm found by Stattaus et al. [Stat 08b] and significantly better than the 3-D targeting error of 9.6 mm reported by Wacker et al. [Wack 06]. Moreover, the measured needle placement accuracy in phantoms is in the same range as reported by others for stereotactic methods and significantly better than for the freehand approach (Table 5.4). The accuracies achieved in this study are potentiated by continuous visualization of the needle in three planes aligned with preference to the principal patient axes and the precise skin entry point localization.

Reduced table time plays a central role for adoption of MR-guided percutaneous needle interventions beyond academic centers. Without introducing any additional hardware, less than 30 minutes (from planning to verification) were needed to place five needles in the kidney or spinal muscle of pigs (on average 6 minutes per needle). This is significantly shorter than what has been reported in literature for manual MR-guided percutaneous interventions (Table 5.3).

Table 5.3: *Comparison of reported times for in-vivo studies on manual MR-guided percutaneous interventions in abdominal target locations.*

Author	Organ (# cases)	Time
in-bore, freehand		
1 T Panorama, Philips		
Fischbach 2011 [Fisc 11]	Liver (50)	Mean intervention time (planning to verification): 18 min (range, 15-35 min)
Ricke 2010 [Rick 10]	Liver (224)	Mean intervention time (planning to dosimetry data acquisition): 64 min (range, 29-174 min)
Streitparth 2010 [Stre 10]	Nerve root (107), facet (53), sacroiliac joint (23)	Mean procedure time: 29 min (range, 19-67 min)
1.5 T MAGNETOM Espree, Siemens		
Fritz 2009 [Frit 09]	Nerve root (22), facet (18), epidural (9)	Mean table time: 36 min (range, 23-75 min) Mean real-time MRI: 38 sec (range, 12-185 sec)

Fritz 2008 [Frit 08]	Sacroiliac joint (60)	Mean intervention time (entry point localization to needle retraction): 22.5 min (range, 5.0-67.5 min)
Stattaus 2008 [Stat 08b]	Liver (20)	Median puncture time (finger-pointing to needle placement): 19 min (range, 12-43 min)
Hoffmann 2012 [Hoff 12]	Liver (19), soft-tissue (19)	Mean planning time: 64 min (liver); 43 min (soft-tissue) Mean puncture time (needle insertion to retraction): 18 min (soft-tissue); 43 min (liver) Mean total procedure time: 134 min (liver range, 57 94 min); 73 min (soft-tissue - range, 30-121 min)
0.2 T MAGNETOM Concerto, Siemens		
Zangos 2006 [Zang 06]	Paraaortic (20), kidney (2), adrenal gland (3), pancreas (5)	Median intervention time (needle insertion to retraction): 12.3 min (range, 6.3-16.8 min)
0.3 T Airis I, Hitachi		
Sakarya 2003 [Saka 03]	Lung (14)	Mean biopsy duration (planning to needle placement): 19 min (range, 15-28 min)
0.5 T Signa SP, GE		
Genant 2002 [Gena 02]	Spine + paraspinal (14), pelvic (17), upper extremities (13), foot and ankle (7), knee and leg (6), miscellaneous (6)	Mean needle time (needle insertion to retraction): 26.2 min ± 19.7.
in-bore, optical tracking		
0.23 T Panorama, Philips		
Ojala 2002 [Ojal 02]	Bone (5)	Procedure time (needle insertion to retraction): < 40 min
Sequeiros 2002 [Sequ 02]	Nerve root (61)	Mean puncture time (needle insertion to retraction): 12 min (range, 2-60 min)
in-and-out, freehand		
1.5 T MAGNETOM Avanto, Siemens		
Das 2010 [Das 10]	Liver (4), pancreas (4), retroperitoneum (2)	Mean total procedure time: 59.7 min (range, 46-70 min) intervention time: 20-25 min

3 T MAGNETOM Trio, Siemens		
Kühn 2010 [Khn 10]	Liver (47), spleen (1), kidney (2)	Median intervention time (insertion to retraction): 9.3 min ± 8.1
out-of-bore, optical tracking/ augmented reality		
1.5 T MAGNETOM Symphony, Siemens		
Busse 2010 [Buss 10]	Scapula (1)	Technical setup: 5 min Patient positioning: 10 min Planning (marker and roadmap images acquisition): 9 min Patient preparation and access planning: 15 min
1.5 T MAGNETOM Espree, Siemens		
Wacker 2006 [Wack 06]	3 Pigs	Mean puncture time (planning to verification): 13 min

Table 5.4: *In-vitro studies on manual MR-guided percutaneous interventions: Comparison of reported targeting accuracies.*

Author	Method	Accuracy
Busse 2010 [Buss 10]	Optical tracking	Mean in-plane error: 3.1 mm (range, 1.0-5.8 mm) Mean out-of-plane error: 4.5 mm (range, 2.0-7.0 mm)
Fischer 2007 [Fisc 07a]	Freehand	Mean in-plane error: 5.2 ± 5.56 mm Mean orientation error: 4.07° ± 4.11°
	Protractor	Mean in-plane error: 5.37 ± 7.36 mm Mean orientation error: 3.35° ± 3.34°
	Laser	Mean in-plane error: 2.90 ± 2.62 mm Mean orientation error: 2.02° ± 2.22°
	Overlay	Mean in-plane error: 2.00 ± 1.70 mm Mean orientation error: 2.41° ± 2.27°
Christoforou 2007 [Chri 07]	Manipulator-driven	Mean 3D error: 3.2 mm Mean orientation error: 2.5°
Wacker 2006 [Wack 06]	Augmented reality	Mean minimum in-plane distance: 1.44 mm Mean out-of-plane error: 2.55 mm

5.2 Needle Guidance - Patient Cases

Beyond validation, clinical translation of the developed methods could be demonstrated for a variety of percutaneous minimally-invasive procedures. Table 5.5 gives an overview of the first patient cases performed with the prototype. All patients were successfully treated. Targeting refers to the time needed for real-time MR-guided needle placement. The average targeting time indicates that the developed methods allow for fast needle placement also in moving organs (liver ablation and abdominal biopsies). To further illustrate the clinical use of the developed methods, example patient cases are presented in the following sections. First publications are [Bret 12] and [Roth 12a]. All cases have in common that they were performed on a wide-bore 1.5 T MR scanner (Siemens MAGNETOM Espree). For signal reception a 6 element body matrix coil was used in combination with 6 elements of the spine matrix.

Table 5.5: *First patient cases performed with prototype developed within this thesis. Average time per patient is reported.*

Procedure (# patients - needles)	**Avg. path length**	**Average time**		
		Targeting	**MR-imaging**	**Non-imaging**
Thermal ablation (1 - 2)	81.5 mm	4.5 min	41 min	187 min
Abdominal biopsy (3 - 3)	76 mm range,47-100	6 min range, 5-7	12 min range, 9-15	44 min range, 38-54
Sclerotherapy (4 - 13)	95 mm range, 38-122	3 min range, 0.5-10	34 min range, 20-60	107 min range, 74 -146
Spinal infiltration (10 - 10)	61 mm range, 45-98	3 min range, 1-6	6 min range, 2-12	22 min range, 12-34

5.2.1 Thermal Ablation - Tübingen

Thermal ablations are increasingly used as a local treatment option to supplement systemic treatment strategies such as chemotherapy and immunotherapy [Tatl 07, Riek 08]. RFA is widely used for treatment of liver cancer [Marr 06], that is hepatocellular carcinoma or colon cancer that metastasizes from the colon to the liver.

In the presented RFA case, two internally cooled MR-compatible RF applicators (Celon, Tretow, Germany) were placed into an unresectable liver lesion. Further details on the technical principles of RFA can be found in (Chap. 4.1.1). The patient was positioned feet-first supine into the wide-bore MR scanner. The procedure was performed under analgesic sedation.The two entry points were localized in one session as described in Section 3.2.2 and marked on the patient's skin. The RF applicators were placed under continuous imaging with automatic initial slice alignment along the planned path (Fig. 5.5). The needles were pushed forward under real-time image guidance and if needed the slice positions were interactively adjusted.

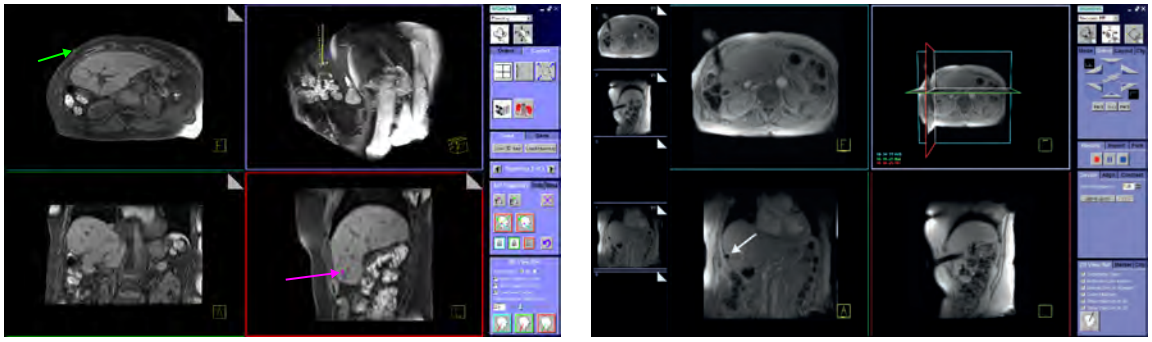

(a) (b)

Figure 5.5: *RFA in the liver, screen captures of developed needle guidance prototype. (a) Planning of placement of two RF applicators into liver lesion with the target point (magenta dot) of the second trajectory placed in the sagittal slice and the entry point (green dot) in the axial one. (b) Applicator placement under continuous imaging using a real-time GRE sequence. The cross-sectional needle artifact (see arrow) in the coronal plane positioned at the tumor location indicates that the thermal applicator is in place.*

5.2.2 Abdominal Biopsy - Strasbourg

Due to the increasing use and sensitivity of imaging methods the detection of incidental small lesions which require histological diagnosis has increased [Zang 06]. Most abdominal biopsies are currently performed using either CT or US image guidance. However, there are cases which justify the use of MRIhif. Firstly, this holds for target structures which are not sufficiently visualized using the standard imaging modalities and the patient might otherwise have to undergo more invasive procedures. Secondly, the high soft-tissue contrast of MRI allows for an increased biopsy yield by guiding the needle into viable tumor tissue instead of necrotic areas [Deng 09]. Finally, MRI is attractive for targets in locations requiring a highly angulated approach and non-axial scan planes, such as hepatic dome or adrenal lesions. An example for such a highly angulated biopsy path is presented in the following case.

A kidney biopsy in a 64-year old male patient was performed under local anesthesia. For planning a T2-weighted 3-D dataset was used (BLADE: 134 msec TE, 2800 msec TR, 150° flip angle, 380×380 mm FOV, 3 mm slice thickness, 1.5 mm reconstructed in-plane resolution, 68 seconds total acquisition time). Figure 5.6a shows the planning stage after automatic MPR alignment along the planned trajectory. A real-time balanced SSFP sequence (Sec. 2.3.2) was used for needle guidance. The needle was placed into the tumor under continuous imaging with the patient free breathing, Figure 5.6b provides a screen capture of the targeting step. The total targeting imaging time was 6 minutes 21 seconds with a total procedure time of 49 minutes.

5.2.3 Targeted Drug Delivery

Targeted delivery of a therapeutic agent allows for a high therapeutic efficacy with minimal systemic effects [Arep 08]. Sclerotherapy and spinal infiltrations are two examples.

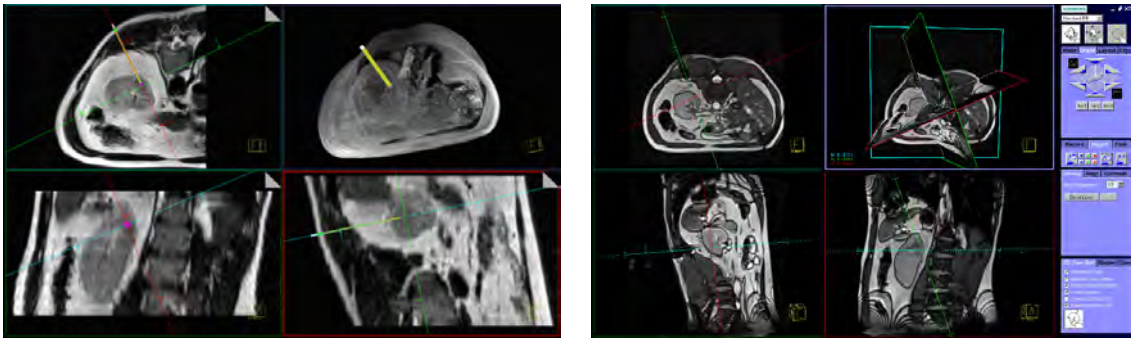

(a) (b)

Figure 5.6: *MR-guided kidney biopsy. (a) Planning of a double-oblique path for a kidney biopsy using a T2-weighted 3-D dataset. The trajectory (yellow line) is defined by selecting the entry and target points in any MPR plane. The MPRs can be automatically aligned along the planned path for trajectory review (as shown here). [Bret 12] (b) Needle placement under real-time MR guidance. Slices were automatically aligned along the planned needle path.*

Sclerotherapy - Johns Hopkins

Percutaneous sclerotherapy is currently the treatment of choice for low-flow vascular malformations. Typically, the lesions are percutaneously treated under US and X-ray fluoroscopy guidance. However, certain lesions cannot be treated using those modalities, e.g. lesions deep within the body, beneath scars or in bone. In addition, many patients require several treatments, some on a monthly basis, which would expose them to a high cumulative dose of ionizing radiation.

In the following case, four needles (Fig. 5.7) were placed for sclerotherapeutic treatment of a complex intra-peritoneal venous malformation involving the mesentery of a 40-year old woman with Klippel-Trénaunay syndrome. The patient had already undergone one successful sclerotherapy of some superficial portions of this lesion using standard US and X-ray fluoroscopic guidance, but subsequent attempts to treat the deeper lesions using these modalities had failed. The presented MR-guided treatment was performed under general anesthesia with the needle guidance prototype being displayed on a screen inside the MR scanner room (Fig. 5.8). All four needles were successfully placed into the venous malformation, and the therapeutic agent (gadolinium DTPA-doped 3% sodium tetradecyl sulfate) was administered without extravasation or complication. The total time related to needle placement was 16 minutes. The planning time for four needles was 4 minutes and the mean skin-to-target time was 76 $\pm$ 30 seconds, with a median path length of 103 mm (range, 84 - 122 mm).

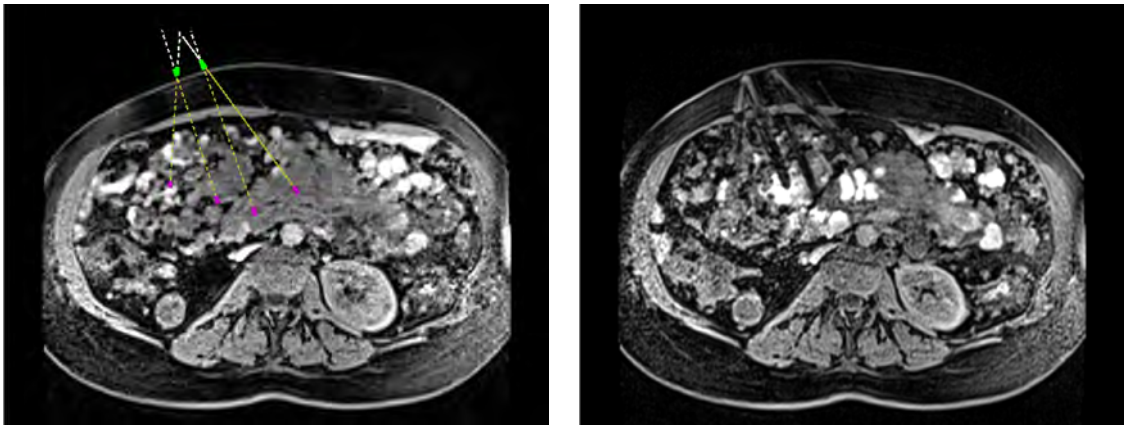

(a) (b)

Figure 5.7: *Comparison between (a) planned trajectories and (b) verification dataset after fourth needle placement. Needles were placed during free breathing. Areas of the venous malformation treated with gadolinium DTPA-doped 3 % sodium tetradecyl sulfate show enhancement in the image.*

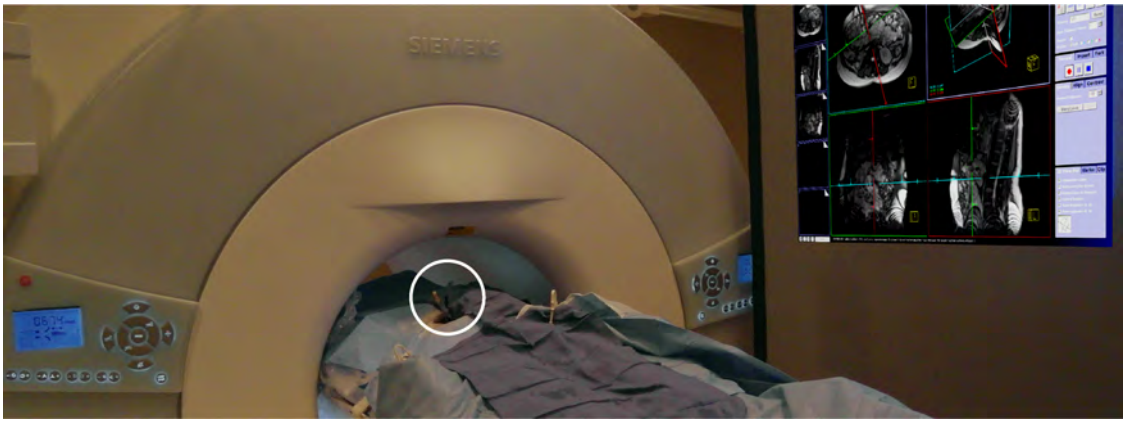

Figure 5.8: *Patient in the scanner with needle guidance user interface displayed on a screen inside the MR scanner room. All four needles (marked by circle) were successfully placed.*

Spinal Infiltration - Strasbourg

Selective nerve root infiltration with corticosteroids and anesthetics allows for an effective treatment of lumbosacral and sciatic pain [Sequ 02]. X-ray fluoroscopy and CT have been the imaging modalities of choice to guide these procedures due to their excellent bone-tissue contrast, high temporal resolution, and real-time imaging capabilities. However, many spinal infiltrations are performed in children or women of childbearing age, and often multiple therapy sessions are required. Thus, ionizing radiation should be avoided as much as possible. MRI allows to perform spinal infiltrations without ionizing radiation and provides superior tissue contrast. In an initial study, the developed needle guidance prototype was used for MR-guided needle placement in 10 cases. An example case is shown in (Fig. 5.9). As it can be seen from the reported times in Table 5.5, spinal infiltrations under MR guidance are relatively fast. Most time is needed for preparing both the patient and the equipment (e.g. pla-

(a) (b)

Figure 5.9: *MR-guided spinal infiltration. (a) Screen capture of real-time MR-guided needle placement with planned path overlaid. (b) Needle in place for injection of treatment agent. The needle guidance user interface is displayed on the movable in-room monitor (see arrow). The control elements of the magnet on the right side are covered by sterile foil to allow the interventionalist to move the patient table.*

cing sterile covers) ready for spinal needle placement (Fig. 5.9b). The average total procedure time was 27 min (range, 16-40 min) with an average targeting imaging time of 2:16 min (range, 0:22 - 4:37 min).

5.2.4 Discussion

The presented patient cases performed at multiple sites show the clinical value of the developed prototype for a spectrum of MR-guided percutaneous interventions. The procedure workflow is simplified by advanced planning capabilities, the image-guided entry point localization and automatic slice alignment along the planned path. The proposed slice layout allowed for safe and efficient needle placement also in difficult target locations. As summarized in Table 5.5, significant time was spent on non-imaging actions. Thus, one strategy to further decrease MR room time would be to prepare the patient on a second MR table outside the MR scanner room.

5.3 MR Thermometry

The purpose of this section is to provide an overview of the research performed with the developed framework for enhanced MR thermometry. Several thermal ablation studies using various energy sources from laser, RF, FUS to cryo have been performed within this project, see Figure 4.14 for screen captures. As MR thermometry during cryoablation is not well explored, an *in-vivo* study evaluated the use of MR thermometry during cryoablation with the results being presented in Section 5.3.1. Another study investigated the use MR thermometry for safety validation of an endorectal coil for ^{31}P spectroscopic imaging at 7 T (Sec. 5.3.2). The section closes by a study evaluating in patients both the temperature stability in prostate at 3 T and the clinical feasibility of the proposed integrated workflow for MR-guided thermal ablations.

5.3.1 Temperature Monitoring During Cryoablation

In contrast to heat-based ablation methods, cryoablation destroys tissue based on freezing [Gage 98, Erin 10]. For percutaneous cryoablation, thin probes are introduced under image guidance into the target structure. High-pressured argon gas is then circulated through the lumen of the probe. The rapid expansion of argon gas causes very low temperatures (Joule-Thompson effect) and thus creates an ice ball around the tip of the probe (Fig. 5.11). Each freezing cycle is followed by a passive or active (based on helium gas) thawing cycle. [Tatl 10] and [Morr 08] provide an overview of clinical applications.

Performing cryoablations under MR image guidance not only allows for accurate cryoprobe placement but also for real-time ice ball growth monitoring with an excellent contrast between ice ball and surrounding structures as illustrated in Figure 5.10. Temperature monitoring during cryoablation is currently based on discrete point measurements with temperature probes either built into the cryoprobe or additionally inserted. For increased procedural safety, it would be desirable to measure the temperature in close proximity all around the ice ball in order to avoid thermal injury to collateral structures. In the following section, a study [Roth 10b, Roth 11b]

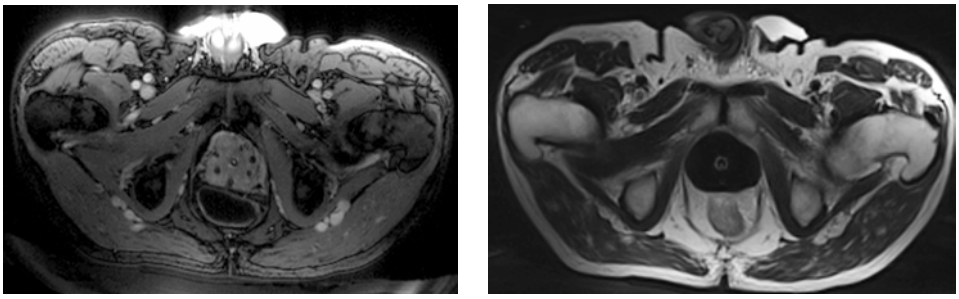

(a) Needles (six) in place (b) Ice ball covering prostate

Figure 5.10*: Cryoablation in prostate under MR image guidance. MR allows for (a) accurate real-time image-guided needle placed and (b) an excellent contrast between the frozen and unfrozen tissue. Images courtesy of Prof. Afshin Gangi.*

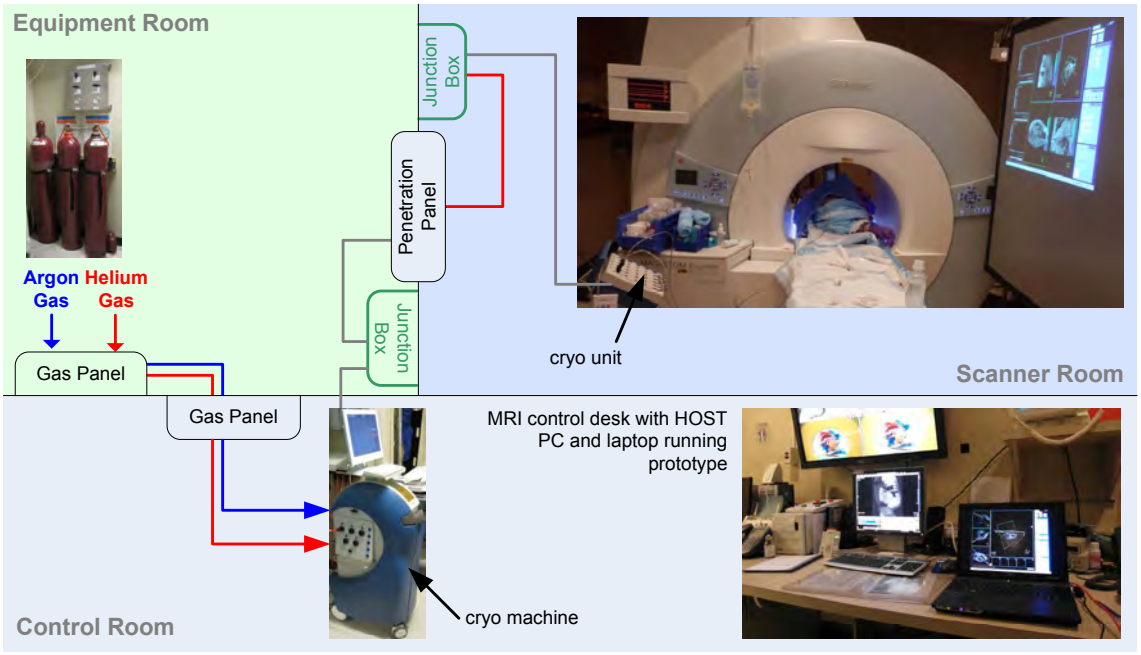

Figure 5.11: *Cryoablation system setup visualizing the flow of argon gas for freezing and helium gas for active thawing. The flow of gas is handled at the cryo machine in the control room and the cryoablation needles are connected to the cryo unit inside the scanner room. The display of the developed thermal therapy monitoring and guidance system is projected onto a screen next to the MR scanner.*

is introduced which explored the use of PRF shift thermometry for monitoring the temperature around the ice ball.

Study Setup

The following *in-vivo* swine experiments were approved by the institutional animal care and use committee. The experiments were performed on a 1.5 T MR scanner (Siemens MAGNETOM Espree). For signal reception, a 6-element body matrix coil was used in combination with 6 elements of the spine matrix coil.

The animals were pre-anesthetized, intubated, maintained on isoflurane, and positioned head-first, supine in the scanner. Cryoablation was performed in the kidney of four swine using an MR-compatible cryotherapy system from Galil Medical (Yokneam, Israel). Figure 5.11 shows the cryoablation system setup for this study.

Both cryoprobe (17 gauge IceRod, Galil Medical) placement and treatment monitoring were guided by MR imaging. Cryoablation was performed using a double freeze-thaw cycle (15 - 5 - 10 - 5 minutes) scheme. Ice ball formation and dissolution was monitored in one minute intervals under breath-hold conditions using a multiplanar PRF GRE sequence (5 msec TE, 51 msec TR, 25° flip angle, and a spatial resolution of $2.3 \times 2.3 \times 5$ mm). In two swines, a single cryoablation needle was used and in the other two swines, two needles were used in order to create a larger ablation zone and monitor the potential synergistic freezing effect of two adjacent probes. Following the procedure, the animals were immediately sacrificed, and the kidneys were harvested for histological evaluation (α-NADH staining for cell viability).

Selection of PRF Shift-based Thermometry Parameters

The temperature sensitivity of the PRF shift-based thermometry is maximized when TE equals T_{2*} [Yuan 12]. However, as shown in Section 2.4.2, needle artifacts grow with increasing TE. For a 17 gauge cryoablation probe, it was observed that the resulting needle artifact from PRF GRE imaging with an echo time of 20 msec (optimal TE) nearly covered the entire ice ball (Fig. 5.12). Therefore, a TE of 5 msec was chosen to allow for monitoring of the ice ball growth.

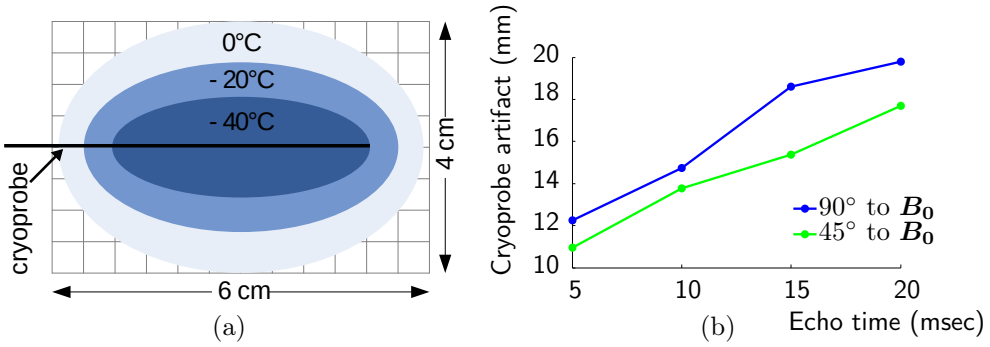

Figure 5.12: *Choosing the optimal echo time for PRF shift-based temperature monitoring during cryoablation using a 17 gauge IceRod (Galil Medical, Yokneam, Israel) cryoprobe. (a) Expected ice ball size according to the product specification. (b) Cryoablation needle artifact (mean diameter in mm) for different TEs at 45° and 90° with respect to* $\boldsymbol{B_0}$.

Results

The study showed that temperature measurements with the PRF shift method during cryoablation are strongly influenced by the ice ball-induced susceptibility artifact which increases with increasing ice ball size. The artifact is most pronounced perpendicular to the external magnetic field $\boldsymbol{B_0}$ (Fig. 5.13). Methods to efficiently calculate phase changes from estimated susceptibility distributions have been proposed [Koch 06, Kick 12]. However, those methods need further validation and so far no *in-vivo* results have been published for correcting the ice ball-induced susceptibility artifact.

The results further suggest that the PRF shift method can support ice ball shaping with multiple cryoprobes by predicting how the ice balls grow. This is important as the spacing between probes needed to adequately cover the target lesion is not fully understood and can vary significantly depending on tissue composition [Perm 07]. As demonstrated in Figure 5.14, cryoprobes separated by 2 cm did not create fully overlapping ice balls and thus no overlapping ablation zone. This was verified by the histological results. However, the PRF shift thermometry images even after 1 minute of freezing provided an early indication of the pattern of ice ball growth.

In addition, thermal injury to adjacent structures is a known complication of cryoablation, and suitable protection measures are essential [Gina 10, Tsou 11]. An example where thermal injury was induced in the abdominal wall adjacent to the kidney is shown in Figure 5.15. Here, the PRF shift thermometry images showed dissipation of cold towards the skin surface. Post-ablation T2-weighted TSE imaging

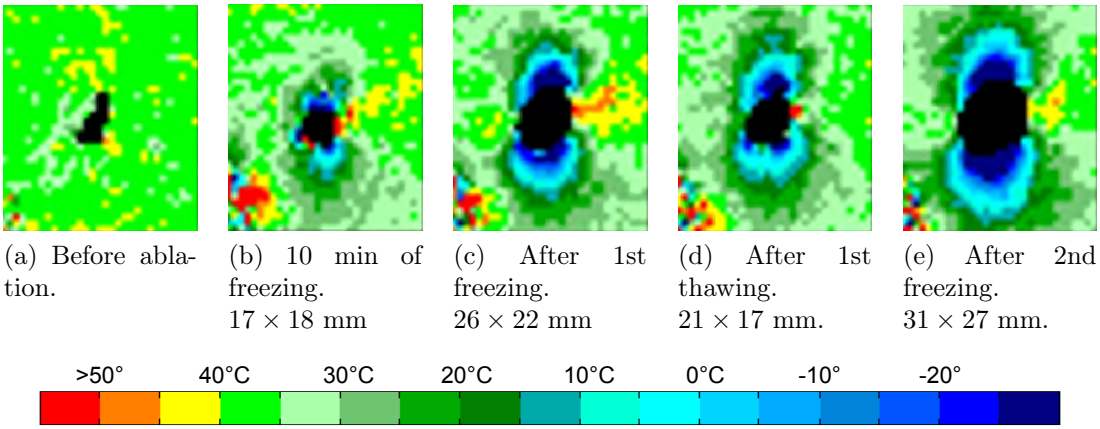

(a) Before ablation.
(b) 10 min of freezing. 17 × 18 mm
(c) After 1st freezing. 26 × 22 mm
(d) After 1st thawing. 21 × 17 mm.
(e) After 2nd freezing. 31 × 27 mm.

Figure 5.13: *Ice ball-induced susceptibility artifact and progression of ice ball growth through two freeze-thaw cycles. The susceptibility artifact is most pronounced perpendicularly to* $\boldsymbol{B_0}$ *and increases with growing ice ball size (given in second line). The signal void (black) in (a) corresponds to the needle artifact and to the artifact and ice ball in (b) - (e).*

(SPACE, 146 msec effective TE, 4303 msec TR, 0.4 × 0.4 × 0.8 mm spatial resolution) confirmed the ablation zone and thermal injury. This example demonstrates the potential of using PRF shift-based MR thermometry to monitor the effectiveness of protection mechanisms.

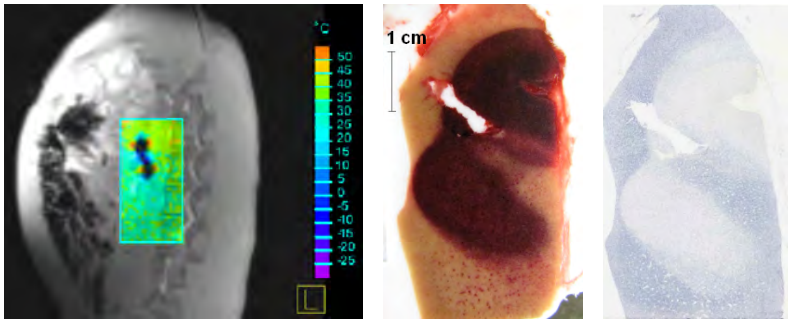

(a) (b) (c)

Figure 5.14: *Ice ball formation between multiple cryoprobes in porcine kidney. (a) Magnitude image with temperature overlay after 1 minute of freezing. Signal voids indicate the ice ball created by the two cryoprobes. Corresponding (b) unstained and (c)* α*-NADH stained tissue sample to assess cell viability (dark blue). The staining suggests a discontinuous cryoablation zone.*

Discussion

Accurate PRF shift-based temperature measurement in close proximity to the ice ball is difficult due to the induced susceptibility artifact which increases with increasing ice ball size. However, the results suggest that PRF shift-based MR thermometry can help optimize the spacing between multiple probes in order to create overlapping

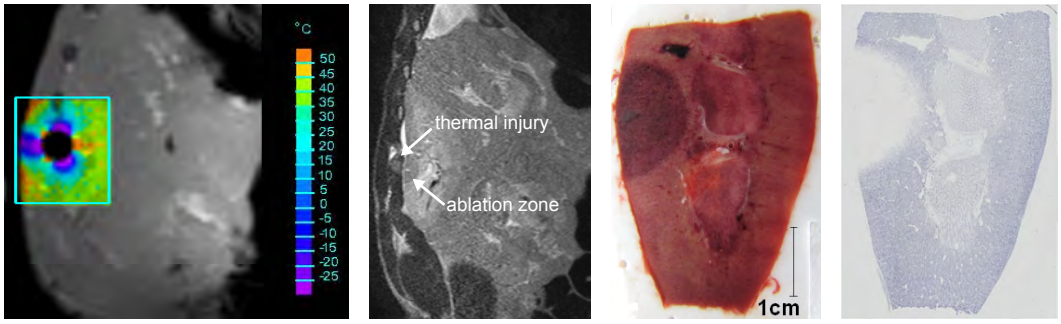

(a) (b) (c) (d)

Figure 5.15*: Thermal injury to collateral structure. (a) Magnitude image with overlaid temperature for a single cryoprobe placed adjacent to the kidney capsule. Dissipation of cold was measurable as it extended towards the abdominal wall. (b) Post-procedure T2w TSE imaging confirmed the ablation zone and thermal injury. Corresponding (c) unstained and (d) α-NADH stained tissue sample. The viability stain suggests extension of ablation zone beyond the kidney capsule.*

ablation zones. In addition, thermometry during cryoablation might help to avoid damage to collateral structures by monitoring if the protection mechanisms work.

However, as the PRF thermometry method is based on hydrogen bonding in liquid water, the PRF shift in frozen tissue differs and Eq. 4.6 cannot be applied for real-time MR thermometry inside the ice ball. Initial studies explored to use of MR parameters, such as signal intensity or $R2^*$ for temperature monitoring in frozen tissue [Wans 05]. To our knowledge, no *in-vivo* studies have been reported so far.

5.3.2 MR Thermometry for Verification of Coil Safety Validations

This section demonstrates that the developed MR thermometry methods can be used for applications beyond monitoring thermal ablations. A study is presented which uses MR thermometry to verify simulated RF field distributions for safety validation of a 7 T ^{31}P transmit/receive endorectal coil. Focus is put on the MR thermometry aspects and the interested reader is referred to [Kobu 12] for further details.

Motivation

The prostate-specific antigen (PSA) blood test is increasingly used for the early detection of prostate cancer. However, the specificity of the PSA test is very low leading to a large number of false positive results. Many of the detected lesions show benign pathology and could be left untreated. Thus, image-based methods are actively explored to improve the diagnosis and staging of prostate cancer. Currently, multiparametric MR imaging is the most sensitive and specific imaging method for that purpose [Scia 11]. In multi-parametric MRI, anatomic T2-weighted imaging is combined with MR spectroscopic imaging, diffusion weighted imaging (DWI), and dynamic contrast-enhanced MRI. MR spectroscopy allows for non-invasive measurement of the relative concentration of certain metabolites. Thus, it is applied to enhance the ana-

tomical and functional data of a suspected tumor region by metabolic information. For prostate cancer, studies explored the use of proton (^1H) MR spectroscopy for tumor/non-tumor tissue characterization [Sche 11] and it is anticipated that phosphorus (^{31}P) MR spectroscopy might further improve prostate cancer staging. However, ^{31}P has a lower gyromagnetic ratio, and thus Larmor frequency, than ^1H. It is also much less abundant in human tissue. This implies a high magnetic field strength is needed to achieve a reasonable spectral resolution within an acceptable measurement time (Sec. 2.1.1). However, the specific absorption rate (SAR) scales with approximately the square of the magnetic field strength. SAR quantifies the RF energy absorbed per unit of mass of an object in watts per kilogram (W/kg), i.e. it describes the potential tissue heating. It is given by

$$\mathrm{SAR} = \frac{\sigma E^2}{\rho}, \tag{5.4}$$

where σ defines the electric conductivity of the tissue, ρ the density, and E the strength of the electromagnetic field [Henn 11]. Staying within SAR limits is one of the most complex challenges for ultrahigh-field MR imaging [Mose 12] and requires the careful design and safety validation of dedicated coils.

Materials and Methods

Figure 5.16a shows the ^{31}P transmit/receive endorectal coil for which the safety validations were performed. MR thermometry was used to verify the points of highest SAR depositions identified by finite integration technique (FIT) simulations as described in [Kobu 12]. As the ^{31}P endorectal coil needs to be used in combination with a ^1H coil in order to map the metabolic information to anatomical locations, the RF-field distributions and corresponding SAR were evaluated for both the ^{31}P endorectal coil alone and in combination with an eight channel ^1H array coil.

For MR thermometry measurements, the ^{31}P endorectal coil was embedded into a gel phantom modeling the dielectric properties of abdominal human tissue. An MR magnitude image of the phantom is shown in Figure 5.16b. Phase images for temperature calculations were acquired before and after two minutes transmission of excessive RF power. A GRE sequence was used with three MR thermometry planes placed through the feed point and top of the coil (17 msec TE, 98 msec TR, 160 Hz/Px bandwidth, 25° flip angle, isotropic spatial resolution of 2 mm).

Safety validation of the ^{31}P endorectal coil: RF field distribution simulations were performed to determine the maximum input power at 120.3 MHz (Larmor frequency of ^{31}P at 7 T), which complies with SAR safety limits of maximum 10 g averaged SAR of 10 W/kg.

Safety validation of the combined setup: To investigate the combined operation of both coils FIT simulations were performed using an heterogeneous body model of a 70 kg male, combined with a model of the ^1H 8-channel array coil and a prostate model.

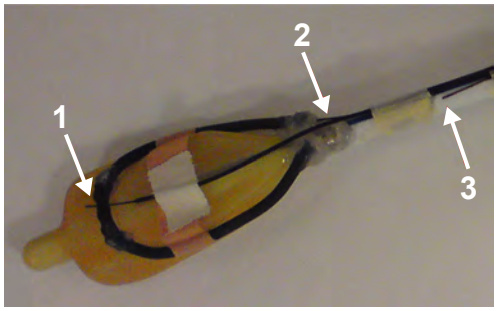

(a) ^{31}P endorectal coil for MR imaging at 7 T

(b) Gel phantom with embedded endorectal coil

Figure 5.16: *^{31}P transmit/receive endorectal coil for MR spectroscopy at 7 T. (a) ^{31}P transmit/receive endorectal coil built into mechanical housing of Medrad (Indianola (PA), USA) coil with fiber optic temperature probes fixed to the top of the coil (1), feed point (2), and coil wire (3). Image reproduced from [Kobu 12] with permission from John Wiley and Sons. (b) MR magnitude image of gel phantom with embedded endorectal coil used for MR thermoetry measurements to verify SAR simulations.*

Results

The RF simulations showed that a maximum RF input of 0.95 W for the endorectal coil and a maximum of 33 W for the combined setup can be used to stay within the SAR safety limits. Figures 5.17 and 5.18 show that there is good agreement between the simulated SAR distributions and measured MR temperature maps. It was further shown, that the presence of the ^{31}P endorectal coil had no influence on the SAR levels of the external 8-channel ^{1}H array coil (Fig. 5.18a). With the derived power setting for the ^{31}P endorectal coil an *in-vivo* experiment was performed which verified the compliance with SAR guidelines by the use of fiber optic temperature probes. The probes were fixed to the identified RF hot spots at the coil as illustrated in Figure 5.16b. See [Kobu 12] for further details on the *in-vivo* experiments.

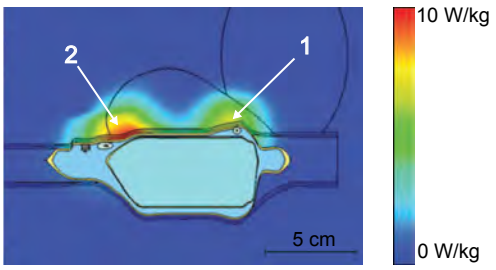

(a) Calculated SAR distribution

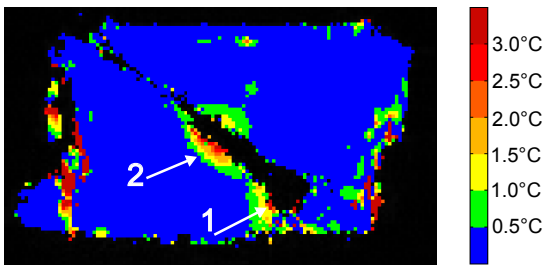

(b) MR temperature map

Figure 5.17: *Safety validation of the ^{31}P transmit/receive endorectal coil. The top of the coil (1) and feed point (2) were identified as locations of highest SAR depositions. (a) Calculated 10 g averaged SAR (W/kg) distribution at an RF input power of 0.95 W of the ^{31}P endorectal coil. Image reproduced from [Kobu 12] with permission from John Wiley and Sons. (b) MR temperature map after 2 minutes of extensive RF power transmission with the ^{31}P endorectal coil.*

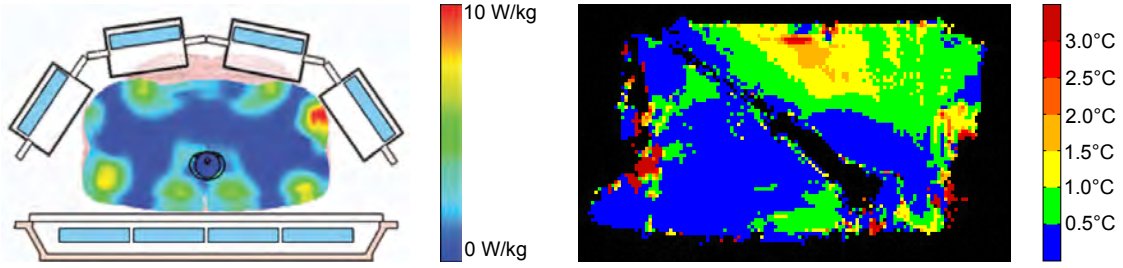

(a) Calculated SAR distribution (b) MR temperature map

Figure 5.18: *Safety validation of the combined setup. The presence of the ^{31}P endorectal coil had no influence on the SAR levels of the external 8-channel ^{1}H array coil. (a) Calculated 10 g averaged SAR (W/kg) distribution at an RF input power of 33 W of the ^{1}H array coil with the ^{31}P endorectal coil present. Image reproduced from [Kobu 12] with permission from John Wiley and Sons. (b) MR temperature map after 2 minutes of extensive RF power transmission.*

5.3.3 MR-guided Focal Therapy in Prostate

Minimally invasive focal therapy is emerging as an option between watchful waiting and radical whole gland therapy for the treatment of low and intermediate grade prostate cancer. [Ahme 08]. In the following sections, a pre-study for MR-guided transrectal prostate laser ablation at 3 T is presented [Bome 12, Bome]. The purpose of the study was two fold. The first goal was to evaluate in patients the temperature stability in prostate at 3 T using a fast GRE EPI sequence. The second goal was to evaluate the clinical feasibility and time efficiency of the integrated needle placement and real-time treatment monitoring workflow developed within this thesis.

Performing focal laser ablation in prostate under MR guidance is attractive for two reasons. First, MR imaging is currently the most sensitive and specific imaging technique for localizing prostate cancer [Scia 11]. Second, the ablation progress can be monitored with MR thermometry as the laser fiber does not cause any image distortion [Bozz 13]. The principle of laser ablation is to cause coagulation necrosis through high temperatures generated by the local absorption of laser energy. The laser light is delivered through thin and flexible fibers which are positioned in the tumor using fine-bore cannulas. The ablation volume is predominately determined by the extent of laser power which can be applied before charring at the fiber tip occurs.

Materials and Methods

Informed consent was waived by the Institutional Review Board. The study included 15 patients with suspicion for recurrent prostate cancer who were scheduled for MR-guided transrectal prostate biopsy on a 3 T MR scanner (Siemens MAGNETOM Trio). As illustrated in Figure 5.19, the patients were positioned prone on the MR scanner table and the DynaTrim biopsy device (Invivo, Gainesville (FL), USA) with an attached needle guide was inserted rectally. For signal reception, one 6-element phased array matrix coil was placed on the patient's back and one below the hips and pelvis. The contrast media filled needle sleeve (Fig. 5.19b) was well visible in T1-

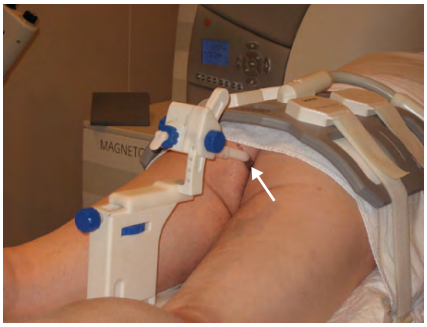

(a) Invivo DynaTrim biopsy device

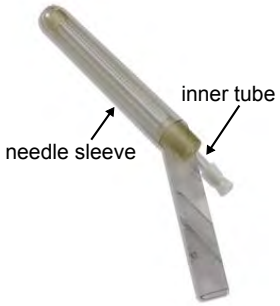

(b) MR-visible needle guide

Figure 5.19: *MR-guided transrectal prostate biopsy. (a) Patient in prone position with DynaTrim biopsy device (Invivo, Gainesville (FL), USA) and needle guide (see arrow) inserted rectally. Image reproduced from [Yaka 08] with permission from Wolters Kluwer Health. (b) shows the needle guide with the MR-visible needle sleeve filled with contrast media and the inner tube for biopsy needle or laser fiber insertion. Image reproduced from [Invi] with permission from Invivo.*

weighted MR images and the DynaTrim biopsy device was adjusted until the needle sleeve pointed towards the target, i.e. the cancer suspicious region. Following, the biopsy needle or laser fiber was inserted through the inner tube of the needle sleeve.

The MR-guided prostate biopsies were performed as described in [Yaka 08, Scho 12] with additional steps added for online MR thermometry as illustrated in Figure 5.20.

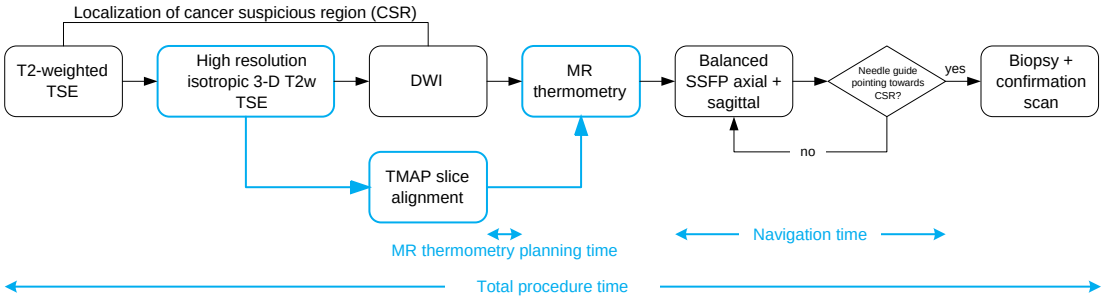

Figure 5.20: *Workflow diagram of MR-guided transrectal prostate biopsy with additional steps (in blue) added for online MR thermometry. The workflow for a laser ablation procedure would be very similar as instead of the biopsy needle a trocar for placing the laser fiber would be inserted. Procedure times recorded for evaluation of workflow efficiency are further indicated.*

For localization of the cancer suspicious region, T2-weighted TSE and DWI datasets were acquired. Between those two localization datasets an additional high resolution, isotropic, T2-weighted 3-D TSE dataset (102 msec effective TE, 1000 msec TR, spatial resolution of $1.0 \times 1.0 \times 1.0$ mm, acquisition time for 60 slices 2:36 min) was acquired for planning of the MR thermometry slices. Thus, the 3 minutes acquisition time of the DWI dataset was be used for planning of the MR thermometry image planes. The 3-D dataset was imported into the developed planning tool and the MR

thermometry image planes were planned along the MR-visible needle sleeve with the target point set to the cancer suspicious region (Fig. 5.21). After the DWI, the three real-time MR thermometry planes were automatically aligned along the planned laser fiber position as described in Section 3.2.4. This layout of thermometry planes allows for optimal spatial monitoring of the ablation progress in three orthogonal dimensions. Temperature was continuously measured for two minutes using a multi-slice GRE PRF EPI sequence (12.1 msec TE, 20 msec TR, 20° flip angle) with a frame rate of 1.95 seconds and a spatial resolution of $3.1 \times 3.0 \times 5.0$ mm. Two minutes is a realistic time for focal laser ablation in prostate [Wood 10]. After the thermometry step the biopsy was continued. The needle guide was adjusted using an in-and-out procedure, i.e. alternating imaging and manual DynaTrim adjustment outside the bore, until it was aligned with the cancer suspicious region. The biopsy was then taken and balanced SSFP confirmation scans were acquired in axial and sagittal directions.

For evaluation of time efficiency, procedure times were recorded as illustrated in Figure 5.20. The total procedure time was defined as the time from the first to the last MR image acquisition for the first cancer suspicious region, MR thermometry planning time as the time between the end of the DWI and the MR thermometry start, and navigation time as the time needed for needle guide positioning.

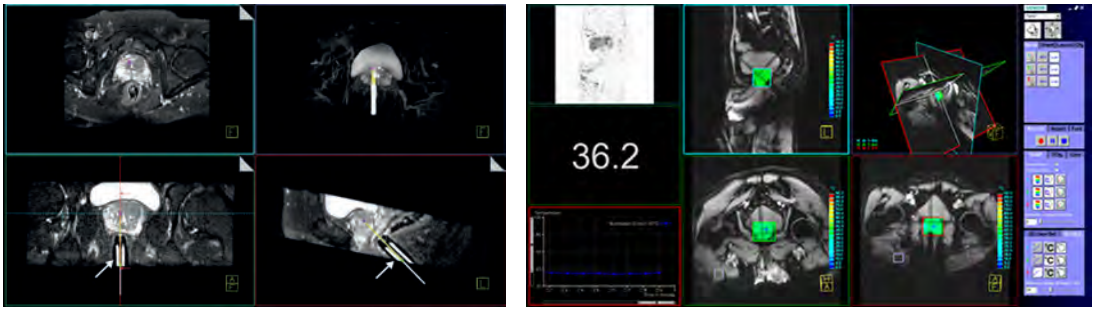

(a) Planning of MR thermometry planes (b) Monitoring of temperature stability

Figure 5.21: *MR thermometry for focal laser ablation in prostate. (a) Planning of MR thermometry planes along the MR-visible needle sleeve (see arrows) with the target point set to the cancer suspicious region. (b) The real-time MR thermometry slices are automatically aligned along the planned MR thermometry planes. Temperature stability was evaluated in the ROIs placed around the prostate.*

Results

The integrated needle placement and real-time treatment monitoring workflow was feasible in all 15 patients. The median total procedure time was 35 minutes (range, 29 - 46 min) with two biopsy samples taken from one cancer suspicious region in each patient. The median additional time needed for TMAP planning was 0:33 minutes (range, 0:05 - 2:23 min). The median needle guide navigation time was 8 minutes (range, 2:09 - 12:08 min). The temperature stability was evaluated for each patient in an ROI placed around the prostate as illustrated in Figure 5.22b. In two patients the prostate moved due to peristaltic motion and bladder filling. Figure 5.22 illustrates the effect of this motion on the temperature maps. The motion-corrupted temperature

maps were reliably detected by calculating the cross correlation for the ROI covering the prostate, details are provided in Table 5.6. Excluding those two patients whose prostate had moved, the mean temperature deviation from baseline temperature was 1.49 °C (range,0.67 °C - 2.32 °C) with $\boldsymbol{B_0}$ drift correction.

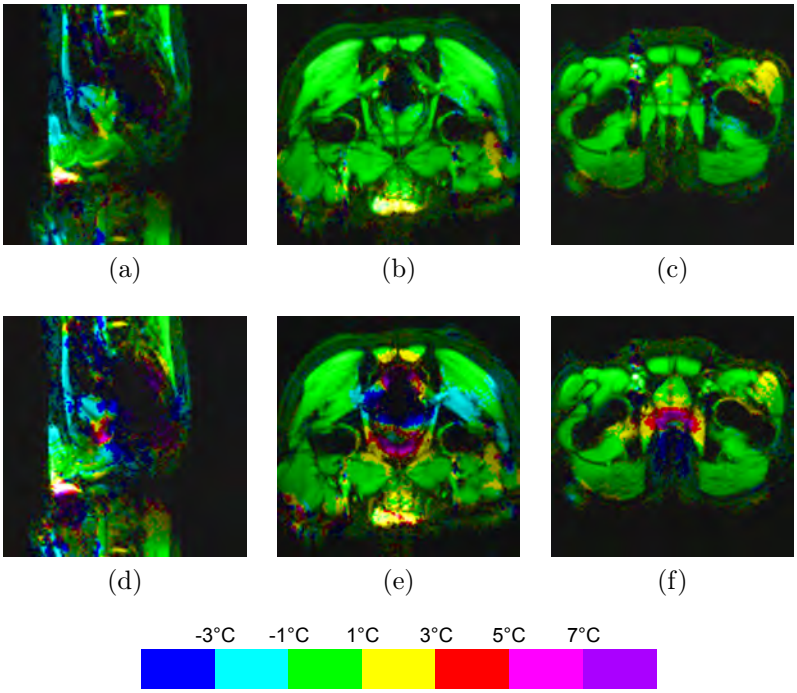

Figure 5.22: *Influence of motion on temperature maps. (a)-(c) Temperature images of patient 11 at time point 1 (cross correlation ROI = 0.996). (d)-(f) Temperature images at time point 3 (cross correlation ROI = 0.581) are corrupted due to prostate motion. The corresponding magnitude difference images can be found in Figure 4.4.*

Discussion

The integrated workflow for thermal applicator placement and real-time treatment monitoring was feasible to use in a clinical setup. The median procedure time of 35 minutes suggests that it is feasible to perform a focal prostate laser ablation in an hour as only additional time for post-ablation imaging would be needed. The high temperature stability is promising for accurate real-time treatment monitoring. It was further shown that prostate motion can be reliably detected by setting the ROI cross correlation threshold to 0.9. To minimize prostate motion due to bowel movement, and thus increase temperature stability, a peristaltic relaxing agent could be administered to decrease the tonus and motility of the intestines.

Table 5.6: *Temperature stability in prostate. Mean absolute temperature deviation (in °C) from baseline temperature over a 2 min PRF image acquisition period (20 measurements per slice). The number of data points depends on prostate size.*

Patient	Avg. temperature deviation	# Data points	Cross correlation[a]	
			ROI	Image
1	2.28	8,560	0.98	0.98
2	1.20	13,460	0.99	0.99
3	0.67	17,000	0.99	0.99
4	2.32	12,300	0.99	0.99
5	1.14	12,880	0.98	0.99
6	2.17	11,440	0.97	0.97
7	1.90	9,920	0.97	0.99
8	0.72	9,500	0.99	0.99
9	5.25	8,880	0.83	0.98
10	0.90	10,380	0.98	0.99
11	11.77	9,680	0.84	0.99
12	1.37	9,400	0.98	0.99
13	0.99	13,060	0.99	0.99
14	2.29	18,680	0.97	0.98
15	1.43	8,700	0.97	0.99
all[b]	**1.49 ± 0.62**	**155,280**		

[a] Cross correlation averaged over all three image planes.

[b] Not including patient 9 and 11 in which the prostate had moved.

5.4 Summary

The evaluation covers the entire imaging workflow for an MR-guided percutaneous procedure and examines the impact of the developed methods for real-time MR-guided needle placement and online MR thermometry. The extensive *in-vitro* and *in-vivo* clinical studies performed with the developed prototype emphasizes the relevance of the conducted research.

As targeting accuracy is essential for any percutaneous intervention, targeting accuracy and time of the proposed methods were extensively validated in phantom and animal studies. The influence of trajectory obliquity, level of experience of the interventionalist, and organ motion on targeting accuracy and time was analyzed.

For the phantom study, two expert interventionalists and two non-expert users performed 96 needle punctures in a gelatin phantom. All targets were successfully punctured with a mean skin-to-target time of 100 ± 50 seconds. Expert users were significantly faster than non-expert users for single-oblique but not for double-oblique

trajectories which emphasizes the ease of use of the developed system. The mean targeting error was 1.8 ± 1.5 mm (standard deviation) in all directions. No significant difference in targeting accuracy was found between non-expert and expert users and between single and double-oblique paths. Further, no interaction effect between level of expertise and trajectory obliquity on targeting accuracy could be shown.

The *in-vivo* study in two living pigs showed similar results. Fifty-five needle insertions were performed by an expert interventionalist, 20 in the paraspinal muscle and 35 in all segments of the kidney. During free breathing, the needles were inserted in a single advancement into the target point, 23 along single-oblique and 32 along double-oblique trajectories. All needles were successfully placed with a mean skin-to-target time of 113 ± 57 seconds. The mean targeting error was 2.9 ± 1.9 mm in all directions. No significant difference was found in targeting time between paraspinal and kidney insertions but between single and double-oblique trajectories.

The results of these validation studies show significant potential for the translation of the proposed methods into clinical practice. This is further emphasized by the results of 18 patient cases covering a wide range of procedures from MR-guided thermal ablation to targeted drug delivery. All patients were treated successfully with an average targeting time of 3 minutes for spinal infiltrations and around 5 minutes for abdominal procedures. This indicates that the developed methods allow for fast needle placement even in moving organs.

Besides needle guidance, the developed prototype was used for several studies exploring the use of MR thermometry for new applications from coil safety validation to MR thermometry during cryoablation and evaluating temperature stability for focal laser treatment in prostate.

The *in-vivo* study on MR thermometry during cryoablation showed that accurate PRF shift-based MR thermometry in close proximity to the ice ball is difficult due to the induced susceptibility artifact. However, online MR thermometry during cryoablation appears to be helpful in optimizing the spacing between multiple probes in order to create overlapping ablation zones.

The results from the study evaluating in patients both the temperature stability in prostate at 3 T and the clinical feasibility of the proposed integrated workflow for MR-guided thermal ablations are very promising. The median total procedure time was 35 minutes with only about 30 seconds needed for planning of the temperature monitoring slices. This further emphasizes the potential clinical value of the proposed automatic slice alignment algorithm. The temperature stability was evaluated for each patient in an ROI placed around the prostate. In two patients the prostate moved due to peristaltic motion and bladder filling which was reliable identified by the implemented motion detection strategies. Excluding those two patients, the mean temperature deviation from baseline temperature was 1.49 °C (range, 0.67 °C - 2.32 °C).

Summary and Conclusions 6

MRI offers several major advantages over other imaging modalities for guiding percutaneous interventions including superior soft-tissue contrast, real-time multi-planar imaging capabilities, and the ability to intra-procedurally monitor thermally-induced tissue alterations. In particular for pediatric patients or repeated and long procedures, the lack of ionizing radiation is a further key advantage. Even though interventional MRI is still in its early stages, the clinical potential has improved significantly with the introduction of wide-bore systems and near real-time, high resolution imaging sequences. This growth reflects in an increasing number of centers providing interventional MRI services. The interventional and surgical MRI market in the United States is estimated to increase with a compound annual growth rate of 3.7% until 2016 [Insi 12]. To promote the spread of MR-guided percutaneous interventions beyond tertiary care centers, the research efforts of this dissertation were focused on improving and simplifying the entire workflow of such procedures by image processing methods without introducing any additional equipment.

As accurate needle placement is essential for the success of both diagnostic (e.g. biopsies) and therapeutic procedures (e.g. thermal ablation or sclerotherapy), methods were developed which allow for safe and efficient device placement under real-time MR imaging. These methods cover the three main workflow steps planning, entry point localization, and real-time needle placement. As MR guidance is usually only applied if the procedure is not feasible under less expensive imaging modalities, special focus was put on complex target locations, i.e. locations requiring highly angulated approaches and non-axial scan planes, and procedures requiring the placement of several needles.

The presented algorithm on rapid entry point localization allows to rapidly, accurately and reproducibly localize the skin entry site using only the scanner's landmark laser and image processing methods which calculate the lateral offset based on the body contour derived from segmenting the image. Thus, the proposed technique can be performed on any clinical MR scanner without the need for additional entry point localization imaging. This promises reduced overall procedure time, in particular for complex procedures where multiple needles are placed. Combined with the implemented methods for trajectory planning, the proposed entry point localization method allows a "plan once, scrub once" procedure workflow. The interventionalist can accurately locate multiple entry sites before scrubbing the patient, and can then move quickly from one site to the next without needing to reidentify entry sites and trajectories for each needle placement.

The developed method for automatic slice alignment overcomes one of the main challenges in freehand MR-guided needle interventions. For procedure safety and efficiency it is essential to continuously visualize the entire needle, the target lesion, and the surrounding anatomy. However, slice alignment typically requires significant intraprocedure communication. This can be time consuming and confusing even for an experienced team. It is particularly challenging when complicated oblique or orthogonal image planes need to be prescribed. The presented algorithm automatically aligns three MR-slices: two along the planned trajectory and one orthogonal to it at the target. The slices are oriented with preference to the standard axial, coronal, and sagittal planes. Coincidentally, the intersection of the orthogonal slice planes generates a saturation band pattern in the other slices corresponding to the planned path and target location, respectively, which provides additional guidance during needle placement. Further, aliasing artifacts are minimized by optimally choosing the center of the imaging planes determined with respect to the planning dataset. The proposed slice layout is advantageous for real-time needle placement as the slices are oriented as closely as possible to the standard anatomical planes and the user can intuitively follow the slice saturation bands and knows the target is reached once a cross-sectional needle artifact appears in the orthogonal target slice.

The developed set of tools for precise needle positioning may have positive impact on thermal ablations as precise thermal applicator placement is key for ensuring complete ablation of disease tissue while sparing adjacent healthy tissue.

To further improve the safety and efficiency of thermal ablation procedures, a set of methods was developed that supports integration of MR thermometry into a clinical setting. The first step is to ensure straightforward positioning of thermal image planes to ensure coverage of the entire ablation zone. Thus, information about thermal applicator placement from the planning step is reused and fed into the automatic slice alignment algorithm. The reliability of online MR thermometry is then improved by the presented algorithms for automatic $\boldsymbol{B_0}$ drift correction and identification of motion-corrupted images. Furthermore, thermal data interpretation is simplified by fusing anatomical and thermal data based on the HLS color space. The proposed method allows for intuitive and consistent windowing of both anatomical and thermal data. Thus, anatomical structures which can cause heat sink effects, e.g. large vessels, are well visible in the combined magnitude/ thermal image. Areas of low signal, and thus unreliable thermal information, are effectively thresholded.

A major goal of this thesis was the translation of the developed methods into clinical practice. To allow for extensive validation, the proposed methods were implemented in a CE-labeled prototype which supports the entire MR-guided thermal ablation workflow from planning to applicator placement and real-time temperature monitoring. Currently, the prototype is used at more than 20 centers worldwide allowing for an extensive evaluation of the presented methods. The broad use of the developed prototype for both *in-vitro* and *in-vivo* clinical studies emphasizes the relevance and impact of the conducted research.

As targeting accuracy is essential for successful image-guided therapy, an extensive validation of targeting accuracy and time was performed in a phantom and animal study. Ninety-six targets were punctured in a custom-designed stiff gelatin phantom (rubber O-rings as targets and wooden beads as vital structures). The measured need-

le placement accuracy of 1.8 ± 1.5 mm (standard deviation) was significantly better than the numbers reported by others for the freehand approach. Even for double-oblique trajectories, the needle could be positioned within a 5 mm accuracy limit, even by non-expert users. The *in-vivo* animal studies showed similar results with a targeting accuracy of 3.0 ± 1.8 mm in all directions, with no significant difference based on trajectory obliquity or organ type (paraspinal or kidney punctures). Procedure safety and efficacy is further influenced by table time. By using the developed purely software-based approach that does not require any setup time, less than 30 minutes (from planning to verification) were needed to place five needles in the kidney or spinal muscle of pigs, i.e. on average 6 minutes per needle. This is significantly shorter than what has been previously reported for manual MR-guided percutaneous interventions. This is anticipated to facilitate more widespread adoption of MR guidance for these procedures beyond tertiary care centers.

Clinical translation of the developed methods was shown for a wide spectrum of percutaneous procedures at multiple centers. Needles were placed in patients for sclerotherapeutic treatment of venous malformations, RF ablation of liver lesions, spinal infiltrations for pain treatment, and biopsies of abdominal lesions. All patients were successfully treated with the needles safely and efficiently placed also into difficult target locations. The average targeting time of around 5 minutes for liver ablation and abdominal biopsies indicates that the developed methods allow for fast needle placement even in moving organs. Significant time was spent on non-imaging actions, which emphasizes the potential to further decrease procedure time by workflow improvements, such as in-room MR scanner control. The wide range of thermal applications performed with the developed framework further suggests that it may serve as a validation tool for researchers. Studies ranged from testing novel coils to exploring MR thermometry for cryoablation and evaluating temperature stability for focal laser treatment in the prostate. The integrated needle placement and real-time treatment monitoring workflow was feasible in all patients with a median total procedure time of 35 minutes. Temperature stability evaluation showed that motion-corrupted thermal images can be reliably detected with the proposed methods and a high temperature stability is feasible *in-vivo*. The mean deviation from baseline temperature was 1.49 °C.

The initial experience at multiple clinical sites suggests that the presented purely software-based methods simplify MR-guided percutaneous interventions and may reduce variability among interventionalists. Providing easy to use, affordable and effective MR guidance may have the potential to increase adoption of MR for image-guided minimally invasive percutaneous procedures, providing greater access also to patients in non-academic care centers where today such procedures are not often performed.

Acronyms

2-D	two-dimensional
3-D	three-dimensional
ANOVA	analysis of variance
CT	computed tomography
DICOM	digital imaging and communications in medicine
DWI	diffusion weighted imaging
EPI	echo planar imaging
FID	free induction decay
FIT	finite integration technique
FLASH	fast low-angle shot
FNA	fine-needle aspiration
FOV	field of view
L_{re}	field of view along the readout direction
L_{ph}	field of view along the phase encoding direction
FUS	focused ultrasound
GRAPPA	generalized autocalibrating partially parallel acquisition
GRE	gradient echo
HLS	hue lightness saturation
IFE	Interactive Front End
iMRI	interventional MRI
LITT	laser induced thermal therapy
MIP	maximum intensity projection

MPR	multi-planar reformatting
MR	magnetic resonance
MRI	magnetic resonance imaging
PCS	patient-centered coordinate system
PRF	proton resonance frequency
PSA	prostate-specific antigen
RF	radiofrequency
RFA	RF thermal ablation
ROI	region of interest
SAR	specific absorption rate
SNR	signal-to-noise ratio
SPACE	sampling perfection with application optimized contrasts using different flip angle evolutions
SSFP	steady-state free precession
TE	echo time
TR	repetition time
TSE	turbo spin echo
UI	user interface
US	ultrasound
VIBE	volumetric interpolated breath-hold examination
XIP	eXtensible Imaging Platform

List of Symbols

Chapter 2

$\boldsymbol{M}$	Net magnetization	11
$\boldsymbol{B_0}$	External homogeneous magnetic field	11
$\|\boldsymbol{B_0}\|_2$	Magnitude of the $\boldsymbol{B_0}$ measured in Tesla	12
ω_0	Resonance frequency, the so-called Larmor frequency	12
γ	Gyromagnetic ratio of the observed nucleus	12
$n\uparrow$	Number of protons in the upper energy level	12
$n\downarrow$	Number of protons in the lower energy level	12
ΔE	Energy difference between the upper and lower spin states	12
$\hbar$	Planck's constant	12
k	Boltzmann's constant	12
T	Absolute temperature in Kelvin	12
χ	Magnetic susceptibility	13
$\boldsymbol{M_z}$	Longitudinal magnetization	13
$\boldsymbol{M_{xy}}$	Transverse magnetization	13
$\boldsymbol{T_1}$	Time required for $\boldsymbol{M_z}$ to recover to $\sim 63\%$ of its final value	13
$\boldsymbol{T_2}$	Time required for $\boldsymbol{M_{xy}}$ to decline to $\sim 37\%$ of its initial value	13
$\boldsymbol{T_{2^*}}$	Decay of FID	14
$\boldsymbol{B}$	Local magnetic field	14
$\boldsymbol{r}$	Position in the magnetic field	14
$\omega(\boldsymbol{r})$	Local Larmor frequency at position $\boldsymbol{r}$	14
G_{ss}	Slice selection gradient	15
ω_{RF}	Center frequency of RF pulse	15
$\Delta\omega_{RF}$	Bandwidth of RF pulse	15
Δz	Slice thickness	15
G_{re}	Gradient along the readout direction	15
Φ_{re}	Spatially dependent phase along the readout direction	15
G_{ph}	Phase encoding gradient	16
T_{ph}	Duration of phase encoding gradient	16
Φ_{ph}	Spatially dependent phase along the phase encoding direction	16
S	MR signal-induced in the receiver coil	17
N_{re}	Number of readout time points during one phase encoding step	17
N_{ph}	Number of phase encoding steps	18

$I(u,v)$	Signal intensity at voxel (u,v)	18
$\|\|I(u,v)\|\|$	Magnitude of the measured MR signal at voxel (u,v)	18
$\Phi(I(u,v))$	Phase of the measured MR signal at voxel (u,v)	18
L_{re}	FOV along the readout direction	19
ν	Receiver bandwidth	19
T_{acq}	Duration of data acquisition	19
Δt	Signal sampling time	19
L_{ph}	FOV along the phase encoding direction	19

Chapter 3

x, y, z	Coordinates $\in \mathbb{R}^3$ of a point in the PCS	36
$\boldsymbol{r}, \boldsymbol{c}, \boldsymbol{n}$	Row, column, and normal unit vectors spanning the image plane	36
$\boldsymbol{t}$	Distance of image plane from origin of PCS	36
Δc,Δr	Column/ row pixel resolution	36
M	Number of columns	41
N	Number of rows	41
$\boldsymbol{p}_{\mathrm{e}}$	Coordinates $\in \mathbb{R}^3$ of entry point	34
$\hat{\boldsymbol{p}}_{\mathrm{e}}$	Image coordinates $\in \mathbb{R}^2$ of entry point	36
$\boldsymbol{p}_{\mathrm{t}}$	Coordinates $\in \mathbb{R}^3$ of target point	34
$\boldsymbol{p}_{\mathrm{l}}$	Coordinates $\in \mathbb{R}^3$ of point marked by laser crosshair on patient	37
$\hat{\boldsymbol{p}}_{\mathrm{l}}$	Image coordinates $\in \mathbb{R}^2$ corresponding to $\boldsymbol{p}_{\mathrm{l}}$	37
t_{move}	Table movement for superior-inferior entry point localization	37
$t_{\mathrm{curr\ pos}}$	Current table position	37
$d_{\mathrm{iso\ laser}}$	Distance between laser light and isocenter of magnet	37
$d_{\mathrm{l,r}}$	Left-right offset for lateral entry point localization	37
$I(u,v)$	Image with $u \in [0, M[$ and $v \in [0, N[$, and grey values of $[0, 4095]$	37
T	Threshold for object/background segmentation	37
T_{opt}	Minimum error threshold	37
g	Grey values in the range $[0, 4095]$	37
h	Histogram	37
i	Classes, $i = 1$ for background and $i = 2$ for object	37
μ	Mean value	37
σ	Standard deviation	37
P	A priori probability	37
e	Probability of correct grey level assignment	37
$B(u,v)$	Binary image with $u \in [0, M[$ and $v \in [0, N[$	39
θ	Threshold	41
$E(u,v)$	Edge image with $u \in [0, M[$ and $v \in [0, N[$	41
C	Set of contour pixels	41

$\boldsymbol{t}_\mathrm{p}$	Planned trajectory	43
z_s	Center of image slice $s \in 1, 2, 3$	45
z_v	Center of planning volume	45
$G_t(u, v)$	Exponential running average background image at time t	46
α	Learning rate $\in [0, 1]$	46
$\mathcal{R}$	Candidate region	47
$K(\mathcal{R})$	Circularity of a region	47
$A(\mathcal{R})$	Area of a region	47
Pe	Perimeter	47
n_e	Number of even Freeman chain codes	47
n_o	Number of odd Freeman chain codes	47
$\hat{\boldsymbol{p}}_\mathrm{c}$	Image coordinates $\in \mathbb{R}^2$ of a region's centroid	47
$\boldsymbol{p}_\mathrm{c}$	Coordinates $\in \mathbb{R}^3$ of a region's centroid	47
$d_{\boldsymbol{p}_\mathrm{c}, \boldsymbol{t}_\mathrm{p}}$	Distance of a region to the planned trajectory	47
Γ	Projection of $\boldsymbol{p}_\mathrm{c}$ onto $\boldsymbol{t}_\mathrm{p}$	47
$\boldsymbol{p}_\mathrm{es}$	Entry point moved along the direction of the planned path	50
$\boldsymbol{p}_\mathrm{tl}$	Left point of ROI for needle artifact detection	50
$\boldsymbol{p}_\mathrm{tr}$	Right point of ROI for needle artifact detection	50
$\boldsymbol{p}_\mathrm{n}$	Image plane normal $\in \mathbb{R}^3$	50
$R(\gamma)$	Rotation matrix to derive $\boldsymbol{p}_\mathrm{tl}$ and $\boldsymbol{p}_\mathrm{tr}$	50
$T_{\boldsymbol{p}_\mathrm{t}}$	Transformation matrix moving $\boldsymbol{p}_\mathrm{t}$ to the origin	50
T_xz	Transformation matrix rotating $\boldsymbol{p}_\mathrm{t}$ about the z-axis to the xz-plane	50
T_z	Transformation matrix rotating $\boldsymbol{p}_\mathrm{t}$ in the xz-plane to the z-axis	50
R_z	Rotation matrix rotating $\boldsymbol{p}_\mathrm{t}$ by γ around the z-axis	50
m	Slope	52
b	Intercept	52
A	Hough accumulator array	52
ρ	Normal from the origin to the line	52
θ	Angle of the line's normal with respect to the x-axis	52
l_{opt}	Optimal straight line	52

Chapter 4

$\boldsymbol{B}$	Local magnetic field	57
$\boldsymbol{B_0}$	External homogeneous magnetic field	57
σ	Nuclear shielding constant	57
σ_0	Temperature independent contribution to σ	57
σ_T	Temperature dependent contribution to σ	57
α	Temperature coefficient varying with -0.01 ppm/°C	58
$\omega(T)$	Proton resonance frequency at temperature T	58
γ	Gyromagnetic ratio of the observed nucleus	58

T_0	Baseline temperature	58
$\Delta T(u,v)$	Temperature change compared to T_0 at voxel (u,v)	58
$\Phi_t(u,v)$	Phase at time t and voxel (u,v)	58
$\Phi_0(u,v)$	Baseline phase at voxel (u,v)	58
TE	Echo time in msec	58
P	Cross-correlation coefficient	61
M	Number of columns	61
N	Number of rows	61
I_0	Magnitude baseline image	61
I_t	Magnitude image at time t during the procedure	61
$\overline{I_b}$	Mean gray value of the baseline image	61
$\overline{I_t}$	Mean gray value of the magnitude image	61
$D(u,v)$	Difference magnitude image	62
s	User defined scaling factor for $D(u,v)$	62
μ_d	Mean phase drift	62
θ_d	Threshold for $\boldsymbol{B_0}$ drift correction	63
$\Phi_{t_{corr}}(u,v)$	Phase at time t and voxel (u,v) corrected for $\boldsymbol{B_0}$ drift	63
c	Center for windowing	67
w	Width for windowing	67
g_i	12-bit input gray value	67
g_o	8-bit output gray value	67

List of Figures

List of Tables

Bibliography

[Ahme 08] H. Ahmed and M. Emberton. "Active surveillance and radical therapy in prostate cancer: can focal therapy offer the middle way?". *World Journal of Urology*, Vol. 26, No. 5, pp. 457–467, 2008.

[Ahme 11] M. Ahmed, C. L. Brace, F. T. Lee, and S. N. Goldberg. "Principles of and Advances in Percutaneous Ablation". *Radiology*, Vol. 258, No. 2, pp. 351–369, 2011.

[Ahra 11] K. Ahrar and R. Stafford. "Magnetic resonance imaging-guided laser ablation of bone tumors". *Techniques in Vascular and Interventional Radiology*, Vol. 14, No. 3, pp. 177–182, 2011.

[Arep 08] A. Arepally. "Targeted drug delivery under MRI guidance". *Journal of Magnetic Resonance Imaging*, Vol. 27, No. 2, pp. 292–298, 2008.

[Barb 11] I. Barbash, C. Saikus, K. Ratnayaka, A. Faranesh, O. Kocaturk, J. Bell, V. Wu, W. Schenke, M. Slack, and R. Lederman. "Real-time MRI guided percutaneous transthoracic left ventricular access and closure". *Journal of Cardiovascular Magnetic Resonance*, Vol. 13, No. Suppl 1, pp. 1–2, 2011.

[Baze 04] C. M. de Bazelaire, G. D. Duhamel, N. M. Rofsky, and D. C. Alsop. "MR imaging relaxation times of abdominal and pelvic tissues measured in vivo at 3.0 T: preliminary results". *Radiology*, Vol. 230, No. 3, pp. 652–659, 2004.

[Bela 07] M. Beland, P. Mueller, and D. Gervais. "Thermal ablation in interventional oncology". *Seminars in Roentgenology*, Vol. 42, No. 3, pp. 175–190, 2007.

[Bern 04] M. Bernstein, K. King, and X. Zhou. *Handbook of MRI pulse sequences*. Academic Press, 2004.

[Bern 06] M. A. Bernstein, J. Huston, and H. A. Ward. "Imaging artifacts at 3.0 T". *Journal of Magnetic Resonance Imaging*, Vol. 24, No. 4, pp. 735–746, 2006.

[Beye 05] D. Beyersdorff, A. Winkel, B. Hamm, S. Lenk, S. Loening, and M. Taupitz. "MR Imaging-guided prostate biopsy with a closed MR unit at 1.5 T: initial results". *Radiology*, Vol. 234, No. 2, pp. 576–581, 2005.

[Bock 91] A. Böcking. "Cytological vs histological evaluation of percutaneous biopsies". *Cardiovascular and Interventional Radiology*, Vol. 14, No. 1, pp. 5–12, 1991.

[Boll 04] D. Boll, E. Merkle, and J. Lewin. "Low-flow vascular malformations: MR-guided percutaneous sclerotherapy in qualitative and quantitative assessment of therapy and outcome". *Radiology*, Vol. 233, No. 2, pp. 376–384, 2004.

[Bome] J. Bomers, E. Rothgang, J. Roland, J. Barentsz, and J. Fütterer. "MR-guided temperature mapping in prostate cancer patients: stability and feasibility". *[In Submission]*.

[Bome 12] J. Bomers, E. Rothgang, J. Roland, J. Barentsz, and J. Fütterer. "MR-guided temperature mapping in prostate cancer patients: stability and feasibility". In: *Proceedings, 9th Interventional MRI Symposium*, pp. 39–42, Boston (MA), USA, Sep 2012.

[Bott 82] P. Bottomley, W. Edelstein, W. Leue, H. Hart, J. Schenck, and R. Redington. "Head and body imaging by hydrogen nuclear magnetic resonance". *Magnetic Resonance Imaging*, Vol. 1, No. 2, pp. 69–74, 1982.

[Bozz 13] G. Bozzini, P. Colin, P. Nevoux, A. Villers, S. Mordon, and N. Betrouni. "Focal therapy of prostate cancer: energies and procedures". *Urologic Oncology: Seminars and Original Investigations*, Vol. 31, No. 2, pp. 155–167, 2013.

[Bret 12] E. Breton, E. Rothgang, L. Pan, J. Garnon, G. Tsoumakidou, X. Buy, C. Lorenz, M. de Mathelin, and A. Gangi. "Spinal infiltrations and biopsies using an advanced real-time MR guidance approach: preliminary clinical report". In: *Proceedings, 20th Annual Meeting, International Society of Magnetic Resonance in Medicine*, p. 212, Melbourne, Australia, May 2012.

[Buss 10] H. Busse, N. Garnov, G. Thörmer, D. Zajonz, W. Gründer, T. Kahn, and M. Moche. "Flexible add-on solution for MR image-guided interventions in a closed-bore scanner environment". *Magnetic Resonance in Medicine*, Vol. 64, No. 3, pp. 922–928, 2010.

[Buss 12] H. Busse, N. Garnov, G. Thörmer, T. Kahn, and M. Moche. "Impact of an advanced patient registration on the experimental targeting accuracy of percutaneous MRI interventions guided by a clinical navigation system". In: *Proceedings, 20th Annual Meeting, International Society of Magnetic Resonance in Medicine*, p. 1586, Melbourne, Australia, May 2012.

[Carp 11] A. Carpentier, R. J. McNichols, R. J. Stafford, J.-P. Guichard, D. Reizine, S. Delaloge, E. Vicaut, D. Payen, A. Gowda, and B. George. "Laser thermal therapy: Real-time MRI-guided and computer-controlled procedures for metastatic brain tumors". *Lasers in surgery and medicine*, Vol. 43, No. 10, pp. 943–950, 2011.

[Chal 01] G. Chaljub, L. Kramer, R. Johnson, H. Singh, and W. Crow. "Projectile cylinder accidents resulting from the presence of ferromagnetic nitrous oxide or oxygen tanks in the MR suite". *American Journal of Roentgenology*, Vol. 177, No. 1, pp. 27–30, 2001.

[Chri 07] E. Christoforou, E. Akbudak, A. Ozcan, M. Karanikolas, and N. Tsekos. "Performance of interventions with manipulator-driven real-time MR guidance: implementation and initial in vitro tests". *Magnetic Resonance Imaging*, Vol. 25, No. 1, pp. 69–77, 2007.

[Das 10] C. Das, A. Goenka, and D. Srivastava. "MR-guided abdominal biopsy using a 1.5-Tesla closed system: a feasibility study". *Abdominal Imaging*, Vol. 35, No. 2, pp. 218–223, 2010.

[De O 08] A. De Oliveira, J. Rauschenberg, D. Beyersdorff, W. Semmler, and M. Bock. "Automatic passive tracking of an endorectal prostate biopsy device using phase-only cross-correlation". *Magnetic Resonance in Medicine*, Vol. 59, No. 5, pp. 1043–1050, 2008.

[De P 94] J. De Poorter, C. Dewagter, Y. Dedeene, C. Thomsen, F. Stahlberg, and E. Achten. "The proton-resonance-frequency-shift method compared with molecular diffusion for quantitative measurement of two-dimensional time-dependent temperature distribution in a phantom". *Journal of Magnetic Resonance, Series B*, Vol. 103, No. 3, pp. 234–241, 1994.

[Deng 09] J. Deng, S. Virmani, G. Yang, R. Tang, G. Woloschak, O. R.A., and L. A.C. "Intraprocedural diffusion-weighted PROPELLER MRI to guide percutaneous biopsy needle placement within rabbit VX2 liver tumors.". *Journal of Magnetic Resonance Imaging*, Vol. 30, No. 2, pp. 366–373, 2009.

[Deni 05] B. Denis de Senneville, B. Quesson, and C. Moonen. "Magnetic resonance temperature imaging". *International Journal of Hyperthermia*, Vol. 21, No. 6, pp. 515–531, Sep. 2005.

[Dera 05] J. Derakhshan and J. Duerk. "Update to pulse sequences for interventional MR imaging.". *Magnetic Resonance Imaging Clinics of North America*, Vol. 13, No. 3, pp. 415–429, 2005.

[Digi 09] *Digital Imaging and Communications in Medicine (DICOM), Part 3: Information Object Definitions*. National Electrical Manufacturers Association, 2009.

[Duda 72] R. Duda and P. Hart. "Use of the Hough transformation to detect lines and curves in pictures". *Communications of the ACM*, Vol. 15, No. 1, pp. 11–15, 1972.

[Dumo 93] C. Dumoulin, S. Souza, and R. Darrow. "Real-time position monitoring of invasive devices using magnetic resonance". *Magnetic Resonance in Medicine*, Vol. 29, No. 3, pp. 411–415, 1993.

[El S 06] A. M. El-Sharkawy, M. Schär, P. A. Bottomley, and E. Atalar. "Monitoring and correcting spatio-temporal variations of the MR scanner's static magnetic field". *Magnetic Resonance Materials in Physics, Biology and Medicine*, Vol. 19, No. 5, pp. 223–236, 2006.

[Elha 08] H. Elhawary, Z. Tse, A. Hamed, M. Rea, B. Davies, and M. Lamperth. "The case for MR-compatible robotics: a review of the state of the art". *The International Journal of Medical Robotics and Computer Assisted Surgery*, Vol. 4, No. 2, pp. 105–113, 2008.

[Erin 10] J. Erinjeri and T. Clark. "Cryoablation: Mechanism of Action and Devices". *Journal of Vascular and Interventional Radiology*, Vol. 21, No. 8, pp. S187–S191, 2010.

[Fisc 07a] G. Fischer, A. Deguet, C. Csoma, R. Taylor, L. Fayad, J. Carrino, S. Zinreich, and G. Fichtinger. "MRI image overlay: application to arthrography needle insertion". *Computer Aided Surgery*, Vol. 12, No. 1, pp. 2–14, 2007.

[Fisc 07b] G. Fischer, E. Dyer, C. Csoma, A. Deguet, and G. Fichtinger. "Validation system of MR image overlay and other needle insertion techniques". *Studies in Health Technology and Informatics*, Vol. 125, pp. 130–135, 2007.

[Fisc 11] F. Fischbach, J. Bunke, M. Thormann, G. Gaffke, K. Jungnickel, J. Smink, and J. Ricke. "MR-guided freehand biopsy of liver lesions with fast continuous imaging using a 1.0-T open MRI scanner: experience in 50 patients". *Cardiovascular and Interventional Radiology*, Vol. 34, No. 1, pp. 188–192, 2011.

[Free 61] H. Freeman. "On the encoding of arbitrary geometric configurations". *Electronic Computers, IRE Transactions on*, Vol. EC-10, No. 2, pp. 260–268, 1961.

[Frit 08] J. Fritz, J. Henes, C. Thomas, S. Clasen, M. Fenchel, C. Claussen, J. Lewin, and P. Pereira. "Diagnostic and interventional MRI of the sacroiliac joints using a 1.5-T open-bore magnet: a one-stop-shopping approach". *American Journal of Roentgenology*, Vol. 191, No. 6, pp. 1717–1724, 2008.

[Frit 09] J. Fritz, C. Thomas, S. Clasen, C. Claussen, J. Lewin, and P. Pereira. "Freehand real-time MRI guided lumbar spinal injection procedures at 1.5 T: feasibility, accuracy, and safety". *American Journal of Roentgenology*, Vol. 193, No. 4, pp. W161–W167, 2009.

[Frit 12] J. Fritz, U. Paweena, T. Ungi, A. Flammang, N. Cho, G. Fichtinger, I. Iordachita, J. Carrino, *et al.* "Augmented Reality Visualization With Image Overlay for MRI-Guided Intervention: Accuracy for Lumbar Spinal Procedures With a 1.5-T MRI System". *American Journal of Roentgenology*, Vol. 198, No. 3, pp. W266–W273, 2012.

[Gage 98] A. Gage and J. Baust. "Mechanisms of Tissue Injury in Cryosurgery". *Cryobiology*, Vol. 37, No. 3, pp. 171–186, 1998.

[Gena 02] J. Genant, J. Vandevenne, A. Bergman, C. Beaulieu, S. Kee, A. Norbash, and P. Lang. "Interventional musculoskeletal procedures performed by using MR imaging guidance with a vertically open MR unit: assessment of techniques and applicability". *Radiology*, Vol. 223, No. 1, pp. 127–136, 2002.

[Geor 10] A. George, J. Derbyshire, H. Saybasili, C. Saikus, O. Kocaturk, M. Guttman, E. McVeigh, R. Lederman, and A. Faranesh. "Visualization of active devices and automatic slice repositioning ("SnapTo") for MRI-guided interventions". *Magnetic Resonance in Medicine*, Vol. 63, No. 4, pp. 1070–1079, 2010.

[Gina 10] D. Ginat and W. Saad. "Bowel Displacement and Protection Techniques During Percutaneous Renal Tumor Thermal Ablation". *Techniques in Vascular and Interventional Radiology*, Vol. 13, No. 2, pp. 66–74, 2010.

[Gris 02] M. Griswold, P. Jakob, R. Heidemann, M. Nittka, V. Jellus, J. Wang, B. Kiefer, and A. Haase. "Generalized autocalibrating partially parallel acquisitions (GRAPPA)". *Magnetic Resonance in Medicine*, Vol. 47, No. 6, pp. 1202–1210, 2002.

[Gris 10] W. A. Grissom, M. Lustig, A. B. Holbrook, V. Rieke, J. M. Pauly, and K. Butts-Pauly. "Reweighted l1 referenceless PRF shift thermometry". *Magnetic Resonance in Medicine*, Vol. 64, No. 4, pp. 1068–1077, 2010.

[Gttl 10] F. Güttler, J. Rump, U. Teichgräber, C. Seebauer, P. Krauß, and B. Hamm. "Automatic scan plane adjustment in intraoperative MRI: let the image follow the instrument - preliminary results". In: *Proceedings, 8th Interventional MRI Symposium*, pp. 297–298, Baltimore (MD), USA, September 2010.

[Gupt 07] S. Gupta and D. Madoff. "Image-guided percutaneous needle biopsy in cancer diagnosis and staging". *Techniques in Vascular and Interventional Radiology*, Vol. 10, No. 2, pp. 88–101, 2007.

[Haac 99] E. Haacke, R. Brown, M. Thompson, and R. Venkatesan. *Magnetic Resonance Imaging: Physical Principles and Sequence Design*. John Wiley & Sons, 1999.

[Haas 86] A. Haase, J. Frahm, D. Matthaei, W. Hanicke, and K. Merboldt. "FLASH imaging. Rapid NMR imaging using low flip-angle pulses". *Journal of Magnetic Resonance*, Vol. 67, No. 2, pp. 258–266, 1986.

[Hemp 03] E. Hempel, H. Fischer, L. Gumb, T. Höhn, H. Krause, U. Voges, H. Breitwieser, B. Gutmann, J. Durke, M. Bock, *et al.* "An MRI-compatible surgical robot for precise radiological interventions". *Computer Aided Surgery*, Vol. 8, No. 4, pp. 180–191, 2003.

[Henn 11] J. Hennig and O. Speck, Eds. *High-field MR imaging*. Springer, 2011.

[Henn 99] J. Hennig. "K-space sampling strategies". *European Radiology*, Vol. 9, No. 6, pp. 1020–1031, 1999.

[Herr 09] S. Herrero and J. Bescós. "Background subtraction techniques: Systematic evaluation and comparative analysis". In: *Proceedings of the 11th International Conference on Advanced Concepts for Intelligent Vision Systems*, pp. 33–42, Bordeux, France, September 2009.

[Hind 66] J. Hindman. "Proton resonance shift of water in the gas and liquid states". *The Journal of Chemical Physics*, Vol. 44, No. 12, pp. 4582–4592, 1966.

[Hoff 12] R. Hoffmann, C. Thomas, H. Rempp, D. Schmidt, P. Pereira, C. Claussen, and S. Clasen. "Performing MR-guided biopsies in clinical routine: factors that influence accuracy and procedure time". *European Radiology*, Vol. 22, No. 3, pp. 663–671, 2012.

[Houg 62] P. Hough. "Method and means for recognizing complex patterns". Patent number US 3069654, 1962.

[Huet] S. Huettel. "Functional Magnetic Resonance Imaging". `http://www.biac.duke.edu/education/courses/fall04/fmri/`, accessed online July 2013.

[Insi 12] M. Insight, Ed. *United states markets for image-guided surgery products*. *Medical market and technology reports*, Elsevier Business Intelligence, 2012.

[Invi] Invivo. "Prostate Needle Guide". `http://www.invivocorp.com/Interventional/info.php?id=15`, accessed online January 2013.

[Ishi 95] Y. Ishihara, A. Calderon, H. Watanabe, K. Okamoto, Y. Suzuki, K. Kuroda, and Y. Suzuki. "A precise and fast temperature mapping using water proton chemical shift". *Magnetic Resonance in Medicine*, Vol. 34, No. 6, pp. 814–823, 1995.

[Jean 12] D. Jeanmonod, B. Werner, A. Morel, L. Michels, E. Zadicario, G. Schiff, and E. Martin. "Transcranial magnetic resonance imaging-guided focused ultrasound: noninvasive central lateral thalamotomy for chronic neuropathic pain". *Neurosurgical Focus*, Vol. 32, No. 1, p. E1, 2012.

[Jung 06] H. Jung, D. Kim, P. Yoon, and J. Kim. "Parking slot markings recognition for automatic parking assist system". In: *Intelligent Vehicles Symposium, 2006 IEEE*, pp. 106–113, IEEE, Tokyo, Japan, June 2006.

[Kahn 08] T. Kahn, F. Jolesz, and J. Lewin. "Special issue: Interventional MRI update". *Journal of Magnetic Resonance Imaging*, Vol. 27, No. 2, p. 252, 2008.

[Keat 01] N. Keat. "Real-time CT and CT fluoroscopy". *The British Journal of Radiology*, Vol. 74, No. 888, pp. 1088–1090, 2001.

[Khle 11] M. O. Köhler, B. Denis de Senneville, B. Quesson, C. T. Moonen, and M. Ries. "Spectrally selective pencil-beam navigator for motion compensation of MR-guided high-intensity focused ultrasound therapy of abdominal organs". *Magnetic Resonance in Medicine*, Vol. 66, No. 1, pp. 102–111, 2011.

[Khn 10] J. Kühn, S. Langner, K. Hegenscheid, M. Evert, A. Kickhefel, N. Hosten, and R. Puls. "Magnetic resonance-guided upper abdominal biopsies in a high-field wide-bore 3-T MRI system: feasibility, handling, and needle artefacts". *European Radiology*, Vol. 20, No. 10, pp. 2414–2421, 2010.

[Kick 10] A. Kickhefel, J. Roland, C. Weiss, and F. Schick. "Accuracy of real-time MR temperature mapping in the brain: a comparison of fast sequences". *Physica Medica*, Vol. 26, No. 4, pp. 192–201, 2010.

[Kick 12] A. Kickhefel, C. Weiss, J. Roland, P. Gross, F. Schick, and R. Salomir. "Correction of susceptibility-induced GRE phase shift for accurate PRFS thermometry proximal to cryoablation iceball". *Magnetic Resonance Materials in Physics, Biology and Medicine*, Vol. 25, No. 1, pp. 23–31, 2012.

[Kitt 86] J. Kittler and J. Illingworth. "Minimum error thresholding". *Pattern Recognition*, Vol. 19, No. 1, pp. 41–47, 1986.

[Kobu 12] T. Kobus, A. Bitz, M. van Uden, M. Lagemaat, E. Rothgang, S. Orzada, A. Heerschap, and T. Scheenen. "In Vivo 31P MR spectroscopic imaging of the human prostate at 7 T: Safety and feasibility". *Magnetic Resonance in Medicine*, Vol. 68, No. 6, pp. 1683–1695, 2012.

[Koch 06] K. Koch, X. Papademetris, D. Rothman, and R. de Graaf. "Rapid calculations of susceptibility-induced magnetostatic field perturbations for in vivo magnetic resonance". *Physics in medicine and biology*, Vol. 51, No. 24, pp. 6381–6402, 2006.

[Koli 04] S. Kolind, A. MacKay, P. Munk, and Q. Xiang. "Quantitative evaluation of metal artifact reduction techniques". *Journal of Magnetic Resonance Imaging*, Vol. 20, No. 3, pp. 487–495, 2004.

[Krie 05] A. Krieger, R. C. Susil, C. Ménard, J. A. Coleman, G. Fichtinger, E. Atalar, and L. L. Whitcomb. "Design of a novel MRI compatible manipulator for image guided prostate interventions". *IEEE Transactions on Biomedical Engineering*, Vol. 52, No. 2, pp. 306–313, 2005.

[Krus 52] W. Kruskal and W. Wallis. "Use of ranks in one-criterion variance analysis". *Journal of the American Statistical Association*, Vol. 47, No. 260, pp. 583–621, 1952.

[Kuro 06] K. Kuroda, D. Kokuryo, E. Kumamoto, K. Suzuki, Y. Matsuoka, and B. Keserci. "Optimization of self-reference thermometry using complex field estimation". *Magnetic Resonance in Medicine*, Vol. 56, No. 4, pp. 835–843, 2006.

[Kuru 07] Y. Kurumi, T. Tani, S. Naka, H. Shiomi, T. Shimizu, H. Abe, Y. Endo, and S. Morikawa. "MR-guided microwave ablation for malignancies". *International Journal of Clinical Oncology*, Vol. 12, No. 2, pp. 85–93, 2007.

[Ladd 96] M. Ladd, P. Erhart, J. Debatin, B. Romanowski, P. Boesiger, and G. McKinnon. "Biopsy needle susceptibility artifacts". *Magnetic Resonance in Medicine*, Vol. 36, No. 4, pp. 646–651, 1996.

[Lang 11] J. Langley, W. Potter, C. Phipps, F. Huang, and Q. Zhao. "A self-reference PRF-shift MR thermometry method utilizing the phase gradient". *Physics in Medicine and Biology*, Vol. 56, No. 24, pp. N307–N320, 2011.

[Laut 73] P. Lauterbur. "Image formation by induced local interactions: examples employing nuclear magnetic resonance". *Nature*, Vol. 242, No. 5394, pp. 190–191, 1973.

[Lava] P. Laval. "Mathematics for Computer Graphics - Barycentric Coordinates". `http://facultyfp.salisbury.edu/despickler/personal/Resources/Graphics/Resources/barycentric.pdf` , accessed online November 2012.

[Le B 89] D. Le Bihan, J. Delannoy, and R. Levin. "Temperature mapping with MR imaging of molecular diffusion: application to hyperthermia.". *Radiology*, Vol. 171, No. 3, pp. 853–857, 1989.

[Lee 14] T. Lee, N. Mendhiratta, D. Sperling, and H. Lepor. "Focal Laser Ablation for Localized Prostate Cancer: Principles, Clinical Trials, and Our Initial Experience". *Reviews in Urology*, Vol. 16, No. 2, pp. 55–66, 2014.

[Lewi 00] J. Lewin, S. Nour, and J. Duerk. "Magnetic resonance image-guided biopsy and aspiration". *Topics in Magnetic Resonance Imaging*, Vol. 11, No. 3, p. 173, 2000.

[Lewi 96] J. Lewin, J. Duerk, V. Jain, C. Petersilge, C. Chao, and J. Haaga. "Needle localization in MR-guided biopsy and aspiration: effects of field strength, sequence design, and magnetic field orientation". *American Journal of Roentgenology*, Vol. 166, No. 6, pp. 1337–1345, 1996.

[Lewi 99] J. Lewin. "Interventional MR imaging: concepts, systems, and applications in neuroradiology". *American Journal of Neuroradiology*, Vol. 20, No. 5, pp. 735–748, 1999.

[Ljun 83] S. Ljunggren. "A simple graphical representation of Fourier-based imaging methods". *Journal of Magnetic Resonance*, Vol. 54, No. 2, pp. 338–343, 1983.

[Lore 05] C. Lorenz, K. Kirchberg, S. Zuehlsdorff, P. Speier, M. Caylus, W. Borys, T. Moeller, and M. Guttman. "Interactive FrontEnd (IFE): A platform for graphical MR scanner control and scan automation". In: *Proceedings, 13th Annual Meeting, International Society of Magnetic Resonance in Medicine*, p. 2170, Miami (FL), USA, May 2005.

[Lore 87] W. E. Lorensen and H. E. Cline. "Marching cubes: A high resolution 3D surface construction algorithm". *ACM Siggraph Computer Graphics*, Vol. 21, No. 4, pp. 163–169, 1987.

[Lu 97] D. Lu, H. Lee, K. Farahani, S. Sinha, and R. Lufkin. "Biopsy of hepatic dome lesions: semi-real-time coronal MR guidance technique.". *American Journal of Roentgenology*, Vol. 168, No. 3, pp. 737–739, 1997.

[Lufk 88] R. Lufkin, L. Teresi, L. Chiu, and W. Hanafee. "A technique for MR-guided needle placement". *American Journal of Roentgenology*, Vol. 151, No. 1, pp. 193–196, 1988.

[Lumi 83] R. Lumia, L. Shapiro, and O. Zuniga. "A new connected components algorithm for virtual memory computers". *Computer Vision, Graphics, and Image Processing*, Vol. 22, No. 2, pp. 287–300, 1983.

[Mack 05] M. Mack, T. Lehnert, K. Eichler, T. Vogl, *et al.* "MR-guided laser ablation". *Magnetic Resonance Imaging Clinics of North America*, Vol. 13, No. 3, pp. 583–594, 2005.

[Macu 08] K. Macura and D. Stoianovici. "Advancements in Magnetic Resonance–Guided Robotic Interventions in the Prostate". *Topics in Magnetic Resonance Imaging*, Vol. 19, No. 6, pp. 297–304, 2008.

[Maga 11] J. Magaraggia. *Segmentation of Needle Artifacts in Real Time 2D Images*. Master's thesis, University of Padova, Italy, 2011.

[Maie 09] F. Maier, A. J. Krafft, J. W. Jenne, W. Semmler, and M. Bock. "TAM - a thermal ablation monitoring tool: in vivo evaluation". In: *World Congress on Medical Physics and Biomedical Engineering*, pp. 247–250, Munich, Germany, September 2009.

[Maie 12] F. Maier, A. J. Krafft, J. P. Yung, R. J. Stafford, A. Elliott, R. Dillmann, W. Semmler, and M. Bock. "Velocity navigator for motion compensated thermometry". *Magnetic Resonance Materials in Physics, Biology and Medicine*, Vol. 25, No. 1, pp. 15–22, 2012.

[Mans 77] P. Mansfield. "Multi-planar image formation using NMR spin echoes". *Journal of Physics C: Solid State Physics*, Vol. 10, No. 3, p. L55, 1977.

[Marr 06] J. Marrero and S. Pelletier. "Hepatocellular carcinoma". *Clinics in Liver Disease*, Vol. 10, No. 2, pp. 339–351, 2006.

[McDa 05] N. McDannold. "Quantitative MRI-based temperature mapping based on the proton resonant frequency shift: review of validation studies". *International Journal of Hyperthermia*, Vol. 21, pp. 533–546, 2005.

[McDa 06] N. McDannold, C. M. Tempany, F. M. Fennessy, M. J. So, F. J. Rybicki, E. A. Stewart, F. A. Jolesz, and K. Hynynen. "Uterine Leiomyomas: MR Imaging-based Thermometry and Thermal Dosimetry during Focused Ultrasound Thermal Ablation1". *Radiology*, Vol. 240, No. 1, pp. 263–272, 2006.

[McDa 10] N. McDannold, G. Clement, P. Black, F. Jolesz, and K. Hynynen. "Transcranial MRI-guided focused ultrasound surgery of brain tumors: Initial findings in three patients". *Neurosurgery*, Vol. 66, No. 2, pp. 323–332, 2010.

[Mill 03a] D. Miller, S. Balter, P. Cole, H. Lu, A. Berenstein, R. Albert, B. Schueler, J. Georgia, P. Noonan, *et al.* "Radiation doses in interventional radiology procedures: The RAD-IR study Part II: Skin dose". *Journal of Vascular and Interventional Radiology*, Vol. 14, No. 8, pp. 977–990, 2003.

[Mill 03b] D. Miller, S. Balter, P. Cole, H. Lu, B. Schueler, M. Geisinger, A. Berenstein, R. Albert, J. Georgia, P. Noonan, *et al.* "Radiation doses in interventional radiology procedures: The RAD-IR study Part I: Overall measures of dose". *Journal of Vascular and Interventional Radiology*, Vol. 14, No. 6, pp. 711–727, 2003.

[Miro 99] S. A. Mirowitz. "MR imaging artifacts. Challenges and solutions.". *Magnetic resonance imaging clinics of North America*, Vol. 7, No. 4, pp. 717–732, 1999.

[Moch 08] M. Moche, R. Trampel, T. Kahn, and H. Busse. "Navigation concepts for MR image-guided interventions". *Journal of Magnetic Resonance Imaging*, Vol. 27, No. 2, pp. 276–291, 2008.

[Moch 10] M. Moche, D. Zajonz, T. Kahn, and H. Busse. "MRI-guided procedures in various regions of the body using a robotic assistance system in a closed-bore scanner: preliminary clinical experience and limitations". *Journal of Magnetic Resonance Imaging*, Vol. 31, No. 4, pp. 964–974, 2010.

[Moel 02] A. Moelker, R. Maas, F. Lethimonnier, and P. Pattynama. "Interventional MR Imaging at 1.5 T: Quantification of Sound Exposure". *Radiology*, Vol. 224, No. 3, pp. 889–895, 2002.

[Mori 04] S. Morikawa, T. Inubushi, Y. Kurumi, S. Naka, K. Sato, K. Demura, T. Tani, and H. A. Haque. "Feasibility of respiratory triggering for MR-guided microwave ablation of liver tumors under general anesthesia". *Cardiovascular and Interventional Radiology*, Vol. 27, No. 4, pp. 370–373, 2004.

[Morr 08] P. Morrison, S. Silverman, K. Tuncali, and S. Tatli. "MRI-guided cryotherapy". *Journal of Magnetic Resonance Imaging*, Vol. 27, No. 2, pp. 410–420, 2008.

[Mose 12] E. Moser, F. Stahlberg, M. Ladd, and S. Trattnig. "7-T MRÛfrom research to clinical applications?". *NMR in Biomedicine*, Vol. 25, No. 5, pp. 695–716, 2012.

[Moze 09] P. Mozer, A. Partin, and D. Stoianovici. "Robotic image-guided needle interventions of the prostate". *Reviews in Urology*, Vol. 11, No. 1, pp. 7–15, 2009.

[Muel 86] P. Mueller, D. Stark, J. Simeone, S. Saini, R. Butch, R. Edelman, J. Wittenberg, and J. Ferrucci. "MR-guided aspiration biopsy: needle design and clinical trials". *Radiology*, Vol. 161, No. 3, pp. 605–609, 1986.

[Murr] G. Murray. "Rotation About an Arbitrary Axis in 3 Dimension". `http://inside.mines.edu/~gmurray/`, accessed online October 2012.

[Nara 88] P. Narayana, W. Brey, M. Kulkarni, and C. Sievenpiper. "Compensation for surface coil sensitivity variation in magnetic resonance imaging". *Magnetic Resonance Imaging*, Vol. 6, No. 3, pp. 271–274, 1988.

[Nawf 00] R. Nawfel, P. Judy, S. Silverman, S. Hooton, K. Tuncali, and D. Adams. "Patient and Personnel Exposure during CT Fluoroscopy-guided Interventional Procedures1". *Radiology*, Vol. 216, No. 1, pp. 180–184, 2000.

[Nels 95] K. L. Nelson and V. M. Runge. "Basic principles of MR contrast". *Topics in Magnetic Resonance Imaging*, Vol. 7, No. 3, pp. 124–136, 1995.

[Nitz 99] W. Nitz and P. Reimer. "Contrast mechanisms in MR imaging". *European Radiology*, Vol. 9, No. 6, pp. 1032–1046, 1999.

[Nour 10] S. Nour, S. Goldberg, F. Wacker, S. Rafie, S. Paul, J. Heidenreich, M. Rodgers, F. Abdul-Karim, J. Duerk, and J. Lewin. "MR Monitoring of NaCl-enhanced Radiofrequency Ablations: observations on Low-and High-Field-Strength MR Images with Pathologic Correlation". *Radiology*, Vol. 254, No. 2, pp. 449–459, 2010.

[Numm 03] K. Numminen, J. Halavaara, H. Isoniemi, P. Tervahartiala, L. Kivisaari, J. Numminen, and K. Höckerstedt. "Magnetic resonance imaging of the liver: true fast imaging with steady state free precession sequence facilitates rapid and reliable distinction between hepatic hemangiomas and liver malignancies". *Journal of Computer Assisted Tomography*, Vol. 27, No. 4, pp. 571–576, 2003.

[Ojal 02] R. Ojala, R. Sequeiros, R. Klemola, E. Vahala, L. Jyrkinen, and O. Tervonen. "MR-guided bone biopsy: preliminary report of a new guiding method". *Journal of Magnetic Resonance Imaging*, Vol. 15, No. 1, pp. 82–86, 2002.

[Oppe 86] A. Oppelt. "FISP: a new fast MRI sequence". *Electromedica*, Vol. 54, pp. 15–18, 1986.

[Otsu 79] N. Otsu. “A threshold selection method from gray-level histograms”. *IEEE Transactions on Systems, Man, and Cybernetics*, Vol. SMC-9, pp. 62–66, 1979.

[Pala 09] G. Paladini and F. Azar. “An extensible imaging platform for optical imaging applications”. In: *Proceedings, SPIE Medical Imaging*, p. 717108, San Jose (CA), USA, January 2009.

[Park 84] D. Parker. “Applications of NMR imaging in hyperthermia: an evaluation of the potential of localized tissue heating and noninvasive temperature monitoring”. *IEEE Transactions on Biomedical Engineering*, Vol. 31, No. 1, pp. 161–167, 1984.

[Perm 07] S. Permpongkosol, T. Nicol, H. Khurana, R. Link, Q. Zhai, L. Kavoussi, and S. Solomon. “Thermal maps around two adjacent cryoprobes creating overlapping ablations in porcine liver, lung, and kidney”. *Journal of Vascular and Interventional Radiology*, Vol. 18, No. 2, pp. 283–287, 2007.

[Prue 99] K. Pruessmann, M. Weiger, M. Scheidegger, and P. Boesinger. “SENSE: Sensitivity encoding for fast MRI”. *Magnetic Resonance in Medicine*, Vol. 42, No. 5, pp. 952–962, 1999.

[Rick 10] J. Ricke, M. Thormann, M. Ludewig, K. Jungnickel, O. Grosser, C. Wybranski, N. Peters, P. Hass, J. Bunke, and F. Fischbach. “MR-guided liver tumor ablation employing open high-field 1.0 T MRI for image-guided brachytherapy”. *European Radiology*, Vol. 20, No. 8, pp. 1985–1993, 2010.

[Riek 04] V. Rieke, K. K. Vigen, G. Sommer, B. L. Daniel, J. M. Pauly, and K. Butts. “Referenceless PRF shift thermometry”. *Magnetic Resonance in Medicine*, Vol. 51, No. 6, pp. 1223–1231, 2004.

[Riek 08] V. Rieke and K. Butts Pauly. “MR Thermometry”. *Journal of Magnetic Resonance Imaging*, Vol. 27, No. 2, pp. 376–390, 2008.

[Roth 08] E. Rothgang. *Enhanced Visualization of Real-Time MR Thermography*. Master’s thesis, University of Ulm, Germany, 2008.

[Roth 10a] E. Rothgang, W. Gilson, J. Hornegger, and C. Lorenz. “A system for advanced real-time visualization and monitoring of MR-guided thermal ablations”. In: *Proceedings, SPIE Medical Imaging*, p. 762522, San Diego (CA), USA, May 2010.

[Roth 10b] E. Rothgang, W. Gilson, S. Valdeig, L. Pan, A. Flammang, J. Roland, F. Wacker, and B. Frericks. “MRI guided cryoablation: In vivo assessment of measuring temperature adjacent to ablated tissue using the PRF method”. In: *Proceedings, 8th Interventional MRI Symposium*, pp. 39–42, Leipzig, Germany, Sep 2010.

[Roth 11a] E. Rothgang, W. Gilson, W. Strehl, L. Pan, J. Roland, C. Lorenz, and J. Hornegger. “Interventional MR-imaging for thermal ablation therapy”. In: *Proceedings, IEEE International Symposium on Biomedical Imaging*, pp. 1864–1868, Chicago (IL), USA, March 2011.

[Roth 11b] E. Rothgang, W. Gilson, S. Valdeig, L. Pan, J. Roland, A. Flammang, C. Lorenz, F. Wacker, and B. Frericks. “Enhanced Intra-Operative Control During Cryoablation by Using the PRF Method:

In Vivo Imaging and Histopathologic Correlation". In: *Proceedings, 19th Annual Meeting, International Society of Magnetic Resonance in Medicine*, p. 1762, Montréal (QC), Canada, May 2011.

[Roth 11c] E. Rothgang, J. Roland, W. Gilson, J. Hornegger, and C. Lorenz. "Automatic B0 Drift Correction for MR Thermometry". In: *Proceedings, 19th Annual Meeting, International Society of Magnetic Resonance in Medicine*, p. 1773, Montréal, Québec, Canada, May 2011.

[Roth 12a] E. Rothgang, E. Breton, X. Buy, A. Gangi, J. Garnon, R. Hoffmann, M. de Mathelin, L. Pan, H. Rempp, G. Tsoumakidou, C. R. Weiss, C. Lorenz, and W. Gilson. "Initial, multi-site clinical experience using an integrated interventional needle guidance workflow". In: *Proceedings, 9th Interventional MRI Symposium*, p. 141, Boston (MA), USA, Sep 2012.

[Roth 12b] E. Rothgang and W. Gilson. "Rapid Entry Point Localization for Percutaneous Interventions". In: *Proceedings, 20th Annual Meeting, International Society of Magnetic Resonance in Medicine*, p. 1591, Melbourne, Australia, May 2012.

[Roth 12c] E. Rothgang, W. Gilson, L. Pan, J. Roland, K. Kirchberg, F. Wacker, J. Hornegger, and C. Lorenz. "An Integrated System for MR-Guided Thermal Ablations: From Planning to Real-Time Temperature Monitoring". In: *Proceedings, 20th Annual Meeting, International Society of Magnetic Resonance in Medicine*, p. 1561, Melbourne, Australia, May 2012.

[Roth 13] E. Rothgang, W. Gilson, F. Wacker, A. Hornegger, C. Lorenz, and C. Weiss. "Rapid freehand MR-guided percutaneous needle interventions: An image based approach to improve workflow and feasibility". *Journal of Magnetic Resonance Imaging*, Vol. 37, No. 5, pp. 1202–1212, 2013.

[Saik 11] C. Saikus, K. Ratnayaka, I. Barbash, J. Colyer, O. Kocaturk, A. Faranesh, and R. Lederman. "MRI-guided vascular access with an active visualization needle". *Journal of Magnetic Resonance Imaging*, Vol. 34, No. 5, pp. 1159–1166, 2011.

[Saka 03] M. Sakarya, O. Unal, B. Ozbay, K. Uzun, I. Kati, S. Ozen, and O. Etlik. "MR fluoroscopy-guided transthoracic fine-needle aspiration biopsy: feasibility". *Radiology*, Vol. 228, No. 2, pp. 589–592, 2003.

[Salo 12] R. Salomir, M. Viallon, A. Kickhefel, J. Roland, D. R. Morel, L. Petrusca, V. Auboiroux, T. Goget, S. Terraz, C. D. Becker, *et al.* "Reference-Free PRFS MR-Thermometry Using Near-Harmonic 2-D Reconstruction of the Background Phase". *Medical Imaging, IEEE Transactions on*, Vol. 31, No. 2, pp. 287–301, 2012.

[Sche 03] K. Scheffler and S. Lehnhardt. "Principles and applications of balanced SSFP techniques". *European Radiology*, Vol. 13, No. 11, pp. 2409–2418, 2003.

[Sche 11] T. Scheenen, J. Fütterer, E. Weiland, P. van Hecke, M. Lemort, C. Zechmann, H. Schlemmer, D. Broome, G. Villeirs, J. Lu, J. Barentsz, S. Roell, and A. Heerschap. "Discriminating cancer from non-cancer tissue in the prostate by 3-dimensional proton magnetic re-

sonance spectroscopic imaging: a prospective multicenter validation study". *Investigative Radiology*, Vol. 46, No. 1, pp. 25–33, 2011.

[Schm 99] A. Schmidt, S. Kee, D. Sze, B. Daniel, M. Razavi, C. Semba, and M. Dake. "Diagnostic yield of MR-guided liver biopsies compared with CT-and US-guided liver biopsies". *Journal of Vascular and Interventional Radiology*, Vol. 10, No. 10, pp. 1323–1329, 1999.

[Scho 12] M. Schouten, J. Bomers, D. Yakar, H. Huisman, E. Rothgang, D. Bosboom, T. Scheenen, S. Misra, and J. Fütterer. "Evaluation of a robotic technique for transrectal MRI-guided prostate biopsies". *European Radiology*, Vol. 22, No. 2, pp. 476–483, 2012.

[Scia 11] A. Sciarra, J. Barentsz, A. Bjartell, J. Eastham, H. Hricak, V. Panebianco, and J. Witjes. "Advances in magnetic resonance imaging: how they are changing the management of prostate cancer". *European Urology*, Vol. 59, No. 6, pp. 962–977, 2011.

[Senn] B. Denis de Senneville. "Correction des mouvements pour la thermométrie réel guidée par IRM". `http://greg.maclair.free.fr/Soutenance_These.ppt`, accessed online May 2013.

[Senn 07] B. de Senneville, C. Mougenot, B. Quesson, I. Dragonu, N. Grenier, and C. Moonen. "MR thermometry for monitoring tumor ablation". *European Radiology*, Vol. 17, No. 9, pp. 2401–2410, 2007.

[Sequ 02] R. Sequeiros, R. Ojala, R. Klemola, T. Vaara, L. Jyrkinen, and O. Tervonen. "MRI-guided periradicular nerve root infiltration therapy in low-field (0.23-T) MRI system using optical instrument tracking.". *European Radiology*, Vol. 12, No. 6, pp. 1331–1337, 2002.

[Sero 08] O. Seror, M. Lepetit-Coiffé, B. Le Bail, B. Denis de Senneville, H. Trillaud, C. Moonen, and B. Quesson. "Real time monitoring of radiofrequency ablation based on MR thermometry and thermal dose in the pig liver in vivo". *European Radiology*, Vol. 18, No. 2, pp. 408–416, Feb. 2008.

[Sezg 04] M. Sezgin and B. Sankur. "Survey over image thresholding techniques and quantitative performance evaluation". *Journal of Electronic Imaging*, Vol. 13, No. 1, pp. 146–168, 2004.

[Silv 95] S. Silverman, B. Collick, M. Figueira, R. Khorasani, D. Adams, R. Newman, G. Topulos, and F. Jolesz. "Interactive MR-guided biopsy in an open-configuration MR imaging system". *Radiology*, Vol. 197, No. 1, pp. 175–181, 1995.

[Silv 99] S. Silverman, K. Tuncali, D. Adams, R. Nawfel, K. Zou, and P. Judy. "CT Fluoroscopy-guided Abdominal Interventions: Techniques, Results, and Radiation Exposure1". *Radiology*, Vol. 212, No. 3, pp. 673–681, 1999.

[Skin 98] M. Skinner, M. Iizuka, M. Kolios, and M. Sherar. "A theoretical comparison of energy sources, microwave, ultrasound and laser, for interstitial thermal therapy". *Physics in Medicine and Biology*, Vol. 43, No. 12, pp. 3535–3547, 1998.

[Solo 10] S. Solomon and S. Silverman. "Imaging in interventional oncology". *Radiology*, Vol. 257, No. 3, pp. 624–640, 2010.

[Song 12] S.-E. Song, N. B. Cho, I. I. Iordachita, P. Guion, G. Fichtinger, A. Kaushal, K. Camphausen, and L. L. Whitcomb. "Biopsy needle artifact localization in MRI-guided robotic transrectal prostate intervention". *IEEE Transactions on Biomedical Engineering*, Vol. 59, No. 7, pp. 1902–1911, 2012.

[Staf 09] R. Stafford, B. Fetics, A. Roth, C. Lorenz, A. Krafft, M. Bock, and K. Ahrar. "Tracking system for real-time MR-guided percutaneous interventions at 1.5T". In: *Proceedings, 17th Annual Meeting, International Society of Magnetic Resonance in Medicine*, p. 4420, Honolulu (HI), USA, May 2009.

[Staf 10] R. J. Stafford, D. Fuentes, A. A. Elliott, J. S. Weinberg, and K. Ahrar. "Laser-induced thermal therapy for tumor ablation". *Critical Reviews in Biomedical Engineering*, Vol. 38, No. 1, 2010.

[Staf 12] R. Stafford and K. Ahrar. *Interventional Magnetic Resonance Imaging*, Chap. MRI-Guided Thermal Ablation Techniques, pp. 253–269. Springer, 2012.

[Stat 08a] J. Stattaus, S. Maderwald, H. Baba, G. Gerken, J. Barkhausen, M. Forsting, and M. Ladd. "MR-guided liver biopsy within a short, wide-bore 1.5 Tesla MR system". *European Radiology*, Vol. 18, No. 12, pp. 2865–2873, 2008.

[Stat 08b] J. Stattaus, S. Maderwald, M. Forsting, J. Barkhausen, and M. Ladd. "MR-guided core biopsy with MR fluoroscopy using a short, wide-bore 1.5-Tesla scanner: feasibility and initial results". *Journal of Magnetic Resonance Imaging*, Vol. 27, No. 5, pp. 1181–1187, 2008.

[Stre 09] W. Strehl. *Passive needle tracking under real-time MRI guidance*. Master's thesis, University of Erlangen, Germany, 2009.

[Stre 10] F. Streitparth, T. Walter, U. Wonneberger, S. Chopra, F. Wichlas, M. Wagner, K. Hermann, B. Hamm, and U. Teichgräber. "Image-guided spinal injection procedures in open high-field MRI with vertical field orientation: feasibility and technical features". *European Radiology*, Vol. 20, No. 2, pp. 395–403, 2010.

[Suth 08] G. Sutherland, I. Latour, and A. Greer. "Integrating an image-guided robot with intraoperative MRI". *Engineering in Medicine and Biology Magazine, IEEE*, Vol. 27, No. 3, pp. 59–65, 2008.

[Tatl 07] S. Tatli, P. Morrison, K. Tuncali, and S. Silverman. "Interventional MRI for oncologic applications". *Techniques in Vascular and Interventional Radiology*, Vol. 10, No. 2, pp. 159–170, 2007.

[Tatl 10] S. Tatli, M. Acar, K. Tuncali, P. Morrison, and S. Silverman. "Percutaneous cryoablation techniques and clinical applications.". *Diagnostic and Interventional Radiology*, Vol. 16, pp. 90–95, 2010.

[Teic 06] V. Teichgräber, C. Aubé, D. Schmidt, E. Jehle, C. König, C. Claussen, and P. Pereira. "Percutaneous MR-guided radiofrequency ablation of recurrent sacrococcygeal chordomas". *American Journal of Roentgenology*, Vol. 187, No. 2, pp. 571–574, 2006.

[Temp 03] C. Tempany, E. Stewart, N. McDannold, B. Quade, F. Jolesz, and K. Hynynen. "MR imaging-guided focused ultrasound surgery of uterine leiomyomas: a feasibility study". *Radiology*, Vol. 226, No. 3, pp. 897–905, 2003.

[Terr 10] S. Terraz, A. Cernicanu, M. Lepetit-Coiffé, M. Viallon, R. Salomir, G. Mentha, and C. Becker. "Radiofrequency ablation of small liver malignancies under magnetic resonance guidance: progress in targeting and preliminary observations with temperature monitoring". *European Radiology*, Vol. 20, No. 4, pp. 886–897, 2010.

[Than 08] L. Thanos, S. Mylona, P. Galani, M. Pomoni, A. Pomoni, I. Koskinas, *et al.* "Overcoming the heat-sink phenomenon: successful radiofrequency thermal ablation of liver tumors in contact with blood vessels". *Diagnostic and Interventional Radiology*, Vol. 14, No. 1, pp. 51–56, 2008.

[Tie 13] C. Tie, C. Zou, M. He, W. Guo, Y. Chung, and X. Liu. "Comprehensive Comparison of Six Referenceless PRF Shift MR Thermometry Methods". In: *Proceedings, 21th Annual Meeting, International Society of Magnetic Resonance in Medicine*, p. 229, Salt Lake City (UT), USA, April 2013.

[Tsek 07] N. Tsekos, A. Khanicheh, E. Christoforou, and C. Mavroidis. "Magnetic resonance-compatible robotic and mechatronics systems for image-guided interventions and rehabilitation: a review study". *Annual Review of Biomedical Engineering*, Vol. 9, pp. 351–387, 2007.

[Tsou 11] G. Tsoumakidou, X. Buy, J. Garnon, J. Enescu, and A. Gangi. "Percutaneous thermal ablation: how to protect the surrounding organs". *Techniques in Vascular and Interventional Radiology*, Vol. 14, No. 3, pp. 170–176, 2011.

[Twie 83] D. Twieg. "The k-trajectory formulation of the NMR imaging process with applications in analysis and synthesis of imaging methods". *Medical Physics*, Vol. 10, No. 5, pp. 610–621, 1983.

[U Th 13] P. U-Thainual, J. Fritz, C. Moonjaita, T. Ungi, A. Flammang, J. Carrino, G. Fichtinger, and I. Iordachita. "MR image overlay guidance: system evaluation for preclinical use". *International Journal of Computer Assisted Radiology and Surgery*, Vol. 8, No. 3, pp. 365–378, 2013.

[Vige 03] K. K. Vigen, B. L. Daniel, J. M. Pauly, and K. Butts. "Triggered, navigated, multi-baseline method for proton resonance frequency temperature mapping with respiratory motion". *Magnetic Resonance in Medicine*, Vol. 50, No. 5, pp. 1003–1010, 2003.

[Vika 10] S. Vikal, P. U-Thainua, J. Carrino, I. Iordachita, G. Fischer, and G. Fichtinger. "Perk Station–Percutaneous surgery training and performance measurement platform". *Computerized Medical Imaging and Graphics*, Vol. 34, No. 1, pp. 19–32, 2010.

[Vogl 02] T. J. Vogl, R. Straub, K. Eichler, D. Woitaschek, and M. G. Mack. "Malignant Liver Tumors Treated with MR Imaging-guided Laser-induced Thermotherapy: Experience with Complications in 899 Patients (2,520 lesions)". *Radiology*, Vol. 225, No. 2, pp. 367–377, 2002.

[Wack 06] F. Wacker, S. Vogt, A. Khamene, J. Jesberger, S. Nour, D. Elgort, F. Sauer, J. Duerk, and J. Lewin. "An augmented reality system for MR image-guided needle biopsy: initial results in a swine model". *Radiology*, Vol. 238, No. 2, pp. 497–504, 2006.

[Wack 98] F. Wacker, D. Cholewa, A. Roggan, A. Schilling, J. Waldschmidt, and K. Wolf. "Vascular lesions in children: percutaneous MR imaging-guided interstitial Nd: YAG laser therapy - preliminary experience.". *Radiology*, Vol. 208, No. 3, pp. 789–794, 1998.

[Wans 05] J. P. Wansapura, B. L. Daniel, K. K. Vigen, and K. Butts. "In Vivo MR Thermometry of Frozen Tissue Using R2* and Signal Intensity". *Academic Radiology*, Vol. 12, No. 9, pp. 1080–1084, 2005.

[Weid 04] C. Weidensteiner, N. Kerioui, B. Quesson, B. D. de Senneville, H. Trillaud, and C. T. Moonen. "Stability of real-time MR temperature mapping in healthy and diseased human liver". *Journal of Magnetic Resonance Imaging*, Vol. 19, No. 4, pp. 438–446, 2004.

[Weis 08] C. Weiss, S. Nour, and J. Lewin. "MR-guided biopsy: a review of current techniques and applications". *Journal of Magnetic Resonance Imaging*, Vol. 27, No. 2, pp. 311–325, 2008.

[Wood 10] D. Woodrum, K. Gorny, L. Mynderse, K. Amrami, J. Felmlee, H. Bjarnason, O. Garcia-Medina, R. McNichols, T. Atwell, and M. Callstrom. "Feasibility of 3.0 T magnetic resonance imaging-guided laser ablation of a cadaveric prostate". *Urology*, Vol. 75, No. 6, pp. 1514.e1–e6, 2010.

[Wren 97] C. Wren, A. Azarbayejani, T. Darrell, and A. Pentland. "Pfinder: Real-time tracking of the human body". *IEEE Transactions on Pattern Analysis and Machine Intelligence*, Vol. 19, No. 7, pp. 780–785, 1997.

[Xu 10] H. Xu, A. Lasso, S. Vikal, P. Guion, A. Krieger, A. Kaushal, L. Whitcomb, and G. Fichtinger. "Accuracy validation for MRI-guided robotic prostate biopsy". In: *Proceedings of SPIE*, p. 762517, NIH Public Access, 2010.

[Yaka 08] D. Yakar, T. Hambrock, C. Hoeks, J. Barentsz, and J. Fütterer. "Magnetic resonance-guided biopsy of the prostate: feasibility, technique, and clinical applications". *Topics in Magnetic Resonance Imaging*, Vol. 19, No. 6, pp. 291–295, 2008.

[Yaka 11] D. Yakar, M. Schouten, D. Bosboom, J. Barentsz, T. Scheenen, and J. Fütterer. "Feasibility of a Pneumatically Actuated MR-compatible Robot for Transrectal Prostate Biopsy Guidance". *Radiology*, Vol. 260, No. 1, pp. 241–247, 2011.

[Yang 94] L. Yang, F. Albregtsen, T. Lonnestad, and P. Grottum. "Methods to estimate areas and perimeters of blob-like objects: a comparison". In: *Proceedings of the IAPR Workshop on Machine Vision Applications*, pp. 272–276, Kawasaki, Japan, December 1994.

[Yuan 12] J. Yuan, C.-S. Mei, L. P. Panych, N. J. McDannold, and B. Madore. "Towards fast and accurate temperature mapping with proton resonance frequency-based MR thermometry". *Quantitative Imaging in Medicine and Surgery*, Vol. 2, No. 1, pp. 21–32, 2012.

[Yutz 08] S. Yutzy and J. Duerk. "Pulse sequences and system interfaces for interventional and real-time MRI". *Journal of Magnetic Resonance Imaging*, Vol. 27, No. 2, pp. 267–275, 2008.

[Zang 06] S. Zangos, K. Eichler, A. Wetter, T. Lehnert, R. Hammerstingl, T. Diebold, P. Reichel, C. Herzog, M. Hansmann, M. Mack, *et al.* "MR-guided biopsies of lesions in the retroperitoneal space: technique and results". *European Radiology*, Vol. 16, No. 2, pp. 307–312, 2006.

[Zang 11] S. Zangos, A. Melzer, K. Eichler, C. Sadighi, A. Thalhammer, B. Bodelle, R. Wolf, T. Gruber-Rouh, D. Proschek, R. Hammerstingl, *et al.* "MR-compatible assistance system for biopsy in a high-field-strength system: initial results in patients with suspicious prostate lesions". *Radiology*, Vol. 259, No. 3, pp. 903–910, 2011.

Vitae

Eva Rothgang was born in Erlangen, Germany. After graduating from Martin-Behaim-Gymnasium, Nuremberg, Germany, in 2002, Eva went on to earn her Diplom degree (equivalent to Master of Science) in Computer Science from the University of Ulm, Germany, in 2008. From October 2006 to June 2007 she was at the University of Essex, Great Britain, for postgraduate studies in Computer Science. She wrote her master's thesis at the Center for Applied Medical Imaging, Siemens Corporate Technology, based at Johns Hopkins University in Baltimore, Maryland, and continued to collaborate closely with the lab during her PhD work. Since December 2008, Eva has been a PhD candidate at the Pattern Recognition Lab of Prof. Hornegger, and since February 2012, Eva has been a full-time employee of Siemens. Her research interests include MR-guided percutaneous interventions with focus on image-based needle navigation and MR thermometry. Eva worked as a research scientist at Siemens Corporate Technology, Corporate Research, until August 2013 and she is now managing the program for percutaneous interventions and electrophysiology at Siemens Healthcare, Magnetic Resonance.

Publications

Refereed Journal Publications

1. E. Rothgang, W.D. Gilson, F. Wacker, J. Hornegger, C.H. Lorenz, C.R. Weiss. "Rapid freehand MR-guided percutaneous needle interventions: An image based approach to improve workflow and feasibility". *Journal for Magnetic Resonance Imaging*, 2013, 37(5), pp. 1202-1212.

2. R. Hoffmann, H. Rempp, C. Schraml, N. Schwenzer, G. Grözinger, G. Blumenstock, E. Rothgang, P.L. Pereira, C.D. Clausen, S. Clasen. "Diffusion-weighted imaging during MR-guided radiofrequency ablation of hepatic malignancies: analysis of immediate pre- and post-ablative diffusion characteristics.". *Acta Radiologica*, 2014. [Epub ahead of print]

3. H. Rempp, H. Loh, R. Hoffmann, E. Rothgang, L. Pan, C.D. Claussen, S. Clasen. "Liver lesion conspicuity during real-time MR-guided radiofrequency applicator placement using spoiled gradient echo and balanced steady-state free precession imaging". *Journal of Magnetic Resonance Imaging*, 2014, 40(2), pp. 432-439.

4. T. Kobus, A.K. Bitz, M.J. van Uden, M.W. Lagemaat, E. Rothgang, S. Orzada, A. Heerschap, T.W.J. Scheenen. "In vivo 31P MR spectroscopic imaging of the human prostate at 7T: Safety and feasibility". *Magnetic Resonance in Medicine*, 2012, 68(6), pp. 1683-1695.

5. M.G. Schouten, J.G.R. Bomers, D. Yakar, H. Huisman, E. Rothgang, D. Bosboom, T.W.J. Scheenen, S. Misra, J.J. Fütterer. "Evaluation of a robotic technique for transrectal MRI-guided prostate biopsies". *European Radiology*, 2012, 22(2), pp. 476-483.

6. J.G.R. Bomers, E. Rothgang, J. Roland, J.O. Barentsz, J.J. Fütterer. "MR-guided temperature mapping in prostate cancer patients: stability and feasibility". [In Submission]

Patents

7. J. Roland, E. Rothgang, M. Suehling. "Method and apparatus for generation of image data based on MR thermometry data." DE 102013203407.5, US 20140243654 A1 (patent published on August 28, 2014).

8. A. Bakai, E. Rothgang. "Method and projection device to mark a surface of a 3D exmination subject." DE 102013203399.0, US 20140241511 A1 (patent published on August 28, 2014).

9. A. Bakai, H. Eder, P. Gross, M. Ringholz, E. Rothgang. "Method to prepare an interventional and/ or diagnostic imaging procedure with at least two different medical imaging modalities." DE 102013201828.2, US 20140219525 A1 (patent published on August 7, 2014).

10. M. Ringholz, J. Roland, E. Rothgang. "Method for determining the effect of a medical device on the image data of a magnetic resonance examination and/ or exami-

nation subject examined by means of magnetic resonance." DE 102013200188.6, US 20140191754 A1 (patent published on July 10, 2014).

11. E. Rothgang. "Method and magnetic resonance system to automatically determine imaging planes." CN 103300921A, DE 102012204134.6, US 20130245427 A1 (patent published on September 19, 2013).

12. J. Roland, E. Rothgang. "Coil former used in MRI process for examining organ of patient, has welding tool to weld main portion with welding punch and counter stamp in sterile barrier that is sealed to sterile environment and is detachably followed by housing." DE 102012203972.4 (patent published on September 19, 2013).

13. W.D. Gilson, E. Rothgang. "Rapid entry point localization for percutaneous interventions." US 20130218003 A1 (patent published on August 22, 2013).

14. M. Requardt, E. Rothgang. "Method and magnetic resonance device to assist a person conducting a minimally invasive procedure." DE 102011085308.1 (patent published on May 2, 2013), US 20130116546 A1 (patent published on May 9, 2013).

15. A. Kickhefel, J. Roland, E. Rothgang. "Magnetic resonance method and system to determine the position of a slice relative to a region moving relative to the slice." CN 102565736, DE 102010042518.4 (patent granted on January 24, 2013), US 20120092011 A1 (patent published on April 19, 2012).

16. W.D. Gilson, E. Rothgang, W. Strehl. "System and method for passive medical device navigation under real-time MRI guidance." US 8526691 B2 (patent granted on September 3, 2013).

Refereed Conference Proceedings

17. E. Rothgang, W.D. Gilson, W. Strehl, L. Pan, J. Roland, C. Lorenz, J. Hornegger. "Interventional MR-Imaging for thermal ablation therapy". In: *Proceedings of 2011 IEEE International Symposium on Biomedical Imaging: From Nano to Macro (ISBI)*, pp. 1864-1868, Chicago (IL), USA, March 2011.

18. E. Rothgang, W.D. Gilson, J. Hornegger, C. Lorenz. "A system for advanced real-time visualization and monitoring of MR-guided thermal ablations". In: *Proceedings of Medical Imaging: Visualization, Image-Guided Procedures, and Modeling (SPIE Medical Imaging), Vol. 7625*, pp. 762522-1, San Diego (CA), USA, Feb 2010.

Conference Abstracts

19. H. Rempp, R. Hoffmann, E. Rothgang, P. Li, H. Loh, P. L. Pereira, K. Nikolaou, S. Clasen. "Liver lesion conspicuity in interactive MR fluoroscopic sequences: dependency on lesion histology, size and image weighting." *10th Interventional MRI Symposium - Book of Abstracts*, p. 77, Leipzig, Germany, Oct 2014.

20. J. Garnon, G. Tsoumakidou, E. Rothgang, M. de Mathelin, E. Breton, A. Gangi. "MRI-guided mediastinal biopsies: retrospective evaluation on 15 cases". *10th Interventional MRI Symposium - Book of Abstracts*, p. 119, Leipzig, Germany, Oct 2014.

21. M. Neumann, É. Breton, L. Cuvillon, L. Pan, E. Rothgang, A. Hengerer, M. de Mathelin. "Wireless hybrid passive and active tracking for automatic image plane alignment". *10th Interventional MRI Symposium - Book of Abstracts*, p. 145, Leipzig, Germany, Oct 2014.

22. K.M. Sekins, S. Brunke, X. Zeng, S. Barnes, J. Hoppel, D. Liu, S. Hsu, C. Lee, C. Maleke, J. Nam, J. Eaton, K. Wong, L. Petrusca, M. Viallon, S. Terraz, C. Becker, R. Salomir, C.H. Lorenz, K.J. Kirchberg, S.M. Shea, S. Patil, J. Barbot, T. Meng, E. Rothgang, J. Roland. "Compact modular MR-guided HIFU system for treatment of liver cancer". *Proceedings of Annual International Symposium for Therapeutic Ultrasound.*, Vol. 13, p. 1699836, Shanghai, China, May 2013.

23. J.G.R. Bomers, E. Rothgang, K. Overduin, J. Roland, J.O. Barentsz, J.J. Fütterer. "MR-guided temperature mapping in prostate cancer patients: stability and feasibility". *Proceedings of International Society for Magnetic Resonance in Medicine (ISMRM)*, Vol. 21, p. 1808, Salt Lake City (UT), USA, April 2013.

24. G. Tsoumakidou, H. Lang, J. Garnon, E. Breton, E. Rothgang, A. Gangi. "Transperineal prostate cryoablation under MR-guidance". *Proceedings of International Society for Magnetic Resonance in Medicine (ISMRM)*, Vol. 21, p. 3409, Salt Lake City (UT), USA, April 2013.

25. M. Hoes, J.G.R. Bomers, K. Overduin, E. Rothgang, J.J. Fütterer, F. De Lange. "Towards Proton Resonance Frequency Shift (PRFS) Thermometry during Focal MR-guided Cryotherapy". *Radiological Society of North America (RSNA) Scientific Assembly and Annual Meeting*, pp. LL-PHS-TU4C, Chicago (IL), USA, Nov 2012.

26. E. Rothgang, E. Breton, X. Buy, et al. “Initial, multi-site clinical experience using an integrated interventional needle guidance workflow”. *9th Interventional MRI Symposium - Book of Abstracts*, p. 141, Boston (MA), USA, Sep 2012.

27. J.G.R. Bomers, E. Rothgang, J. Roland, J.O. Barentsz, J.J. Fütterer. “MR-guided temperature mapping in prostate cancer patients: stability and feasibility”. *9th Interventional MRI Symposium - Book of Abstracts*, p. 17, Boston (MA), USA, Sep 2012.

28. E. Breton, E. Rothgang, L. Pan, et al. “Spinal infiltrations and biopsies using an advanced real-time MR guidance approach: preliminary clinical report”. *Proceedings of International Society for Magnetic Resonance in Medicine (ISMRM)*, Vol. 20, p. 212, Melbourne, Australia, May 2012.

29. E. Rothgang, W.D. Gilson, L. Pan, et al. “An Integrated System for MR-Guided Thermal Ablations: From Planning to Real-Time Temperature Monitoring”. *Proceedings of International Society for Magnetic Resonance in Medicine (ISMRM)*, Vol. 20, p. 1561, Melbourne, Australia, May 2012.

30. E. Rothgang, W.D. Gilson. “Rapid Entry Point Localization for Percutaneous Interventions”. *Proceedings of International Society for Magnetic Resonance in Medicine (ISMRM)*, Vol. 20, p. 1591, Melbourne, Australia, May 2012.

31. E. Rothgang, C.R. Weiss, F. Wacker, J. Hornegger, C.H. Lorenz, W.D. Gilson. “Improved Workflow for Freehand MR-Guided Percutaneous Needle Interventions: Methods and Validation”. *Proceedings of International Society for Magnetic Resonance in Medicine (ISMRM), Vol. 20*, p. 1605, Melbourne, Australia, May 2012.

32. E. Rothgang, J. Roland, W.D. Gilson, J. Hornegger, C.H. Lorenz. “Automatic B0 Drift Correction for MR Thermometry”. *Proceedings of International Society for Magnetic Resonance in Medicine (ISMRM)*, Vol. 19, p. 1773, Montréal, Québec, Canada, May 2011.

33. E. Rothgang, W.D. Gilson, S. Valdeig, et al. “Enhanced Intra-Operative Control During Cryoablation by Using the PRF Method: In Vivo Imaging and Histopathologic Correlation”. *Proceedings of International Society for Magnetic Resonance in Medicine (ISMRM)*, Vol. 19, p. 1762, Montréal, Québec, Canada, May 2011.

34. B. Frericks, E. Rothgang, W.D. Gilson, et al. “In Vivo Online MR Thermometry for Detection of Heat Sink Effects during Thermal Ablation of Porcine Liver:

PRF-based Temperature Measurements with Pathologic Correlation". *Radiological Society of North America (RSNA) Scientific Assembly and Annual Meeting*, p. VO41-05, Chicago (IL), USA, Nov 2010.

35. E. Rothgang, W.D. Gilson, S. Valdeig, et al. "MRI guided cryoablation: In vivo assessment of measuring temperature adjacent to ablated tissue using the PRF method". *8th Interventional MRI Symposium - Book of Abstracts*, pp. 39-42, Leipzig, Germany, Sep 2010.

36. W. Strehl, E. Rothgang, W.D. Gilson, J. Hornegger, C.H. Lorenz. "A Passive, Image-Based Navigation Tool for Real-Time MR-Guided Percutaneous Interventional Procedures". *Proceedings of International Society for Magnetic Resonance in Medicine (ISMRM)*, Vol. 18, p. 1840, Stockholm, Sweden, May 2010.

37. E. Rothgang, W.D. Gilson, J. Roland, J. Hornegger, C.H. Lorenz. "TMAP @ IFE - A Framework for Guiding and Monitoring Thermal Ablations". *Proceedings of International Society for Magnetic Resonance in Medicine (ISMRM)*, Vol. 18, p. 4144, Stockholm, Sweden, May 2010.

38. E. Rothgang, A. Kickhefel, J. Roland, C. Rosenberg, J. Hornegger, C.H. Lorenz. "Online improvement of the reliability of PRF based temperature maps displayed during laser-induced thermotherapy of liver lesions". *Magnetic Resonance Materials in Physics, Biology and Medicine*, 2009, 22(1), p. 390.

39. A. Kickhefel, E. Rothgang, C. Rosenberg, J. Roland, F. Schick. "Improving In-Vivo MR Thermotherapy Reliability in Moving Organ by applying Pennes' Bioheat Equation - Evaluation on Patient Liver Study". *Magnetic Resonance Materials in Physics, Biology and Medicine*, 2009, 22(1), p. 380.